

**Rational Design and Activation of Microporous Coordination Polymers
Towards Targeted Structures and Porosity**

by

Jialiu Ma

A dissertation submitted in partial fulfillment
of the requirements for the degree of
Doctor of Philosophy
(Chemistry)
in The University of Michigan
2018

Doctoral Committee:

Professor Adam J. Matzger, Chair
Associate Professor Bart M. Bartlett
Professor Robert T. Kennedy
Associate Professor Donald J. Siegel

Jialiu Ma

jialiuma@umich.edu

ORCID iD: [0000-0002-5481-9383](https://orcid.org/0000-0002-5481-9383)

© Jialiu Ma 2018

For my parents

Guolin Ma and Zumei Li

Acknowledgements

I would like to first thank my advisor, Prof. Adam Matzger, for his guidance and support throughout my graduate school. No words can express my gratitude towards all the things he has taught me. I would also like to thank Prof. Robert Kennedy, Prof. Bart Bartlett and Prof. Don Siegel for serving on my dissertation committee. I am also grateful to all the help from Dr. Antek Wong-Foy on instrumentation and crystallography. I'd like to thank all my collaborators Dr. Ananya Dutta, Dr. Ly Tran, Dr. Saona Seth, Joshua Damron (Prof. Ayyalusamy Ramamoorthy's group) and Jaehun Jun (Prof. Jinsang Kim's group) for their time and commitments to the projects.

To all the past and current members of the Matzger lab, Ly, Ananya, Ping, Zi, Laura, Jon, Jake, Kyle, Kortney, Yiyang, Rosalyn, Chengcheng, Derek, Saona, Darpan, Matias, Raj, Ren, Ryan, Greg and Andy (my favorite undergraduate), thank you for the countless talks and delicious food. Special thanks go to Jake for being my loyal lunch buddy during the last four years in Michigan.

To Junsi and Eli from the Maldonado lab, thank you for mentoring me during my rotation semester. The way they think and do research influences me throughout my time in graduate school.

To my friends outside of lab in Ann Arbor, Junjie, Minyu and Junqi, I'd like to thank them for all the fun time spent together.

To my amazing girlfriend, Qingyi Wang, thank you for making my life so sweet and colorful.

To my parents, Guolin Ma and Zumei Liu, I am eternally grateful for the support and encouragement. You taught me love and everything.

Table of Contents

Dedication.....	ii
Acknowledgements.....	iii
List of Figures.....	vii
List of Tables.....	xii
Abstract.....	xiii
Chapter 1: Introduction.....	1
1.1 Microporous Coordination Polymer.....	1
1.2 Key Elements in MCP Design.....	2
1.2.1 Linkers.....	2
1.2.2 Metal Clusters.....	4
1.2.3 Framework Topology.....	4
1.3 Microporous Coordination Polymer Activation.....	5
1.4 Organization of Thesis.....	6
1.5 Figures.....	7
1.6 References.....	8
Chapter 2: The Role of Modulator in Controlling Layer Spacings in a Tritopic Linker Based Zirconium 2D-Microporous Coordination Polymer.....	10
2.1 Introduction.....	10
2.2 Results and Discussion.....	11
2.3 Conclusions.....	16
2.4 Experimental Methods.....	16
2.5 Figures.....	19

2.6 References.....	26
Chapter 3: Towards Topology Prediction in Zr-Based Microporous Coordination Polymers: the Role of Linker Geometry and Flexibility.....	28
3.1 Introduction.....	28
3.2 Results and Discussion	30
3.3 Conclusions.....	35
3.4 Experimental Methods	35
3.5 Figures.....	37
3.6 Tables	42
3.7 References.....	49
Chapter 4: Rapid Guest Exchange and Ultra-low Surface Tension Solvents Optimize Metal-Organic Framework Activation [†]	51
4.1 Introduction.....	51
4.2 Results and Discussion	52
4.3 Conclusions.....	56
4.4 Experimental Methods	56
4.5 Figures.....	59
4.6 Tables	64
4.7 References.....	64
Appendix A: A Perylene-based Microporous Coordination Polymer Interacts Selectively with Electron Poor Aromatics [†]	66
A.1 Introduction.....	66
A.2 Results and Discussion.....	67
A.3 Conclusions.....	71
A.4 Experimental Methods	71
A.5 Figures.....	75
A.6 Tables	78

A.7 References 78

List of Figures

Figure 1.1 Structures of MCPs: a) MOF-5, and b) HKUST-1.....	7
Figure 1.2 examples of linker used in the construction of MCPs a) with increased connectivity, b) same connectivity but with different geometry.....	7
Figure 1.3 a) $Zn_4O(CO_2R)_6$, b) $Cu_2(CO_2R)_4$ and c) $Zr_6O_4(OH_4)(CO_2R)_{12}$ metal cluster ...	8
Figure 1.4 Structure of a) MOF-5 and its corresponding topology b) pcu net.....	8
Figure 2.1. Summary of common Zr_6 clusters with different coordination numbers: a) 12 coordinate, b) 8 coordinate, c) 6 coordinate (trigonal prismatic), d) 6 coordinate (hexagonal planar).	19
Figure 2.2. a) Octahedral core of the Zr_6 cluster. Four of the μ_3 -O on the face of the octahedral are hydroxyl b) A Zr_6 cluster with 6 coordinate (hexagonal planar) arrangement of ligands. c) A Zr_6 cluster with 6 coordinate (hexagonal planar) arrangement of ligands highlighting terminal oxygen demonstrating coordination environment for Zr centers in UMCM-309a.....	19
Figure 2.3. Model structure of UMCM-309a and expansion of a single Zr_6 cluster.	20
Figure 2.4. Results of Pawley refinement for UMCM-309a.	20
Figure 2.5. TGA trace of UMCM-309a. Conditions: temperature ramp from 25 °C to 600 °C at 10 °C/min under flow of N_2 gas.	21
Figure 2.6. N_2 isotherm at 77 K for UMCM-309a.....	21
Figure 2.7. PXRD pattern of UMCM-309a and UMCM-309a treated with water and 1 M HCl for 4 months at room temperature.	22
Figure 2.8. PXRD pattern of UMCM-309c as-synthesized and the pattern for UMCM-309c after 10 min, 30 min and 45 min in air. After 45 min in air, another PXRD pattern was	

obtained after adding DMF to the dried UMCM-309c.....	22
Figure 2.9. ^1H spectrum of digested UMCM-309b before and after treatment with water/DMF at 120 °C for 3 days. Samples were digested with 10 wt% $\text{D}_2\text{SO}_4/\text{DMSO-d}_6$. From integration, the ratio between H_3BTB and benzoic acid was determined to be 2:4.84.....	23
Figure 2.10. ^1H spectrum of digested UMCM-309c before and after treatment with water/DMF at 120 °C for 3 days. Samples were digested with 10 wt% $\text{D}_2\text{SO}_4/\text{DMSO-d}_6$. From integration, the ratio between H_3BTB and biphenyl-4-carboxylic acid was determined to be 2:5.32.	23
Figure 2.11. a) Biphenyl-4-carboxylate coordinated to the free sites of the Zr_6 cluster. b) Experimental and calculated peak positions of UMCM-309c based on a c -axis of 14.8 Å. c) Results of Pawley refinement for UMCM-309c.....	24
Figure 2.12. PXRD pattern of UMCM-309a and the pattern for UMCM-309c treated with water/DMF mixture at 120 °C for three days.	25
Figure 2.13. N_2 isotherm at 77 K for UMCM-309c treated with water/DMF mixture at 120 °C for three days.	25
Figure 3.1. Topology representations of a) H_2BDC , H_3BTB and b) H_3TPTC	37
Figure 3.2. Classification of tetratopic linkers based on symmetry.....	38
Figure 3.3 Two ways of measuring aspect ratio (distance between centroids in Zr_6 cluster versus distance between carbon atoms in carboxylate group in the unit of Å) exemplified in a) NU-1000 and b) PCN-222. NU-1000 shows an aspect ratio of 1.003 (by distance between carbon atoms in the carboxylate) or 1.19 (by distance between centroids in the cluster). PCN-222 shows an aspect ratio of 1.06 (by distance between carbon atoms in the carboxylate) or 1.22 (by distance between centroids in the cluster). In either case, both measurements indicate a rectangular geometry of the ligand. In practice, especially when designing new MCPs, aspect ratios measured by carbon atoms are good enough indicator for ligand geometry.....	38

Figure 3.4 Mechanisms by which a flexible linker can access multiple geometries. a) A planar linker deforms to adopt both square and rectangular shapes. b) Adoption of both tetrahedral and planar shapes through bond rotation.	39
Figure 3.5. Common Zr_6 clusters and their topology representations of a) 12-connected $[Zr_6(\mu_3-O)_4(\mu_3-OH)_4(COOR)_{12}]$ and b) 8-connected $[Zr_6(\mu_3-O)_4(\mu_3-OH)_4(OH)_4(H_2O)_4(COOR)_8]$	39
Figure 3.6. Topology prediction framework for designing tetratopic based Zr MCP.	40
Figure 3.7. Structure of UMCM-312 a) Linker structure and its topology representation. b) Crystal structure of UMCM-312. c) Topology representation of <i>flu</i> topology.	40
Figure 3.8. Structure of UMCM-313 a) Linker structure and its topology representation. b) Crystal structure of UMCM-313. c) Topology representation of <i>csq</i> topology.	41
Figure 3.9. Relative energy of perylene-based and porphyrin-based linkers at different aspect ratios (aspect ratios observed in MCP crystal structures are marked with arrows).	41
Figure 4.1. a) Guest exchange in MOFs from high boiling point to low boiling point solvent. b) Guest evacuation to remove solvent from MOFs by vacuum.	59
Figure 4.2. a) Images of UMCM-9 in DMF exchanged into CH_2Cl_2 . Crystals were found to float (0s) and then sink back to the bottom (10s) completely (30s). b) 1H -NMR spectroscopy monitoring of the amount of DMF diffusing into CH_2Cl_2 during the c) first and d) second solvent exchange process of MOF-5.	60
Figure 4.3. N_2 isotherm plot of MOF-5 after 1 (BET SA = $2650 \pm 20 \text{ m}^2/\text{g}$), 2 (BET SA = $3410 \pm 30 \text{ m}^2/\text{g}$) or 3 (BET SA = $3640 \pm 40 \text{ m}^2/\text{g}$) times solvent exchange.	60
Figure 4.4. DMF content in MOF-5 after multiple solvent exchanges determined by 1H -NMR.	61
Figure 4.5. 1H -NMR spectroscopy monitoring of the amount of DMF diffusing into CH_2Cl_2 for MOF-5 and IRMOF-2 during the first solvent exchange process. Concentration of DMF has been normalized for comparison. Inset: structures of	

MOF-5 and IRMOF-2 (space filling representation, color code: white, H; grey, C; red, O; blue, Zn; maroon, Br)	61
Figure 4.6. N ₂ isotherm plots of UMCM-9 activated from n-hexane and CH ₂ Cl ₂ exchanged materials. (Adsorption data are shown in full symbols while desorption data are shown in hollow symbols) Inset: Structure of UMCM-9 (Zn ₄ O(naphthalene-2,6-dicarboxylate) _{1.5} (biphenyl-4,4'-dicarboxylate) _{1.5}).....	62
Figure 4.7. PXRD patterns of UMCM-9. a) Simulated, b) conventional solvent exchange activation from n-hexane.	62
Figure 4.8. N ₂ isotherm plot of UMCM-9 activated from n-hexane under different evacuation rates. Inset: BET surface area of activated UMCM-9 with different evacuation rates.....	63
Figure 4.9. N ₂ isotherm plots of FJI-1 activated from perfluoropentane and n-hexane exchanged materials. (Adsorption data are shown in full symbols while desorption data are shown in hollow symbols) Inset: Structure of FJI-1 (Zn ₂ (benzene-1,3,5-tribenzoate) _{4/3} (4,4'-bipyridine)).....	63
Figure 4.10. PXRD patterns of FJI-1. a) Simulated, b) conventional solvent exchange activation from perfluoropentane.....	64
Figure A.1. Synthesis of 2,5,8,11-tetrakis(4-carboxyphenyl)perylene H ₄ L (cod=1,5-cyclooctadiene; dba=dibenzylideneacetone).....	75
Figure A.2. a) Structure of UMCM-310 with large pore (blue) and small pore (green) indicated. b) Structure of mesoporous cage (large pore). c) Large pore window with Cu-Cu distance measured to be 16.6 Å.....	75
Figure A.3. N ₂ -sorption isotherm of UMCM-310 (●adsorption, ○desorption). Inset: Pore-size distribution from NLDFT fitting of the Ar-sorption isotherm.	76
Figure A.4. Liquid-phase separation of nitrobenzenes on a UMCM-310 packed column at a flow rate 1 mL/min: a) mixture of nitrobenzene, o-dinitrobenzene, and 1,3,5-trinitrobenzene (λ=219 nm); and b) mixture of nitrobenzene, p-dinitrobenzene,	

and 1,3,5-trinitrobenzene ($\lambda=240$ nm). 76

Figure A.5. Liquid-phase separation of nitrotoluenes on a UMCM-310 packed column at a flow rate 1.5 mL/min: a) mixture of 2,4-dinitrotoluene and 2,4,6-trinitrotoluene ($\lambda=224$ nm); and b) mixture of 2,4-dinitrotoluene, 2,6-dinitrotoluene ($\lambda=227$ nm). 77

Figure A.6. Liquid-phase separation of a mixture of 1,3,5-triphenyl benzene and 1,3,5-tris(4-bromobenzyl)benzene on a UMCM-310 packed column (flow rate 1.5 mL/min; $\lambda=260$ nm). 77

List of Tables

Table 3.1. Summary of linker shape, cluster connectivity, predicted topology based on prediction framework from this work and experimental determined topology from reported Zr MCPs based on tetratopic linker	45
Table 3.2. Summary of linker shape, cluster connectivity and predicted topology mentioned in Figure 3.6 (prediction framework).....	47
Table 3.3. Crystal Data and Structure Refinements for UMCM-312 and UMCM-313. ..	49
Table 4.1. DMF content per unit cell after each solvent exchange determined by ¹ H-NMR spectroscopy.....	64
Table A.1. Resolution of compounds separated by liquid chromatography using UMCM-310 as stationary phase	78

Abstract

Microporous coordination polymers (MCPs), a class of materials composed of metal clusters connected by organic linkers, generally provide superior porosity, tunable pore size, and pore shape when compared to traditional sorbents such as activated carbon, zeolites and silica. In spite of the discovery of a vast number of MCPs, the design of MCPs with targeted structure and porosity is still largely an empirical exercise. In this thesis, two key aspects towards achieving targeted MCP structure and porosity are discussed to address this problem. The first aspect focuses on the design and control of MCP structures using additives to alter structure formation and geometric analysis of linkers with an emphasis on shape and flexibility. The second aspect involves exploratory research into critical steps in the MCP activation process involving solvent exchange and solvent evacuation to reveal inherent porosity.

Among efforts towards targeted MCP structures, strategies such as applying additives and geometric analysis of linkers are found to be effective in precise control over MCP structures and porosity. In the first strategy, additives, such as monocarboxylic acids, were found to play a crucial structural role in a newly discovered 2D Zr MCP, UMCM-309a. The additives can be incorporated and then subsequently removed to affect the interlayer spacing of the resulting structure. The findings suggest the proper use of additives is an emerging synthetic approach leading to novel MCP structures. In the second strategy, an analysis of linker geometry and flexibility was performed in the context of achieving predicted topologies for tetratopic-linker based Zr MCPs. Tetratopic linkers were categorized into tetrahedral, planar square or planar rectangular groups with an emphasis on linker flexibility. A combination of these three linker shapes and known

Zr₆ cluster generates a prediction framework. Using this strategy, two new Zr MCPs (UMCM-312 and UMCM-313) were produced, both of which confirmed topology predictions, demonstrating the robustness of this predictive method for targeted MCP structures. Moreover, this strategy highlights the importance of understanding linker flexibility, an overlooked yet vital element of MCP design.

Activation failures in MCPs are common, leading to lower than predicted surface area and inconsistent/irreproducible gas-storage properties. To better understand activation and factors impacting this process, a detailed study of the critical steps in MCP activation was performed. It was discovered that solvent exchange kinetics are extremely fast, and minutes rather than days are appropriate for solvent exchange in many MCPs. Additionally, it has also been determined that very low surface tension solvents are critical in activating challenging MCPs. MCPs that failed to be activated previously can achieve predicted surface areas upon application of lower surface tension solvents, such as n-hexane and perfluoropentane. The insights aid in the efficient activation of MOFs in both laboratory and industrial settings towards targeted porosity.

Chapter 1: Introduction

1.1 Microporous Coordination Polymer

Microporous coordination polymers (MCPs) are a class of porous materials composed of organic ligands coordinated to metal clusters with well-defined 2D or 3D structures. These materials are described with varying terminology including metal-organic framework (MOF), porous coordination polymer (PCP), and porous coordination network (PCN). They are often named to reflect the location of discovery such as University of Michigan Crystalline Material (UMCM), University of Oslo (UiO), Northwestern University (NU) and Fujian Institute of Research on the Structure of Matter (FJI).

Microporous coordination polymers are a relatively new class of porous materials compared to traditional porous materials such as zeolites, silica, alumina oxide and activated carbon. The early works by Robson during 1989-1991¹⁻³ provided concepts and examples that would soon become the foundation of the microporous coordination polymer field. However, the materials discovered at this stage generally lacked permanent porosity in the absence of guests. In 1999, separate reports from Yaghi⁴ and Williams⁵ demonstrate the achievement of permanent porosity in two of the most prominent MCPs, MOF-5 and HKUST-1. Both of these materials are constructed of carboxylate based ligands connecting with metal clusters giving robust structures. Such assembly later became the standard practices in the rational design of MCPs and the field gained tremendous popularity due the high surface area, high accessible pore volume, uniform pore size distribution and tunable pore/aperture size. These features give MCPs advantages in a wide range of applications such as separations,⁶ gas storage,⁷ catalysis⁸

and sensing⁹ compared to traditional sorbents. Until 2016, there are more than 60000 MCP structures deposited in the Cambridge Structural Database (CSD) constructed from a variety of inorganic nodes and organic linkers. Extremely high porosity has been demonstrated with frameworks densities as low as 0.13 g/cm³,¹⁰ pore volumes up to 90% free volume,¹¹ and surface areas greater than 6000 m²/g.¹²

1.2 Key Elements in MCP Design

An attractive feature of MCPs is the highly modular nature of their structures. By judiciously selecting the organic linker and metal clusters, MCPs can be tailor made as frameworks with controlled pore size, shape and functionality for specific applications. In spite of the huge number of structures discovered, in reality it is extremely difficult to realize a targeted structure through only rational design. To address this challenge, key elements related to design and prediction strategy based on linker and metal clusters are discussed below.

1.2.1 Linkers

Organic ligands, referred as linkers when used as cluster-bridging units in the construction of MCPs, play a crucial part in determining the final structure of the extended 2D or 3D network in MCPs. A major effort has focused on linker geometry to achieve predictable design of MCPs with desired structural features and properties. Factors such as linker length, connectivity, and symmetry have all been utilized in the rational construction of MCPs.

In 2002, Yaghi and coworkers¹³ synthesized a series of MCPs named IRMOFs (abbreviated for isorecticular metal organic frameworks) with the same net/topology as the parent structure MOF-5 (also called IRMOF-1) where the ditopic carboxylate is lengthened and/or substituted with various functional groups. This resulted in MCPs with increasing surface area and tunable pore aperture/size. This strategy was later termed ‘reticular synthesis’ and considered a robust approach in generating structures that could

tune the surface area in a systematic way.¹⁴ However, this strategy only works with ditopic carboxylate linker. When extending it to more complicated cases such as polytopic linkers, unexpected structures and properties often arise. Furthermore, extended structures with lengthened linkers are more inclined to interpenetration and collapse upon solvent removal, thus limiting the application of the strategy.

As mentioned above, changing linker geometry would affect the resultant structure of the MCPs. Increasing the connectivity of the linker can also alter the way a linker is incorporated into the network. For example, the use of tetratopic tetrahedral linkers generally gives structures based on the cubic diamond network which is rarely realized with a ditopic linker. Among the reported literature, linker connectivity of 2, 3, 4, 6, 8 and 12 have been frequently used in the construction of linkers.¹⁵ The use of such different linker connectivity leads to various structures and topologies. Even bearing the same connectivity, two linkers with different symmetry can produce structures with vastly different topologies and porosities. The Matzger group explored less symmetric tritopic linkers for the design of MCPs. They explored an unsymmetrically substituted biaryl compound biphenyl-3,4',5-tricarboxylic acid and discovered a Cu-based MCP with a unique [3,4,6]-connected MCP with very high porosity and surface area.¹⁶ This is totally different topology from the Cu-based MCP HKUST-1 derived from the symmetric tritopic linker trimesic acid.

Once linker size and geometry is known, together with predefined metal cluster, the MCP structure can be anticipated on the premise of rigid and robust linker. It is generally assumed the carboxylate based linkers used in the construction of MCPs are rigid and robust. However, MOFs are far more flexible compared to traditional sorbents due to the incorporation of organic linkers. Flexibility proves to be prevalent in MCPs leading to structural breathing, linker rotation, swelling and subnetwork displacement. The flexibility phenomenon complicates the design and prediction of MCP structures.¹⁷

1.2.2 Metal Clusters

The metal cluster acts as nodes for linkers to connect into different frameworks. Similar to linkers, the metal cluster connectivity and geometry will influence structure formation. Unlike most linkers, metal cluster form in-situ during the synthesis of MCPs and can be influenced by a number of variables such as solvent type, temperature, concentration, and the presence of additives.¹⁸ In reality, it is difficult to predict the metal cluster formation simply based on the synthesis conditions. Tough, a few metal clusters have been repeatedly produced to effectively prepare MCPs with permanent porosity such as $Zn_4O(CO_2R)_6$, $Cu_2(CO_2R)_4$ and $Zr_6O_4(OH_4)(CO_2R)_{12}$. The basic zinc carboxylate cluster, an octahedral cluster with a connectivity of six, is featured in various high surface area MCPs including MOF-5,⁴ MOF-177,¹⁹ and UMCM-1.²⁰ The application of these high performance materials have been limited by low water stability of the cluster. Upon contact with moisture, the basic zinc cluster will degrade leading to collapsed structure and lower surface area.²¹ The search for more water stable metal cluster and frameworks leads to the wide use of the $Zr_6O_4(OH_4)^{12+}$ cluster in recent years. The $Zr_6O_4(OH_4)^{12+}$ cluster has been discovered in highly water stable and highly porous MCPs including UiO-66,²² PCN-222²³ and NU-1000.²⁴

1.2.3 Framework Topology

MCPs structures can be abstracted into a periodic net/structure with a specific topology. Structural chemists have worked for ages to enumerate, describe and classify such nets in solid state periodic structures.²⁵ Recently, the application of the topology knowledge to the MCP field leads to the Reticular Chemistry Structure Resource,²⁶ a tool that compiles a searchable database of periodic nets. The 3D nets database contains mainly structures of interest to designed synthesis. However, there are a huge number of possible structures, for examples, more than 100 different topologies are possible for linking tetrahedral building blocks into structures with only one kind of vertex.¹⁴ So it is

argued that only a small number of simple, high-symmetry topology will be of general importance. One such net **pcu**, possess only one vertex with a connectivity of six, is featured in MOF-5 and IRMOF series. In MOF-5, the $Zn_4O(CO_2)_6$ unit can be treated as one common vertex and joined by benzene links. If one identifies conditions reproducibly lead to a particular metal cluster, one should also be able to predict the underlying topology of the MOF structure knowing the geometry of the linker.

1.3 Microporous Coordination Polymer Activation

The inherent porosity of MCP can only be revealed when the solvent molecules used during the synthesis trapped inside the pores are removed. This process called activation is critical as lower surface area and porosity is usually obtained when the process is not properly performed. MCPs are usually synthesized under solvothermal conditions using high boiling point formamide solvent. Direct vacuum evacuation to remove the solvent molecules commonly leads to incomplete guest removal. To solve this problem, solvent exchange processes were used to exchange the high boiling point solvent to low boiling point solvent to facilitate solvent removal. This approach was first demonstrated in the activation of MOF-5.⁴ Since then, this approach has been applied to numerous examples successfully leading to theoretical surface area. However, structure collapse does still happen frequently even when the solvent exchange process is applied. This is especially true for highly porous fragile Zn based MCP. In 2008, the Hupp group²⁷, drawing on inspiration from aerogel production, proposed using supercritical CO_2 ($scCO_2$) to process the MCP. It is theorized that $scCO_2$ possess no surface tension and will generate no capillary force during guest removal. It is demonstrated this method is extremely effective in achieving full surface area for MCPs that previously failed to be activated. However, it requires specialized instrument and is relatively low throughput, thus limiting its wide applications.

1.4 Organization of Thesis

In spite of the discovery of such a huge number of microporous coordination polymers, the design, synthesis, characterization and activation of MCPs is still largely an empirical exercise where trial-and-error, rather than design, is generally adopted. The research presented here serves to better understand factors impacting MCP design, synthesis and activation.

In chapter 2, the discovery of a series of novel 2D Zr-based MCP derived from the tritopic linker 1,3,5-(4-carboxylphenyl)benzene is described. These non-interpenetrated materials possess a rarely found six connected Zr cluster and demonstrated extremely high water stability and decent porosity. The use of different additives (monocarboxylates here) called modulators during the synthesis lead to similar 2D structures with different layer spacings. In contrast to conventional cases, the modulator plays key roles in forming the resultant structures.

Chapter 3 describes a design strategy based on geometric analysis of linker shape and flexibility. A prediction framework solely based on linker shape and cluster connectivity is developed in the context of achieving predictable topology of tetratopic-linker based Zr MCPs. Two new Zr MCPs (UMCM-312 and UMCM-313) are produced using designed linkers based on the strategy and the results fit well into our predictions. It is demonstrated that the uncertainty of targeting topologies in tetratopic-linker based Zr MCPs can be reduced by accounting for linker shape and flexibility.

Turning from design to activation, chapter 4 describes exploratory research into critical steps in MCP activation involving solvent exchange and solvent evacuation. It is discovered that solvent exchange kinetics are extremely fast, and minutes rather than days are appropriate for solvent exchange in many MCPs. It is also demonstrated that choice of very low surface tension solvent is critical in successfully activating challenging MCPs. MCPs that have failed to be activated previously can achieve

predicted surface areas provided that lower surface tension solvent such as n-hexane and perfluoropentane are applied. The insights herein aid in the efficient activation of MCPs in both laboratory and industrial setting.

The use of a perylene based MCP as sorbent in the applications for the separations of nitroaromatics are described in appendix A.

1.5 Figures

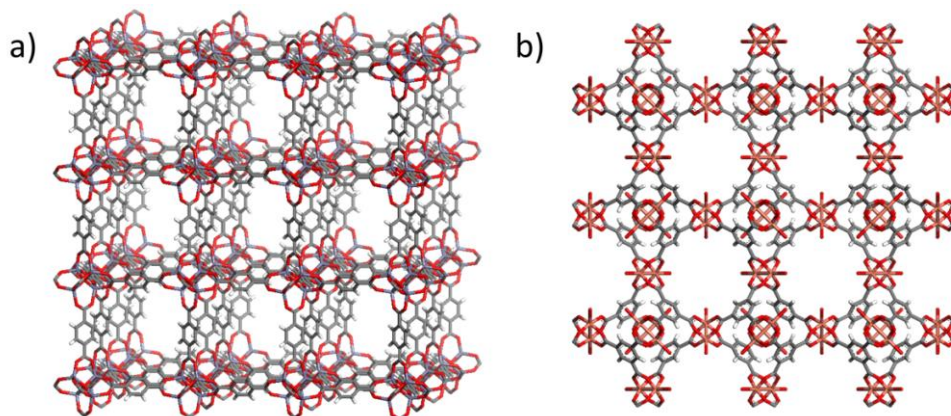


Figure 1.1 Structures of MCPs: a) MOF-5, and b) HKUST-1.

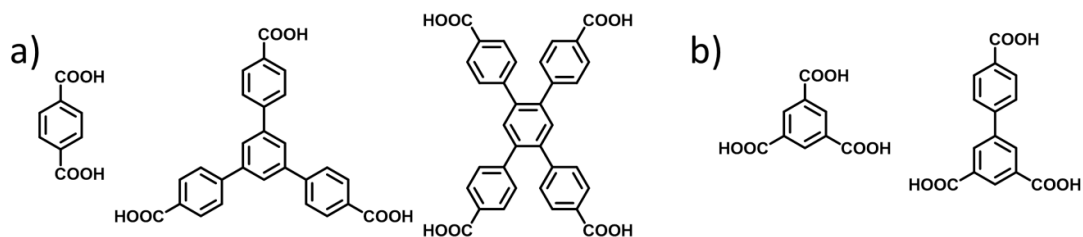


Figure 1.2 examples of linker used in the construction of MCPs a) with increased connectivity, b) same connectivity but with different geometry.

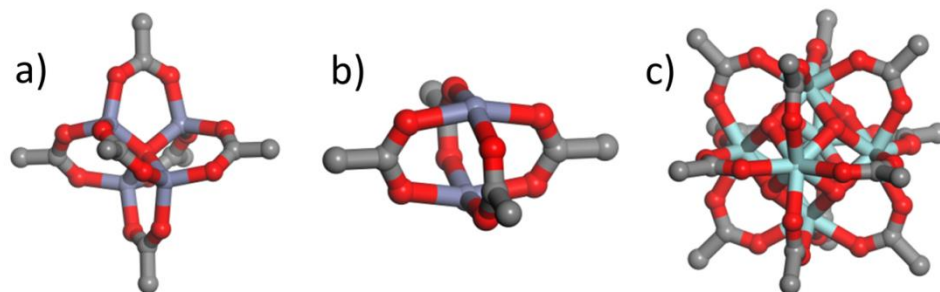


Figure 1.3 a) $\text{Zn}_4\text{O}(\text{CO}_2\text{R})_6$, b) $\text{Cu}_2(\text{CO}_2\text{R})_4$ and c) $\text{Zr}_6\text{O}_4(\text{OH}_4)(\text{CO}_2\text{R})_{12}$ metal cluster

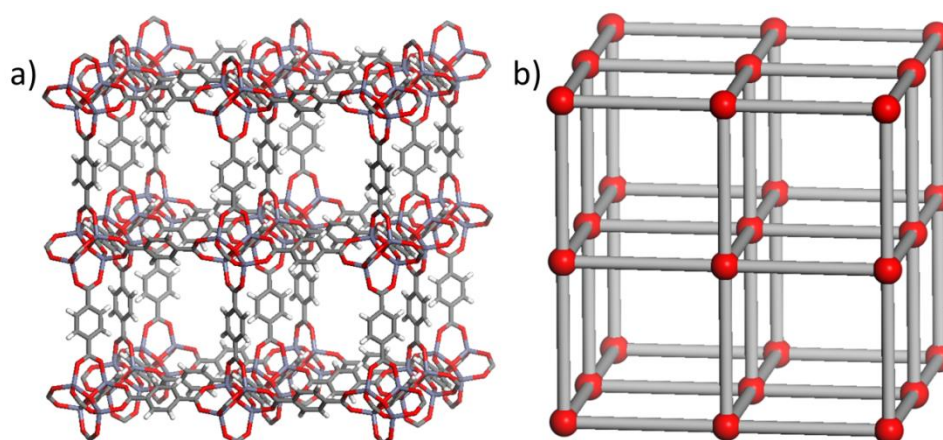


Figure 1.4 Structure of a) MOF-5 and its corresponding topology b) **pcu** net

1.6 References

- (1) Hoskins, B. F.; Robson, R. *J. Am. Chem. Soc.* **1989**, *111*, 5962.
- (2) Hoskins, B. F.; Robson, R. *J. Am. Chem. Soc.* **1990**, *112*, 1546.
- (3) Abrahams, B. F.; Hoskins, B. F.; Robson, R. *J. Am. Chem. Soc.* **1991**, *113*, 3606.
- (4) Li, H.; Eddaoudi, M.; O'Keeffe, M.; Yaghi, O. M. *Nature* **1999**, *402*, 276.
- (5) Chui, S. S.-Y.; Lo, S. M.-F.; Charmant, J. P. H.; Orpen, A. G.; Williams, I. D. *Science* **1999**, *283*, 1148.
- (6) Li, J.-R.; Sculley, J.; Zhou, H.-C. *Chem. Rev.* **2012**, *112*, 869.
- (7) Li, B.; Wen, H.-M.; Zhou, W.; Chen, B. *J. Phys. Chem. Lett.* **2014**, *5*, 3468.
- (8) Zhu, L.; Liu, X.-Q.; Jiang, H.-L.; Sun, L.-B. *Chem. Rev.* **2017**, *117*, 8129.
- (9) Kreno, L. E.; Leong, K.; Farha, O. K.; Allendorf, M.; Van Duyne, R. P.; Hupp, J. T. *Chem. Rev.* **2012**, *112*, 1105.
- (10) Furukawa, H.; Go, Y. B.; Ko, N.; Park, Y. K.; Uribe-Romo, F. J.; Kim, J.; O'Keeffe, M.; Yaghi, O. M. *Inorg. Chem.* **2011**, *50*, 9147.
- (11) Furukawa, H.; Ko, N.; Go, Y. B.; Aratani, N.; Choi, S. B.; Choi, E.; Yazaydin, A. Ö.; Snurr, R. Q.; O'Keeffe, M.; Kim, J.; Yaghi, O. M. *Science* **2010**, *329*, 424.
- (12) Koh, K.; Wong-Foy, A. G.; Matzger, A. J. *J. Am. Chem. Soc.* **2009**, *131*, 4184.

- (13) Eddaoudi, M.; Kim, J.; Rosi, N.; Vodak, D.; Wachter, J.; O'Keeffe, M.; Yaghi, O. M. *Science* **2002**, *295*, 469.
- (14) Yaghi, O. M.; O'Keeffe, M.; Ockwig, N. W.; Chae, H. K.; Eddaoudi, M.; Kim, J. *Nature* **2003**, *423*, 705.
- (15) Li, M.; Li, D.; O'Keeffe, M.; Yaghi, O. M. *Chem. Rev.* **2014**, *114*, 1343.
- (16) Wong-Foy, A. G.; Lebel, O.; Matzger, A. J. *J. Am. Chem. Soc.* **2007**, *129*, 15740-.
- (17) Schneemann, A.; Bon, V.; Schwedler, I.; Senkovska, I.; Kaskel, S.; Fischer, R. A. *Chem. Soc. Rev.* **2014**, *43*, 6062.
- (18) Qin, L.; Zheng, H.-G. *CrystEngComm* **2017**, *19*, 745.
- (19) Chae, H. K.; Siberio-Pérez, D. Y.; Kim, J.; Go, Y.; Eddaoudi, M.; Matzger, A. J.; O'Keeffe, M.; Yaghi, O. M. *Nature* **2004**, *427*, 523.
- (20) Koh, K.; Wong-Foy, A. G.; Matzger, A. J. *Angew. Chem. Int. Ed.* **2008**, *47*, 677.
- (21) Guo, P.; Dutta, D.; Wong-Foy, A. G.; Gidley, D. W.; Matzger, A. J. *J. Am. Chem. Soc.* **2015**, *137*, 2651.
- (22) Cavka, J. H.; Jakobsen, S.; Olsbye, U.; Guillou, N.; Lamberti, C.; Bordiga, S.; Lillerud, K. P. *J. Am. Chem. Soc.* **2008**, *130*, 13850.
- (23) Feng, D.; Gu, Z.-Y.; Li, J.-R.; Jiang, H.-L.; Wei, Z.; Zhou, H.-C. *Angew. Chem. Int. Ed.* **2012**, *51*, 10307.
- (24) Mondloch, J. E.; Bury, W.; Fairen-Jimenez, D.; Kwon, S.; DeMarco, E. J.; Weston, M. H.; Sarjeant, A. A.; Nguyen, S. T.; Stair, P. C.; Snurr, R. Q.; Farha, O. K.; Hupp, J. T. *J. Am. Chem. Soc.* **2013**, *135*, 10294.
- (25) Delgado Friedrichs, O.; O'Keeffe, M.; Yaghi, O. M. *Acta Crystallogr., Sect. A* **2003**, *59*, 22.
- (26) O'Keeffe, M.; Peskov, M. A.; Ramsden, S. J.; Yaghi, O. M. *Acc. Chem. Res.* **2008**, *41*, 1782.
- (27) Nelson, A. P.; Farha, O. K.; Mulfort, K. L.; Hupp, J. T. *J. Am. Chem. Soc.* **2009**, *131*, 458.

Chapter 2: The Role of Modulator in Controlling Layer Spacings in a Tritopic Linker Based Zirconium 2D-Microporous Coordination Polymer[†]

2.1 Introduction

Coordination polymers have seen extensive development in the nearly 100 years since their first description.^{1,2} The delineation of the design principles for porous solids with controlled structure took place a few decades ago through the work of Robson.³ These materials suffered from a lack of porosity in the absence of guests and in 1999 two fantastic examples of porous coordination polymers with permanent porosity were described heralding the area of what is now commonly referred to as MOFs (metal-organic frameworks) or MCPs (microporous coordination polymers).^{4,5} These early examples suffered from water sensitivity but rapid advances led to porous materials with more hydrolytically stable metal clusters broadening the potential applicability of these materials in a host of gas storage and separations applications. Stable Al⁶- and Cr^{7,8}-based MCPs were more recently joined by those based on Zr⁹⁻¹¹ and now MCPs are proving to be excellent desiccants for humid gas streams.^{12,13} With increased stability came poorer crystallinity and indeed single crystals are unattainable for many of the newest water stable MCPs whereas traditional Zn- and Cu-based MCPs often readily form large single crystals. This has put an increased emphasis on alternative characterization techniques for MCPs and here the synthesis, structure elucidation, and interplay of reversible coordination chemistry with cluster geometry of Zr MCPs built from a tritopic linker is discussed.

[†] Published: Ma, J.; Wong-Foy, A. G.; Matzger, A. J. *Inorg. Chem.* **2015**, *54*, 4591.

Currently, most Zr MCPs are built with ditopic linkers. The first example, UiO-66, uses terephthalic acid as the linker.^{14,15} The $Zr_6O_4(OH)_4(RCO_2)_{12}$ cluster in this material has been shown to be one common mode of assembly and by changing the length of the ditopic linker, Zr MCPs with the same topology (**fcu** net) and Zr_6 cluster are typically achieved with different pore sizes and surface areas. Another common class of linkers used in Zr MCP construction is tetratopic linkers such as porphyrin-based tetracarboxylic acids. These linkers generate MCPs with different topologies. For example, in PCN-222(Fe),¹⁶ the Zr MCP constructed based on Fe-TCPP (TCPP = tetrakis(4-carboxyphenyl)porphyrin) adopts a **csq-a** net, whereas the same linker geometry also results in PCN-224¹⁷ with a **she** net and PCN-225¹⁸ with a **sqc** net. The change in linker geometry also affects the Zr_6 cluster (A summary of common Zr_6 clusters is shown in Figure 2.1 and Figure 2.2). In the UiO series of MCPs, each Zr_6 cluster is nominally

12 connected to the linkers. In the cases of PCN-222(Fe), PCN-224 and PCN-225, the Zr_6 cluster is only 8-, 6-, and 6-connected respectively. Whereas tritopic linkers are a common class of linkers in building Zn- or Cu-based MCPs, they are rarely used in building Zr MCPs. Only three Zr MCPs are found in the literature based on a tritopic linker. MOF-808 is built from trimesic acid and adopts the **spn** net.¹³ The cluster in this case is also different from the common 12-connected cluster being only 6-connected. A second example is based on $H_3BTB(1,3,5-(4\text{-carboxylphenyl})\text{benzene})$, a more extended tritopic linker than trimesic acid that possesses the same geometry, and is interpenetrated as well being much less stable compared to other 3D Zr MCPs.¹⁹ The most recent addition, PCN-777, is constructed from the 4,4',4''-s-triazine-2,4,6-triyl-tribenzoate (TATB, which is BTB having a central ring substitution and otherwise identical topology) linker with a 6 connected Zr_6 cluster.²⁰

2.2 Results and Discussion

Here we present a new Zr MCP, UMCM-309a, derived from the tritopic linker

H₃BTB. Our first attempts to synthesize new materials using H₃BTB and ZrCl₄ resulted in amorphous products. This is a common issue encountered in Zr MCP chemistry, a likely result of the poor reversibility of network formation. The use of modulators, such as monocarboxylic acid, has been applied to increase the crystallinity of Zr MCPs.²¹ When added at sufficiently high concentrations, modulators slow crystal growth affording increased crystallinity of the MCP.²² By using concentrated HCl as modulator, a crystalline phase was obtained (UMCM-309a). By using monocarboxylic acids as modulator, including benzoic acid and biphenyl-4-carboxylic acid, the crystallinity of the product was further increased. However, suitable single crystals could not be obtained for further structural elucidation. These new phases (benzoic acid = UMCM-309b, biphenyl-4-carboxylic acid = UMCM-309c) are closely related to those arising from HCl and the relationship among these materials is discussed below.

Without a suitable single crystal to determine the structure, we turn to the approach that was applied to find model structures for covalent organic frameworks.²³ The general work flow is: a) index the PXRD pattern to determine the unit cell and crystal system; b) determine connectivity of the linker and cluster to find potential topologies in the Reticular Chemistry Structure Resource (RCSR).²⁴ Ensure that the topology is consistent with geometry information of the cluster and linkers as well as indexing results; c) build models based on vertex information from the topology; d) optimize and refine the structure against the experimental PXRD pattern. Indexing the PXRD pattern of UMCM-309a (material synthesized from HCl as modulator), the unit cell was determined to be hexagonal with $a=b=20.06$ Å, $c=7.07$ Å, $\alpha=\beta=90^\circ$, $\gamma=120^\circ$. The very short c -axis pointed to the likely involvement of a 2D layered structure. The next step is to identify potential topologies consistent with the indexing information and other geometry information like cluster geometry arrangement. BTB acts as a 3 connector whereas the Zr₆ cluster is commonly found to be 6-, 8-, 10- or 12-connected. Theoretically possible topologies based on different connectivity of vertices have been derived and compiled

into the RCSR database. Searches based on 3, 6; 3, 8; 3, 10 and 3, 12 connectivity were conducted. Only **tfz-d**, **anh** nets and **bru**, **kgd** layers were found to be in the hexagonal group. The **tfz-d** and **anh** topology were excluded because the geometry of the 8-connected unit is not compatible with the Zr_6 cluster shape. The **bru** topology was ruled out because it incorporates a pyramidal 3-connected unit which is not accessible for BTB. The **kgd** binodal 3,6-c 2D kagome hexagonal net is consistent with indexing results and geometry information. Accordingly we chose **kgd** as the starting point for modeling. The BTB linker and Zr_6 cluster were placed in the unit cell with cell parameters obtained from indexing in an arrangement consistent with the vertex information of the **kgd** topology. In fact this topology is the same as the previously reported Zr/BTB phase¹⁹ though, as shown below, the materials are distinct with regard to structure and reactivity. The model was geometry optimized with the Forcite module of Material Studio using the smart algorithm and Universal Force Field with ultra-fine convergence tolerance to give the final structure (Figure 2.3). In the last step, the calculated PXRD pattern was compared with the experimental one and good agreement was found. A Pawley refinement was performed on the PXRD pattern to give the final cell parameters. The final refined unit cell for UMCM-309a is $a=b=19.54 \pm 0.03 \text{ \AA}$, $c=7.01 \pm 0.01 \text{ \AA}$, $\alpha=\beta=90^\circ$, $\gamma=120^\circ$, $R_p = 3.64\%$, $R_{wp} = 5.81\%$ (Figure 2.4). These results further confirmed the topology chosen for modeling. In other cases, if there are several potential topologies suitable for modeling, all topologies should be tried to model the structure and each compared to experimental data to determine the best possible fit.

In the final structure for UMCM-309a (Figure 2.3), each cluster connects to six BTB ligands. The remaining sites are coordinated with six hydroxyl groups and six water molecules to give a neutral framework: $[Zr_6(\mu_3-O)_4(\mu_3-OH)_4(BTB)_2(OH)_6(H_2O)_6]$. This assignment is in reasonable accord with elemental analysis and TGA data (Figure 2.5) although the high carbon content suggests that residual BTB remains in the pores either as a guest or through coordination to the cluster (vide infra). A nitrogen isotherm was

collected on this phase. A BET surface area of 810 m²/g was obtained which is comparable to UiO-66 (Figure 2.6). The previously reported Zr/BTB phase, an interpenetrated version of the present material, has a BET surface area of 713 m²/g.¹⁹ The interpenetrated phase is claimed to have much lower stability compared to other 3D Zr MCPs. It is therefore surprising that UMCM-309a is found to be stable towards water and HCl solution for four months (Figure 2.7).

We now turn to the role of modulator. While modulators are extensively used in Zr MCP synthesis to increase crystallinity, they are often assumed to be removed from the framework after washing with polar solvents like DMF. However, it has been shown that modulators can function as defect sites in the framework or coordinate to the free sites of the cluster. In those cases, washing with DMF does not remove modulators coordinated to the cluster. Harsh conditions like treating MCPs with HCl in DMF at 120 °C help to remove all modulators. In such cases, removing modulators does not change the overall structure.^{16,25} Presented here is a contrasting case where the modulator plays both a role in forming the structure and continues to exert influence upon removal.

When monocarboxylate modulators were examined (benzoic acid and biphenyl-4-carboxylic acid), a dramatic change in PXRD patterns was observed compared to that of UMCM-309a indicating a change in overall structure. Attempts to activate these phases through solvent exchange and supercritical CO₂ activation^{26,27} generated nonporous materials in contrast to the porous UMCM-309a. It was found that the new phases are not stable in air and the PXRD patterns changed upon solvent loss albeit with retention of the two main peaks with peak positions corresponding to the (1,0,0) and (1,1,0) reflections (Figure 2.8). This suggests that the layered structure is still intact after the structure change. Thus it was hypothesized that the changes arising in the PXRD are attributable to the change in distance between the layers (*c*-axis). UMCM-309a possesses free hydroxyl sites that potentially can be substituted by monocarboxylic acid. Unlike more typical cases where the pillar linkers covalently bridge

between layers in pillar-layered MCPs such as D-MOF²⁸ and UMCM-10,-11,-12,²⁹ here monocarboxylic acid only coordinates to one layer leading to weak interaction between layers. This then results in structural change (collapse) specifically with regard to the distance between layers. NMR digestion of the as synthesized products using benzoic acid (UMCM-309b) and biphenyl-4-carboxylic acid (UMCM-309c) were performed and the ratio between the modulator and BTB was determined to be close to 6 to 2, which implies that each cluster coordinates to 6 modulators (Figure 2.9 and Figure 2.10). Furthermore, before and after solvent removal, the ratio does not change. The hypothesis that the modulators change the *c*-axis is further supported by analysis of the PXRD pattern. Considering the increase in the *c*-axis when modulators are coordinated to the free sites, new peaks related to the *c*-axis should emerge at lower 2θ angles. The PXRD pattern of UMCM-309c displays a new peak at $5.9^\circ 2\theta$ that is assigned as the (0,0,1) and related peaks, including (1,0,1), (1,1,1) and (2,0,1), can be found at the predicted positions based on the new unit cell parameters (Figure 2.11b). A preliminary model was generated for UMCM-309c and in this model the free hydroxyl sites are replaced by biphenyl-4-carboxylic acid resulting in a longer *c*-axis (14.8 Å) compared to 7.04 Å of UMCM-309a. The model was refined against the PXRD pattern giving fairly good agreement (Figure 2.11a and Figure 2.11c).

Washing UMCM-309c with DMF several times at room temperature did not change the ratio between modulator and BTB. These modulators can be removed when UMCM-309c (or UMCM-309b) is treated in a DMF/H₂O (or DMF/HCl) mixture at 120 °C. The PXRD pattern changes to exactly the same as UMCM-309a (Figure 2.12). The sharper peaks in the pattern indicate a more crystalline phase than previously obtained. After treatment and activation at 120 °C under vacuum, the MCP shows a surface area around 788 m²/g, a value closely matching that of UMCM-309a and consistent with complete conversion of UMCM-309c upon modulator removal (Figure 2.13). Modulator clearly plays more than a fleeting role in forming the structure here. In

the case of benzoic acid, perhaps the most commonly used modulator in Zr MCP synthesis, a more complex structure than the other two phases is obtained. This may arise from partial collapse or a more profound structural change than described above. However, here too the modulator is far from a spectator and instead is involved intimately in the resultant structure.

2.3 Conclusions

In this communication we report the synthesis and characterization of a Zr MCP based on a tritopic linker (H₃BTB). It possesses a 2D layer structure with a short *c*-axis. This porous phase is stable in aqueous conditions for over four months. The influence of using different modulators on the structure was also investigated and, in contrast to conventional cases, the modulators benzoic acid and biphenyl-4-carboxylic acid remain coordinated to the cluster. Clearly more attention needs to be focused on the role of modulator to ensure correct interpretation of structural results and the ability of modulator to yield novel structures represents an emerging synthetic strategy. Finally, the observation now of two phases of Zr/BTB with such dramatically different stabilities highlights the need for exhaustive searching of phase space to produce materials with desired properties from a given set of reactants.

2.4 Experimental Methods

Reagents. Zirconium tetrachloride (Acros, 98%), concentrated HCl (Fisher Scientific, ACS reagent grade), benzoic acid (Acros, 99.5%), biphenyl-4-carboxylic acid (Alfa Aesar, 98%) and dimethylformamide (DMF, Fisher Scientific, ACS reagent grade) were used as-received without further purification.

Powder X-ray diffraction. The powder X-ray data of UMCM-309a for Rietveld refinement were collected on Rigaku R-Axis Spider diffractometer with an image plate detector and Cu-K α radiation operating at 40 kV and 44 mA in transmission mode. The sample was loaded into a 0.4 mm diameter capillary. The capillary was rotated on the

goniometer in ϕ and oscillated in ω to minimize preferred orientation with χ fixed at 45° . Another image of a blank capillary was acquired in the same manner and subtracted from the sample image. The powder pattern then was obtained by integration of the two-dimensional image in AreaMax 2.0 software with an integration step of 0.01° . All other PXRD data were collected with a Bruker D8 advance diffractometer equipped with a 60 mm sealed Göbel mirror and a LynxEye linear position sensitive detector. The Cu-K α X-ray source was operated at 40 kV and 40 mA. Samples were ground and evenly dispersed on a low-background quartz plate.

Gas sorption measurements. Gas sorption experiments were carried out at 77K using a NOVA 4200 by Quantachrome Instruments (Boynton Beach, Florida, USA) or an Autosorb-1C Quantachrome Instruments (Boynton Beach, Florida, USA). Ultra-high purity N₂ (99.999%) and Ar (99.999%) was purchased from Cryogenic Gasses and used as received. Pore size distributions were calculated using the Non-linear Density Functional Theory (NLDFT) zeolite/silica equilibrium kernel on a cylindrical pore model for Ar adsorption at 87 K using ASWin software package (version 1.2).

Thermogravimetric analysis. TGA data were acquired using a TA instrument Q50. Samples were heated and analyzed in a platinum pan under a nitrogen atmosphere. Temperature was ramped up to 600 °C at a rate of 10 °C/min.

NMR analysis. NMR data were obtained using a 500 MHz Varian Inova NMR spectrometer. A relaxation time of 25 s was applied to ensure full relaxation and accurate integration.

Scanning Electron Microscopy. Activated UMCM-309a (~2-3 mg) was transferred to conductive carbon tape on a sample holder with no coating performed. A Zeiss 1455VP instrument was used for acquiring images at 10 kV with a 5 mm working distance under vacuum.

General synthetic procedures for UMCM-309a. ZrCl₄(0.0863 g, 0.370 mmol) and H₃BTB (0.1095 g, 0.250 mmol) were dissolved in 10 mL of *N,N*-dimethylformamide

(DMF) in a 20 mL vial. Concentrated HCl(10.75 mL, 100 equiv.) was added to the solution. The mixture was sonicated for 10 minutes. The solution was transferred to a Parr 45 mL acid digestion vessel, sealed and heated to 120 °C. After 2 days, white microcrystalline powder was obtained. The powder was collected by centrifugation and washed with clean DMF (3 × 20 mL). The powder was then immersed in 10 mL acetone for 3 days, during which time the acetone was replaced three times each day. After exchange with acetone, the sample was evacuated at 120 °C under dynamic vacuum for 12 h prior to sorption analysis. The yield of the reaction, determined from the weight of the solvent-free material, is 17.3% based on H₃BTB. Anal. Calcd for [Zr₆(μ₃-O)₄(μ₃-OH)₄(BTB)₂(OH)₆(H₂O)₃]•0.5(BTB) which is equivalent to Zr₆O₂₉C₅₄H₄₆ 0.5(C₂₇H₁₅O₆): Zr, 28.45%; C, 42.13%; H, 2.81%. Found: Zr, 28.70%; C, 42.09%; H, 2.75%.

General synthetic procedures for UMCM-309b and UMCM-309c. ZrCl₄(0.0345 g, 0.148 mmol), H₃BTB (0.0438 g, 0.100 mmol) and modulators (100 equiv. benzoic acid or biphenyl-4-carboxylic acid) were dissolved in 4 mL of DMF in a 20 mL vial. The mixture was sonicated for 10 mins. The solution was then heated at 120 °C. After two days, white microcrystalline powder was obtained and subjected to the same washing procedure for UMCM-309a.

Model structure building, geometry optimized and refinement procedures. A unit cell was created in Material Studio 7.0 using PXRD indexing results. A Zr₆ cluster and BTB linker were placed in the unit cell according to the connectivity of the kgd-a network. The unit cell was subjected to geometry optimization with a UFF forcefield and convergence conditions from coarse to ultra-fine were applied sequentially using default parameters. A Pawley refinement was applied to the model against the powder pattern sequentially with specimen displacement, background, lattice parameters, peak profile, and peak asymmetry. The convergence quality was applied starting from coarse to ultra-fine to give the final unit cell parameters.

2.5 Figures

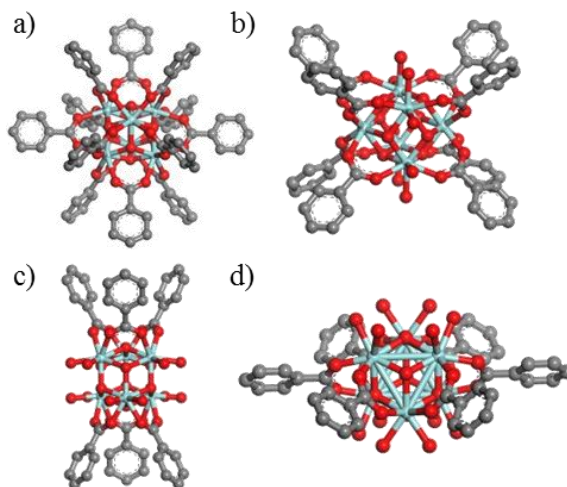


Figure 2.1. Summary of common Zr₆ clusters with different coordination numbers: a) 12 coordinate, b) 8 coordinate, c) 6 coordinate (trigonal prismatic), d) 6 coordinate (hexagonal planar).

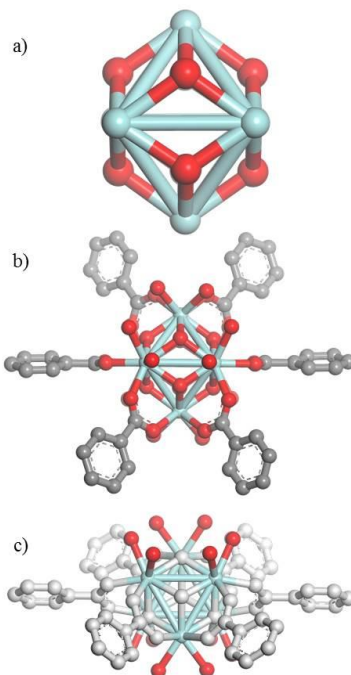


Figure 2.2. a) Octahedral core of the Zr₆ cluster. Four of the μ₃-O on the face of the octahedral are hydroxyl b) A Zr₆ cluster with 6 coordinate (hexagonal planar) arrangement of ligands. c) A Zr₆ cluster with 6 coordinate (hexagonal planar) arrangement of ligands highlighting terminal oxygen demonstrating coordination environment for Zr centers in UCMCM-309a.

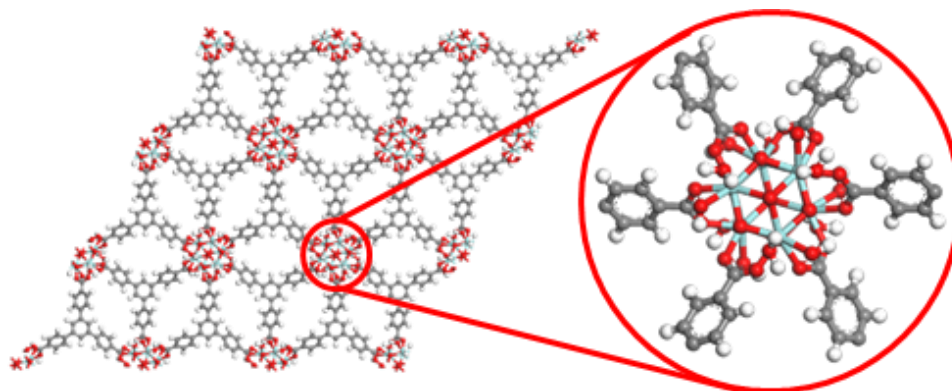


Figure 2.3. Model structure of UMCM-309a and expansion of a single Zr₆ cluster.

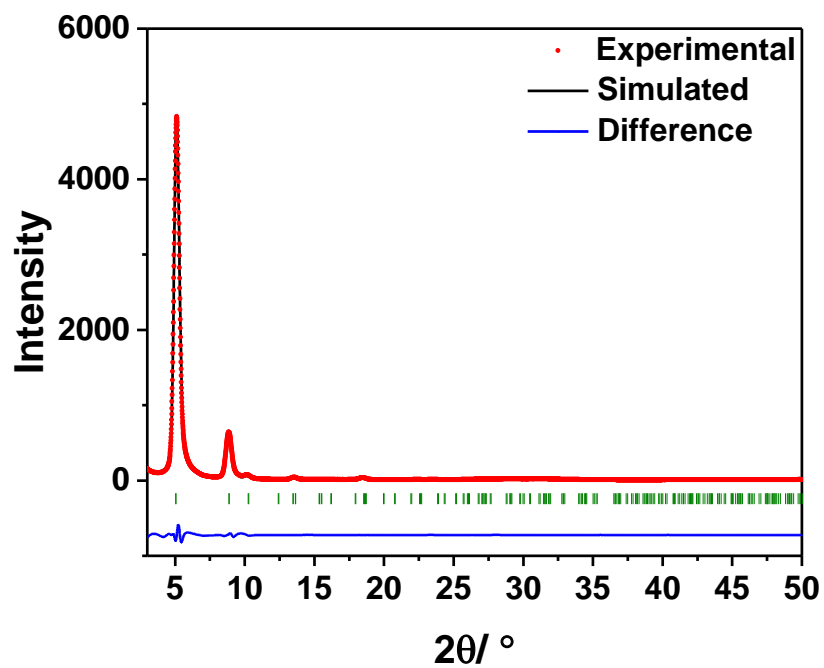


Figure 2.4. Results of Pawley refinement for UMCM-309a.

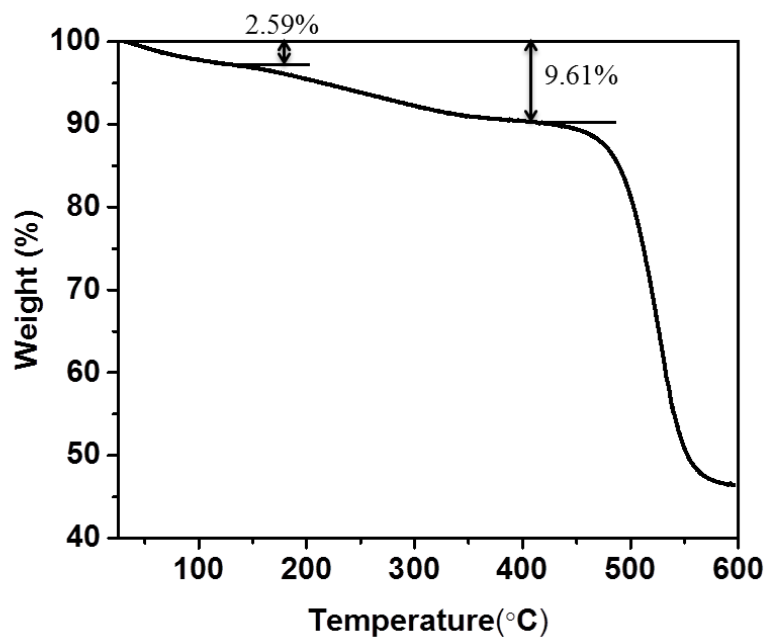


Figure 2.5. TGA trace of UMCM-309a. Conditions: temperature ramp from 25 °C to 600 °C at 10 °C/min under flow of N₂ gas.

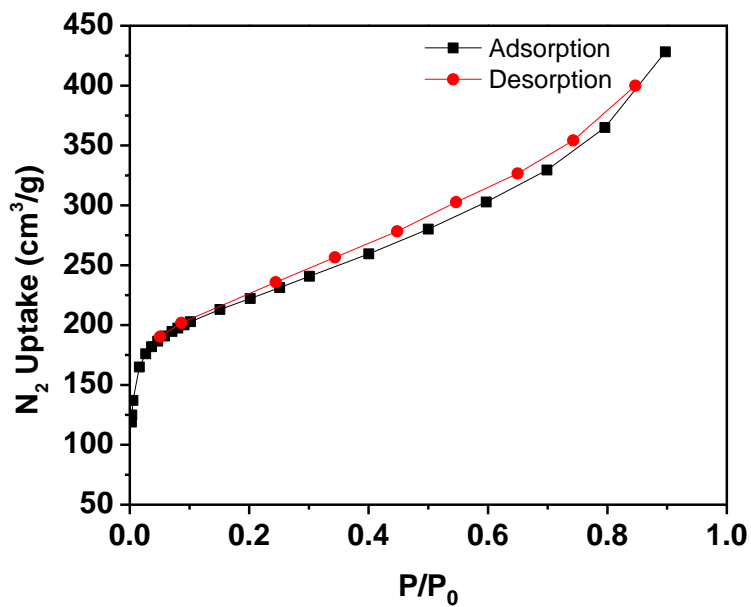


Figure 2.6. N₂ isotherm at 77 K for UMCM-309a

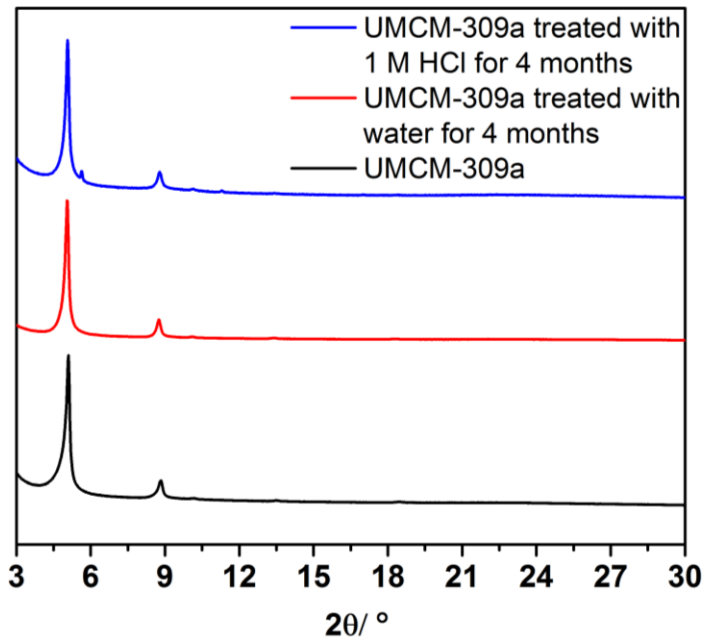


Figure 2.7. PXRD pattern of UMCM-309a and UMCM-309a treated with water and 1 M HCl for 4 months at room temperature.

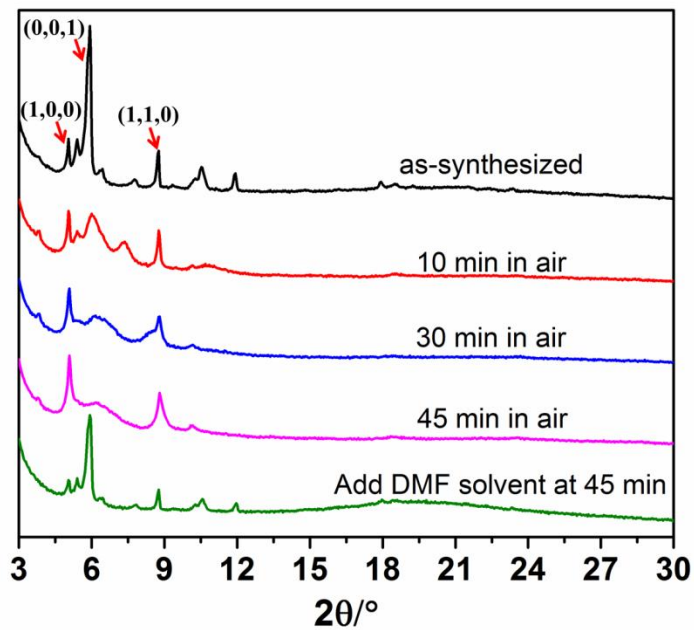


Figure 2.8. PXRD pattern of UMCM-309c as-synthesized and the pattern for UMCM-309c after 10 min, 30 min and 45 min in air. After 45 min in air, another PXRD pattern was obtained after adding DMF to the dried UMCM-309c.

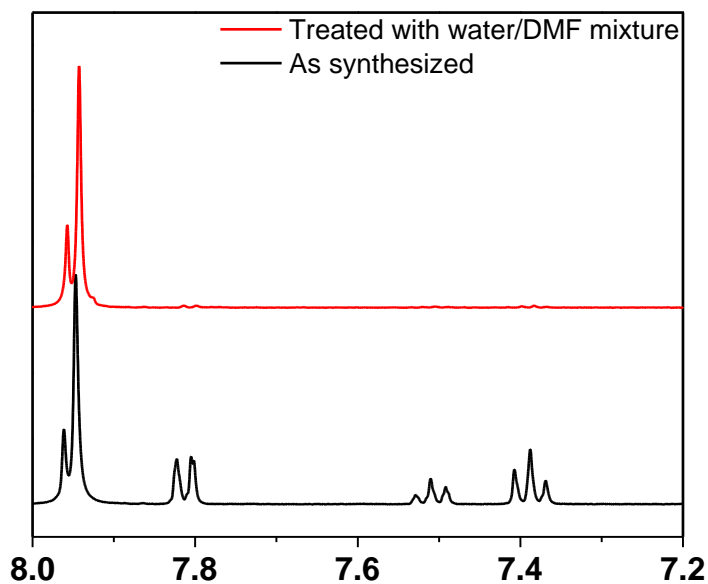


Figure 2.9. ^1H spectrum of digested UMCM-309b before and after treatment with water/DMF at $120\text{ }^\circ\text{C}$ for 3 days. Samples were digested with 10 wt% $\text{D}_2\text{SO}_4/\text{DMSO-d}_6$. From integration, the ratio between H_3BTB and benzoic acid was determined to be 2:4.84.

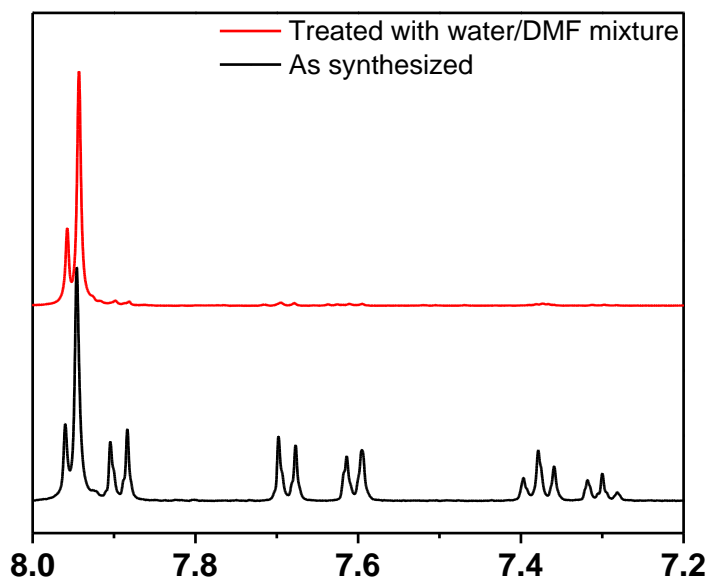


Figure 2.10. ^1H spectrum of digested UMCM-309c before and after treatment with water/DMF at $120\text{ }^\circ\text{C}$ for 3 days. Samples were digested with 10 wt% $\text{D}_2\text{SO}_4/\text{DMSO-d}_6$. From integration, the ratio between H_3BTB and biphenyl-4-carboxylic acid was determined to be 2:5.32.

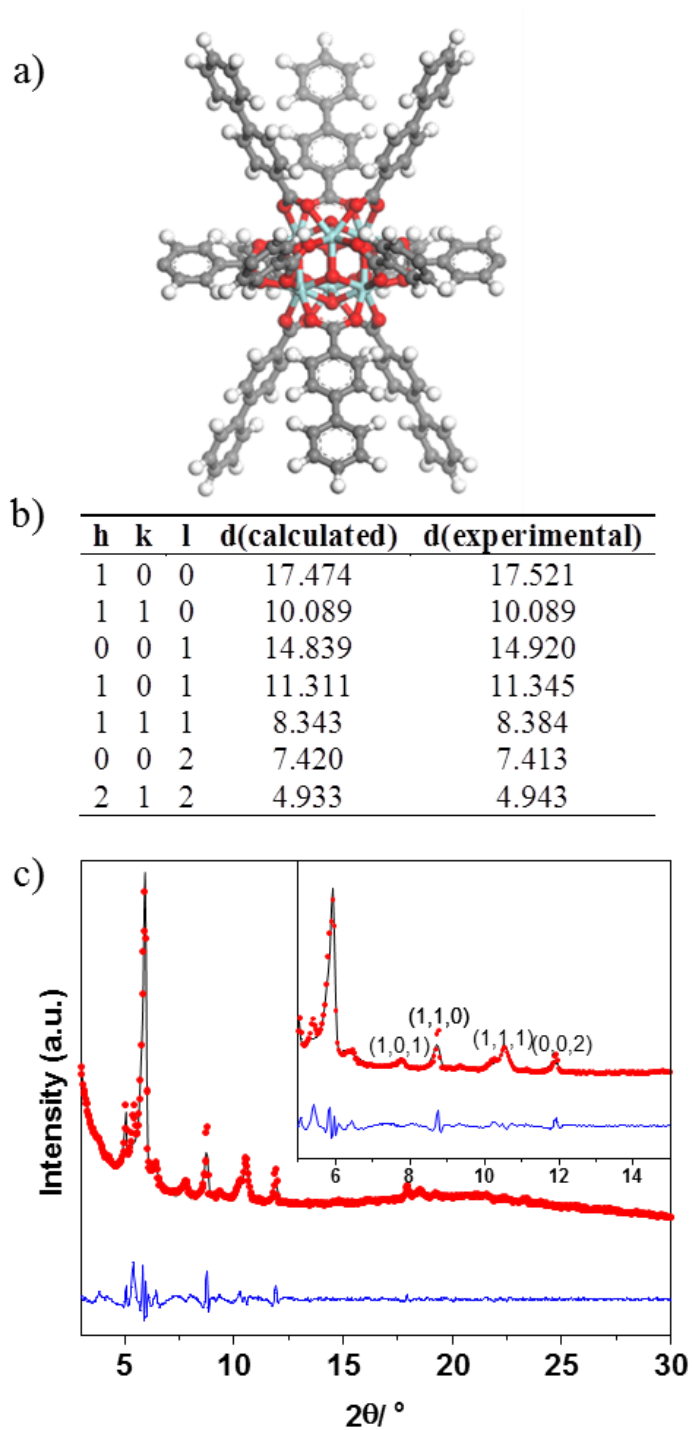


Figure 2.11. a) Biphenyl-4-carboxylate coordinated to the free sites of the Zr_6 cluster.
 b) Experimental and calculated peak positions of UMCM-309c based on a c -axis of 14.8 Å.
 c) Results of Pawley refinement for UMCM-309c.

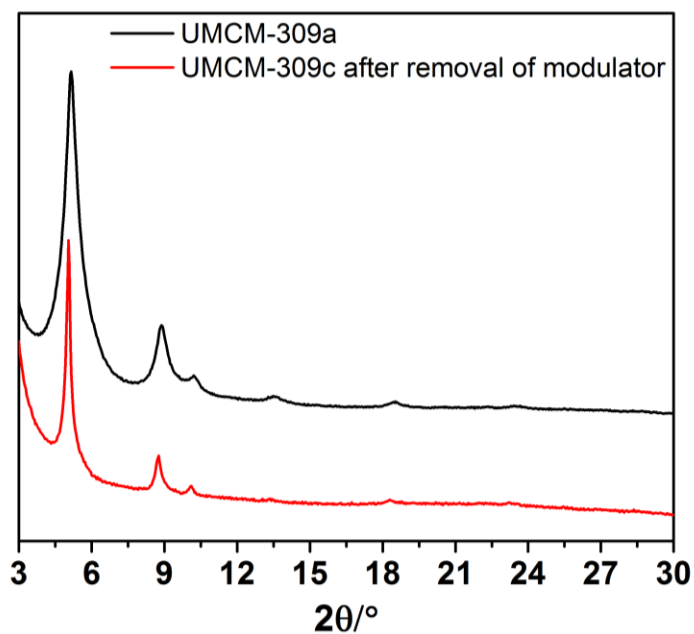


Figure 2.12. PXRD pattern of UMCM-309a and the pattern for UMCM-309c treated with water/DMF mixture at 120 °C for three days.

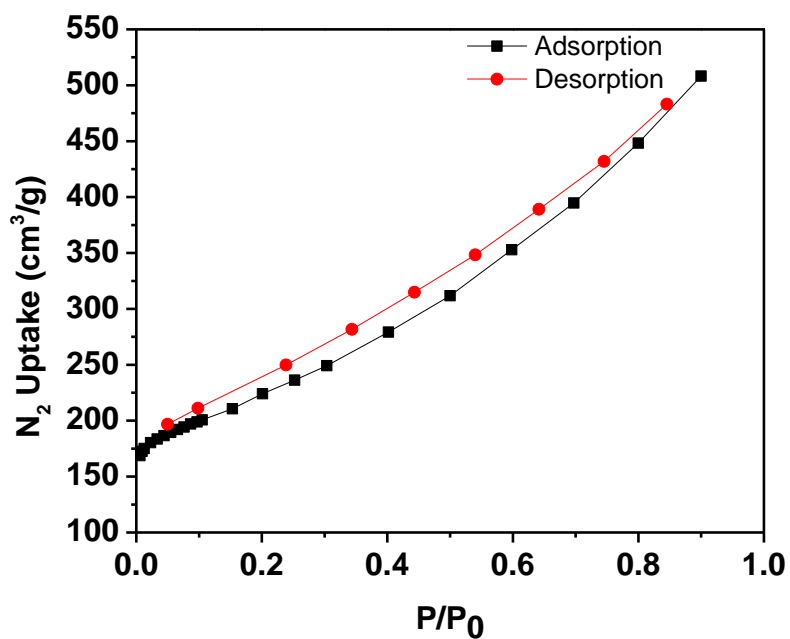


Figure 2.13. N_2 isotherm at 77 K for UMCM-309c treated with water/DMF mixture at 120 °C for three days.

2.6 References

- (1) Shibata, Y. *J. Coll. Sci., Imp. Univ. Tokyo* **1916**, *37*, 1.
- (2) Batten, S. R.; Champness, N. R.; Chen, X.-M.; Garcia-Martinez, J.; Kitagawa, S.; Ohrstrom, L.; O'Keeffe, M.; Suh, M. P.; Reedijk, J. *CrystEngComm* **2012**, *14*, 3001.
- (3) Hoskins, B. F.; Robson, R. *J. Am. Chem. Soc.* **1989**, *111*, 5962.
- (4) Li, H.; Eddaoudi, M.; O'Keeffe, M.; Yaghi, O. M. *Nature* **1999**, *402*, 276.
- (5) Chui, S. S.-Y.; Lo, S. M.-F.; Charmant, J. P. H.; Orpen, A. G.; Williams, I. D. *Science* **1999**, *283*, 1148.
- (6) Loiseau, T.; Serre, C.; Huguenard, C.; Fink, G.; Taulelle, F.; Henry, M.; Bataille, T.; Férey, G. *Chem. Eur. J.* **2004**, *10*, 1373.
- (7) Férey, G.; Mellot-Draznieks, C.; Serre, C.; Millange, F.; Dutour, J.; Surblé, S.; Margiolaki, I. *Science* **2005**, *309*, 2040.
- (8) Serre, C.; Millange, F.; Thouvenot, C.; Noguès, M.; Marsolier, G.; Louër, D.; Férey, G. *J. Am. Chem. Soc.* **2002**, *124*, 13519.
- (9) Reinsch, H.; Stassen, I.; Bueken, B.; Lieb, A.; Ameloot, R.; De Vos, D. *CrystEngComm* **2015**, *17*, 331.
- (10) Bon, V.; Senkovska, I.; Baburin, I. A.; Kaskel, S. *Cryst. Growth Des.* **2013**, *13*, 1231.
- (11) Carboni, M.; Lin, Z.; Abney, C. W.; Zhang, T.; Lin, W. *Chem. Eur. J.* **2014**, *20*, 14965.
- (12) Guo, P.; Wong-Foy, A. G.; Matzger, A. J. *Langmuir* **2014**, *30*, 1921.
- (13) Furukawa, H.; Gándara, F.; Zhang, Y.-B.; Jiang, J.; Queen, W. L.; Hudson, M. R.; Yaghi, O. M. *J. Am. Chem. Soc.* **2014**, *136*, 4369.
- (14) Cavka, J. H.; Jakobsen, S.; Olsbye, U.; Guillou, N.; Lamberti, C.; Bordiga, S.; Lillerud, K. P. *J. Am. Chem. Soc.* **2008**, *130*, 13850.
- (15) Øien, S.; Wragg, D.; Reinsch, H.; Svelle, S.; Bordiga, S.; Lamberti, C.; Lillerud, K. P. *Cryst. Growth Des.* **2014**, *14*, 5370.
- (16) Feng, D.; Gu, Z.-Y.; Li, J.-R.; Jiang, H.-L.; Wei, Z.; Zhou, H.-C. *Angew. Chem., Int. Ed.* **2012**, *51*, 10307.
- (17) Feng, D.; Chung, W.-C.; Wei, Z.; Gu, Z.-Y.; Jiang, H.-L.; Chen, Y.-P.; Darendbourg, D. J.; Zhou, H.-C. *J. Am. Chem. Soc.* **2013**, *135*, 17105.
- (18) Jiang, H.-L.; Feng, D.; Wang, K.; Gu, Z.-Y.; Wei, Z.; Chen, Y.-P.; Zhou, H.-C. *J. Am. Chem. Soc.* **2013**, *135*, 13934.
- (19) Wang, R.; Wang, Z.; Xu, Y.; Dai, F.; Zhang, L.; Sun, D. *Inorg. Chem.* **2014**, *53*, 7086.
- (20) Feng, D.; Wang, K.; Su, J.; Liu, T.-F.; Park, J.; Wei, Z.; Bosch, M.; Yakovenko, A.; Zou, X.; Zhou, H.-C. *Angew. Chem., Int. Ed.* **2015**, *54*, 149.
- (21) Schaate, A.; Roy, P.; Godt, A.; Lippke, J.; Waltz, F.; Wiebcke, M.; Behrens, P. *Chem. Eur. J.* **2011**, *17*, 6643.
- (22) Wu, H.; Chua, Y. S.; Krungleviciute, V.; Tyagi, M.; Chen, P.; Yildirim, T.; Zhou, W. *J. Am. Chem. Soc.* **2013**, *135*, 10525.

- (23) Côté A. P.; Benin, A. I.; Ockwig, N. W.; O'Keeffe, M.; Matzger, A. J.; Yaghi, O. M. *Science* **2005**, *310*, 1166.
- (24) O'Keeffe, M.; Peskov, M. A.; Ramsden, S. J.; Yaghi, O. M. *Acc. Chem. Res.* **2008**, *41*, 1782.
- (25) Deria, P.; Mondloch, J. E.; Tylianakis, E.; Ghosh, P.; Bury, W.; Snurr, R. Q.; Hupp, J. T.; Farha, O. K. *J. Am. Chem. Soc.* **2013**, *135*, 16801.
- (26) Liu, B.; Wong-Foy, A. G.; Matzger, A. J. *Chem. Commun.* **2013**, *49*, 1419.
- (27) Nelson, A. P.; Farha, O. K.; Mulfort, K. L.; Hupp, J. T. *J. Am. Chem. Soc.* **2008**, *131*, 458.
- (28) Dybtsev, D. N.; Chun, H.; Kim, K. *Angew. Chem., Int. Ed.* **2004**, *43*, 5033.
- (29) Dutta, A.; Wong-Foy, A. G.; Matzger, A. J. *Chem. Sci.* **2014**, *5*, 3729.

Chapter 3: Towards Topology Prediction in Zr-Based Microporous Coordination Polymers: the Role of Linker Geometry and Flexibility[†]

3.1 Introduction

The field of microporous coordination polymers (MCPs) has enjoyed great progress in both design and application since the report of two fantastic examples of crystalline materials with exceptional pore structure in 1999: MOF-5¹ and HKUST-1². MCPs with new topologies and high surface area are being discovered at a stunning pace and such materials have attracted a great deal of interest for potential applications in gas storage,^{3,4} separations,⁵ catalysis,⁶ drug delivery,⁷ and sensing.^{8,9} However, one key limitation for the majority of practical applications is the generally low hydrolytic stability of MCPs. In recent years, a class of MCPs based on Zr has shown considerable promise in this regard. Zr-based MCPs have generally shown greatly improved hydrolytic stability compared to common Zn- or Cu-based MCPs. Additional advantages, such as production under mild synthetic conditions from inexpensive Zr salts derived from earth abundant ores, make Zr-based MCPs strong candidates for applications that were previously not practical for conventional MCPs.

The directed assembly of clusters and linkers having well defined geometries, dubbed reticular chemistry in the MCP literature, has proven to be a useful tool in targeting default topologies/nets;⁹ this is especially true with MCPs based on basic zinc carboxylate ($\text{Zn}_4\text{O}(\text{CO}_2\text{R})_6$) or paddlewheel (exemplified by $\text{Cu}_2(\text{CO}_2\text{R})_4$) clusters connected by ditopic linkers. When linker geometry and cluster connectivity become

[†] Published: Ma, J.; Tran, L. D.; Wong-Foy, A. G.; Matzger, A. J. *Cryst. Growth Des.* **2016**, *16*, 4148.

more complex, it is challenging to design MCPs and predict their topology. For example the design of Zr MCPs with ditopic linkers such as terephthalic acid (H_2BDC),¹¹ biphenyl-4,4'-dicarboxylic acid (H_2BPDC) and their derivatives¹² consistently results in the UiO-66-type structure (*fcu* net) which consists of linear linkers bridging 12-connected clusters. With more complex geometries, such as tritopic linkers like trimesic acid (H_3BTC) or 1,3,5-tris(4-carboxyphenyl)benzene (H_3BTB), topology is unpredictable and two topologies have been obtained in the three examples of tritopic-linker based Zr MCPs: MOF-808, *spn*;¹³ PCN-777, *spn*¹⁴ and UMCM-309, *kgd*¹⁵. Instead of a 12-connected cluster, all tritopic based Zr MCPs possess a 6-connected cluster. In other words, differences in topologies between ditopic- and tritopic-based Zr MCPs arise not only from changes in the linker geometry, but also result from the flexibility of cluster connectivity. Among reported Zr MCPs, the Zr_6 cluster ($Zr_6O_4(OH)_4(OOCR)_x$) shows multiple connectivities, commonly as 12 or 8 connected clusters, and in rare cases can be 6 or 10 connected. Therefore, cluster flexibility makes topology prediction more challenging for Zr MCPs than for those based on clusters with well-defined connectivity.

Topology diversity induced from linker complexity and cluster flexibility poses challenge in designing and targeting Zr-MCP topologies.¹⁶ A suitable case to demonstrate this is Zr MCPs constructed with tetratopic linkers. It is observed that Zr MCPs based on tetratopic linkers show an extraordinary diversity in topology due both to linker and cluster complexity. For example, the Zhou group has obtained Zr MCPs with the same porphyrin-based linker in 4 different topologies (PCN-222,¹⁷ PCN-223,¹⁸ PCN-224¹⁹ and PCN-225²⁰), a phenomenon unprecedented in Zr MCPs based on ditopic linkers. A general strategy for designing tetratopic-linker based Zr-MCP and controlling their topology is thus lacking. Herein the problem of topology prediction of Zr MCPs based on tetratopic linkers is addressed with a design strategy using a geometric analysis approach with an emphasis on linker flexibility. When linkers are designed to target a specific

shape, MCP topologies can be achieved in a highly controlled manner. This strategy is then tested with two linkers designed and synthesized to aim at specific shapes. Their corresponding Zr MCPs are synthesized to verify predictions.

3.2 Results and Discussion

MCPs can be abstracted as topologies in which metal clusters are vertices and the linkers are the linkages among them. Different vertex connectivity and linkage geometry lead to diverse topologies. For example, the combination of the $Zn_4O(CO_2R)_6$ cluster with H_2BDC gives the *pcu* net¹ and with H_3BTB gives the *qom* net²³ among others²⁴. Because linker geometry plays an important role in directing MCP topology, it is a good practice to carefully analyze linker shape before embarking on MCP design. The analysis is straightforward for ditopic linkers: they are simply treated as lines. The analysis can be more complicated with tritopic linkers. BTC and BTB possess D_{3h} symmetry which can be described as an equilateral triangle. As shown in two MCPs based on the paddlewheel, HKUST-1(H_3BTC)² and MOF-14(H_3BTB),²⁵ lead to closely related topologies (*tbo* net and *pto* net). However, when the linker symmetry is reduced from D_{3h} to C_{2v} , the desymmetrized linker [1,1':3',1''-terphenyl]-4,4'',5'-tricarboxylic acid (H_3TPTC) in UCMC-151²⁶ gives a different topology (*fmj* net). The desymmetrization is accompanied by a linker shape change, thus an equilateral triangle is not adequate to describe the linker geometry (Figure 3.1). For tetratopic linkers additional complexities arise. The highest symmetry cases yield a tetrahedral shape or a planar square shape. The tetrahedral shape ideally possesses T_d symmetry which is the highest symmetry that can be achieved by any tetratopic linker. It is realized synthetically with tetrahedral carbon²⁷ or silicon centers²⁸. On the other hand, the planar square shape has an ideal D_{4h} symmetry and is found in the important class of porphyrin-based linkers. However, some tetratopic linkers, such as those based on benzene central rings do not possess idealized D_{4h} symmetry; in such cases the 4-fold rotational symmetry is lost and a measurement of two sides of linkers shows an aspect ratio²⁹ larger than 1. The linker symmetry is reduced to

D_{2h} and therefore a planar square model is not adequate to describe this geometry (Figure 3.2) and a description of “planar rectangular” shape is preferred for this class of linkers. It should be noted that the linker shape is best reflected in the MCP structure. Whenever a crystal structure is available, the aspect ratio should be measured based on the distance between centroids of metal cluster as this is the most accurate way to describe the geometry of the linker. However, from a practical standpoint, no crystal structure will be available when designing a new MCP. Therefore, a measurement based solely on the linkers (distance between carbon atoms of carboxylate groups) is used as a surrogate tool to assess the aspect ratio of the designed linker. Attempts have been made to calculate centroids-based aspect ratio from linker-based aspect ratio plus known carboxylate group to Zr_6 cluster centroid distance. However, severe bending between the carboxylate group and the Zr_6 cluster are found in certain MCPs (for example, PCN-222). No angles based solely on the linker can be correlated to this bending and thus the attempts failed. From a practical standpoint, even a slight deviation from a linker aspect ratio of 1 suggests that rectangular shape will arise in the framework (demonstrated in Figure 3.3 using PCN-222 and NU-1000 as examples).

A search of carboxylate based tetratopic linkers in the Cambridge Structural Database (CSD)³⁰ also confirms that most linkers found can be categorized based on above analysis. In other words, they all fall into three shape classes: tetrahedron, planar square, and planar rectangular. In the case of Zr-based MCP there are 3 examples of tetrahedral linkers, 9 planar square and 6 planar rectangular (Table 3.1). However, idealized geometry of the linker does not convey the complete picture because distortions of the idealized geometries are routinely observed.

It is common to find linkers bending or deforming in the crystal structures of MCPs and recently linker flexibility based on bending potentials has been invoked to explain structural instability;³¹ thus linker flexibility is also crucial in MCP design. Because flexible linkers might access more than one geometric shape, it is necessary to define all

accessible, in the sense of energetically reasonable, geometries for a designed linker. For example, Zr MCPs based on porphyrin tetratopic carboxylate linkers exhibit four different topologies; this topological flexibility resulting from one linker is rarely found in MCPs. Notably, of the linkers in those four different structures, only one possesses a square shape within the coordination network whereas the other three show a rectangular shape (Figure 3.4a). Another case is Zr MCPs based on tetrakis[4-(4-carboxyphenyl)phenyl]ethene (H₄ETTC), two different topologies were obtained with the same linker (PCN-94³² and PCN-128³³). In PCN-94, the linker shows a square shape whereas in PCN-128 the linker shows a rectangular geometry. These observations prompted us to create a systematic framework to describe possible situations that a tetratopic linker could access multiple geometries. Two possibilities are presented below. For flexible planar linkers, they might access both the square and rectangular shape through deformation. Another possibility is that a linker can access both planar shape and tetrahedral shapes. This could be achieved through rotatable C-C linkage between two aryl rings shown in the example of a linker 3,3',5,5'-tetrakis(4-carboxyphenyl)-1,1'-biphenyl. The rotation of the biphenyl rings makes both tetrahedral and planar shapes accessible (Figure 3.4b).

The connectivity of the cluster in MCP design is as important as linker geometry. The Zr₆ cluster has been frequently observed in Zr MCPs. The most routinely reported cluster is 12-connected [Zr₆(μ₃-O)₄(μ₃-OH)₄(COOR)₁₂] which is found in the UiO-66-type structure. 8-Connected [Zr₆(μ₃-O)₄(μ₃-OH)₄(OH)₄(H₂O)₄(COOR)₈] is also observed in some structures (Figure 3.5). The cluster can be viewed by eliminating four carboxylate linkages in one mirror plane of symmetry in the 12 connected cluster and replacing them with 4 -OH and -H₂O groups. While 10 and 6-connected clusters are also observed, they occur less frequently than the 12- and 8-connected ones. Therefore the predictive analysis herein will focus on the 12- and 8-connectivity for Zr₆.

With the above issues of cluster diversity and flexibility of linkers in mind, a

strategy is developed in designing and targeting potential topologies for Zr MCPs based on tetratopic linkers. The combination of the three shapes of linker and 2 connectivities of cluster generates finite topology possibilities in the reticular chemistry structure resource (RCSR)³⁴ that are compatible with all above linker and cluster geometric information. The flow chart in Figure 3.6 demonstrates this strategy and summarizes the findings with regard to network topology (Table 3.2). The inputs are linker geometry and cluster connectivity and five groups of outcomes are identified based on these parameters. Linker shape can be tetrahedral, square, or rectangular. Cluster connectivity can be 12 or 8 (with the exception of square linkers that have only been observed with 12 connectivity). For flexible linkers, all accessible shapes should be considered under the flow chart (*vide infra*). The strategy is confirmed with all the tetratopic linker based Zr MCPs in the literature. Their determined topologies fit well into this framework (see Table 3.1 for full list), although several combinations are not sufficiently represented and therefore additional examples were sought. To test the robustness of the prediction framework, tetrahedral and planar rectangular linkers were designed and their Zr-MCPs synthesized; the tetrahedral linker would provide another example of a Zr-MCP derived from this linker topology whereas the rectangular linker was designed to test the effect of extreme deviation from square geometry (i.e. aspect ratio $\gg 1$).

The tetrahedral linker was designed based on a biphenyl core (Figure 3.7a). Crystal structures of the linker in MCPs showed possible access to a tetrahedral shape and thus led to a prediction of the *ith* or *flu* net depending on cluster connectivity. Solvothermal reaction between $ZrCl_4$ and the linker using benzoic acid as modulator in DMF gave colorless octahedral crystals (UMCM-312). The material crystallizes in the space group *Fmmm*. The Zr_6 cluster is 8-connected $[Zr_6(\mu_3-O)_4(\mu_3-OH)_4(OH)_4(H_2O)_4(COOR)_8]$. The two aryl rings in the biphenyl core exhibit a distorted tetrahedral shape with a dihedral angle of 29.9° matching our predication of possible access to tetrahedral shape. Each linker connects to 4 Zr_6 clusters maintaining a (4,8)-connected network. The topology of

this structure was determined to be *flu* net, a result in accord with the prediction from the framework (Figure 3.7). UMCM-312 collapsed upon vacuum activation, a result that may be related to the high flexibility of the linker. It should be noted that it is possible to obtain higher porosity in UMCM-312 if a maximum of dihedral angle of 90 ° is achieved. Adding bulky group at the *ortho* position to lock the C-C linkage would increase the dihedral angle and rigidify the linker. However, this linker is specifically chosen in this study to demonstrate that by rational design of linkers, targeted shape can even be achieved even with rotatable bonds in a linker that allows adopting more than one symmetry.

A planar rectangular linker based on a perylene core (Figure 3.8a) was chosen for the largest aspect ratio among tetratopic linkers in the literature. Reaction with $ZrCl_4$ in the presence of benzoic acid in DMF resulted in red needle-shaped crystals (UMCM-313). The structure crystallizes in the space group *P6/mmm* with an 8-connected Zr_6 cluster: $Zr_6(\mu_3-O)_4(\mu_3-OH)_4(OH)_4(H_2O)_4(COOR)_8$. Topology analysis determined the structure to be the *csq* net matching our prediction with the linker unambiguously assigned as rectangular (Figure 3.8). The aspect ratio measured from the crystal structure is determined to be the largest among reported tetratopic-linker based Zr MCPs. After activation at 120 °C under vacuum, UMCM-313 shows permanent porosity and a BET surface area of 2578 m²/g. Two different 1-D channel sizes is a prominent feature commonly observed in MCPs with *csq* topology. This is also found true in UMCM-313. Thus by rational design, the 1-D channel can be deliberately achieved.

Accessible linker geometry needs to be ascertained before topology prediction. However a practical tool is lacking for determining possible shapes. For example, it is unclear why porphyrin-based linkers can access both planar square (energetically favored) and planar rectangular (higher energy) forms whereas the perylene-core based linker only accesses a planar rectangular form. It is hypothesized that the energy required for the porphyrin-based linker distortion into the less favored form is much smaller than for the

perylene-core based structure. To test the hypothesis, energy calculations are carried out with each linker restricted to specific aspect ratios and then subjected to constrained DFT geometry optimization. All aspect ratios from computational results and the literature in Figure 3.9 are measured as the distance between carbon atoms of carboxylate groups. The energy of porphyrin-based linker between planar square (PCN-224, aspect ratio = 1) and planar rectangular shape (PCN-222, aspect ratio = 1.057; PCN-223, aspect ratio = 1.101; PCN-225, aspect ratio = 1.146. See Figure S3 for details on the calculation of aspect ratio) shows a difference less than 8 kJ/mol. On the contrary, the designed planar rectangular linker, based on a perylene core, when distorted to an aspect ratio 1 shows an energy increase of 35 kJ/mol. The huge energy difference explains why porphyrin-based linker can achieve the less energy-favored shape whereas the perylene-core based linker fails to do so.

3.3 Conclusions

In conclusion, a prediction framework is set up for tetratopic linker based MCPs utilizing analysis of linker geometry and cluster connectivity. Two linkers with tetrahedron and planar rectangular shapes are designed to test this framework. The structures of the resulting MCPs (UMCM-312 and UMCM-313) give the predicted topologies. Energy calculations considering only the distortion energy of the linkers prove to be a practical tool in defining accessible geometries.

3.4 Experimental Methods

General Information. Zirconium tetrachloride (Acros, 98%), benzoic acid (Acros, 99.5%) and dimethylformamide (DMF, Fisher Scientific, ACS reagent grade) were used as-received without further purification.

Synthesis of UMCM-312. Linker 3,3',5,5'-tetrakis(4-carboxyphenyl)-1,1'-biphenyl is synthesized according to published procedures.²¹ ZrCl₄ (11.6 mg, 0.0497 mmol) and benzoic acid (183 mg, 1.50 mmol) in 0.5 mL of DMF were dissolved in a 4 mL vial aided

by ultrasound. The vial was incubated in an 85 °C oven for 12 h. After cooling to room temperature, the mixture was filtered through a 0.45 µm polytetrafluoroethylene (PTFE) filter. Linker 3,3',5,5'-tetrakis(4-carboxyphenyl)-1,1'-biphenyl (6.80 mg, 0.0107 mmol) was added to the filtrate and dissolved by brief sonication. The clear colorless solution was kept at a 120 °C oven for 1 day. Colorless octahedral crystals were obtained (9.65 mg, 69.5 % yield). $Zr_6(\mu_3-O)_4(\mu_3-OH)_4(\text{benzoate})_4(C_{40}H_{22}O_8)_2$. Anal. Calcd (Found) for formula: C, 53.5 (52.7), H, 2.83 (2.89).

Synthesis of UMCM-313. Linker 2,5,8,11-tetrakis(4-carboxyphenyl)perylene is synthesized according to published procedures.²² $ZrCl_4$ (7.00 mg, 0.0300 mmol) and benzoic acid (760 mg, 3.11 mmol) in 1 mL of DMF were dissolved in a 4 mL vial aided by ultrasound. The vial was incubated in an 85 °C oven for 12 h. After cooling to room temperature, the mixture was filtered through a 0.45 µm PTFE filter. Linker 2,5,8,11-tetrakis(4-carboxyphenyl)perylene (3.50 mg, 0.00478 mmol) in 1 mL DMF was added to the filtrate and dissolved by brief sonication. The clear orange solution was kept at a 120 °C oven for 2 days. Orange needle crystals were obtained (4.43 mg, 81.8 % yield). $Zr_6(\mu_3-O)_4(\mu_3-OH)_4(OH)_4(H_2O)_4(C_{48}H_{24}O_8)_2$. Anal. Calcd (Found) for formula: C, 50.6 (50.4), H, 2.83(2.52).

X-ray Crystallography. Single-crystal X-ray data of UMCM-312 and UMCM-313 were collected on a Rigaku AFC10K Saturn 944+ CCD-based X-ray diffractometer equipped with a low temperature device and Micromax-007HF Cu-target micro-focus rotating anode ($\lambda = 1.54187$ Å) at 85(1) K. Rigaku d*trek images were exported to CrysAlisPro for processing and corrected for absorption. The structure was solved and refined with the Bruker SHELXTL (version 2014/6) software package. All non-hydrogen atoms were refined anisotropically with the hydrogen atoms placed in idealized positions. The SQUEEZE subroutine of the PLATON program suite was used to address the disordered solvent in the large cavity present in the structure. Crystallographic data and structural refinements for UMCM-312 and UMCM-313 are summarized in Table 3.

Gas adsorption of UMCM-313. N₂ sorption experiments were carried out at 77K using an Autosorb-1C Quantachrome Instruments (Boynton Beach, Florida, USA). He (99.999%, used to determine void volume), N₂ (99.999% purity) purchased from Cryogenic Gasses and used as received. As synthesized UMCM-313 (~15 mg) was washed with clean DMF and then soaked in a mixture of 10 mL DMF and 1 mL concentrated HCl at 100 °C oven overnight. The crystals were then washed with DMF and soaked in acetone. The acetone was replaced three times each day for 2 days. The sample was evacuated at 120 °C under dynamic vacuum for 12 h prior to sorption analysis.

Density Functional Theory (DFT) computations. All computations were carried out with Spartan 09. Linker starting conformations were obtained from crystal structures in UMCM-312 and UMCM-313. The distance between carbon atoms of carboxylate groups were constrained on opposite sides of the linker (two identical distance constraints total). The distorted linker was then subjected to a DFT geometry optimization with this aspect ratio constraint and the relative energy and final aspect ratio was recorded. All optimization used B3LYP functions and the 6-31G* basis set.

3.5 Figures

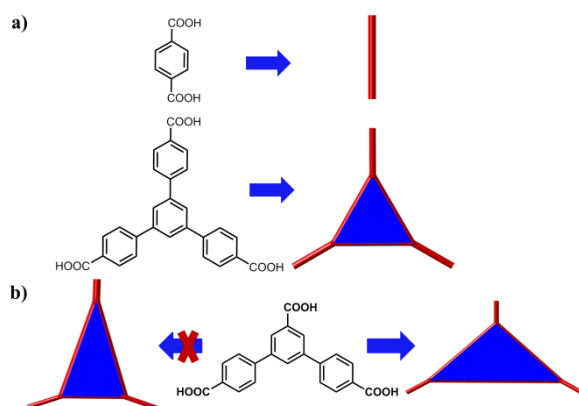


Figure 3.1. Topology representations of a) H₂BDC, H₃BTB and b) H₃TPTC.

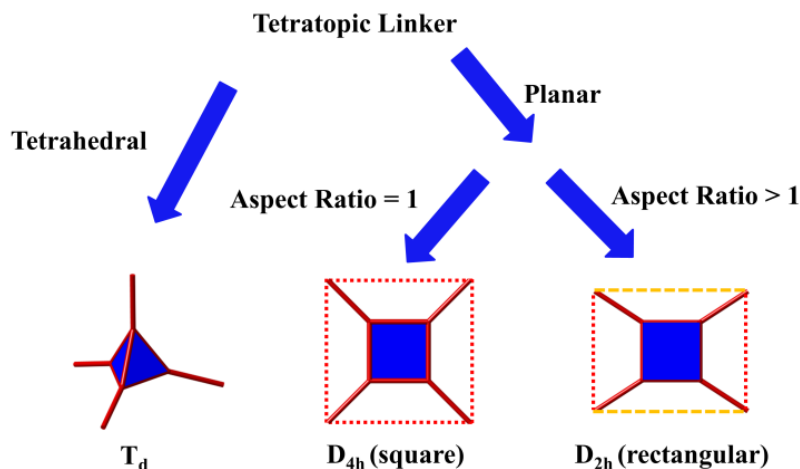


Figure 3.2. Classification of tetratopic linkers based on symmetry

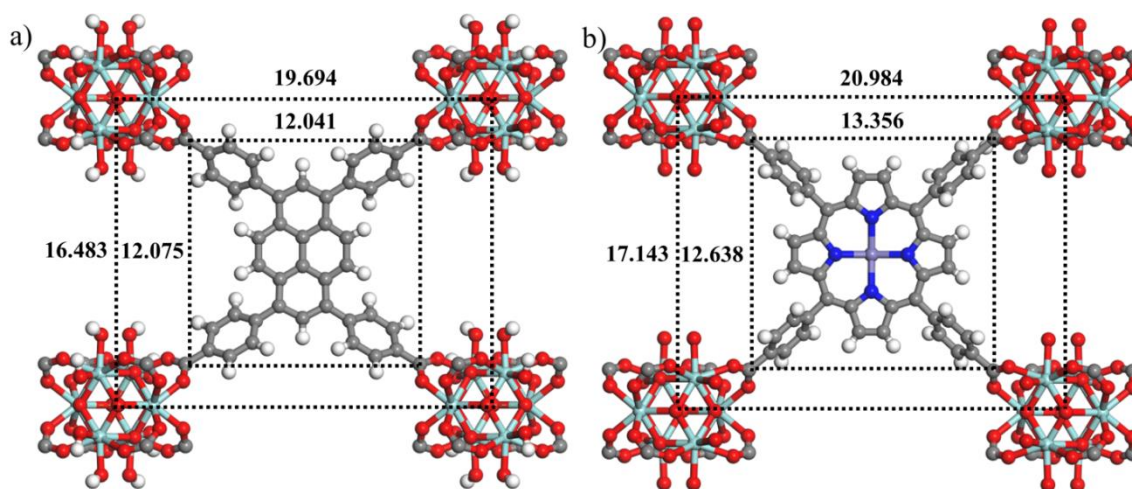


Figure 3.3 Two ways of measuring aspect ratio (distance between centroids in Zr₆ cluster versus distance between carbon atoms in carboxylate group in the unit of Å) exemplified in a) NU-1000 and b) PCN-222. NU-1000 shows an aspect ratio of 1.003 (by distance between carbon atoms in the carboxylate) or 1.19 (by distance between centroids in the cluster). PCN-222 shows an aspect ratio of 1.06 (by distance between carbon atoms in the carboxylate) or 1.22 (by distance between centroids in the cluster). In either case, both measurements indicate a rectangular geometry of the ligand. In practice, especially when designing new MCPs, aspect ratios measured by carbon atoms are good enough indicator for ligand geometry.

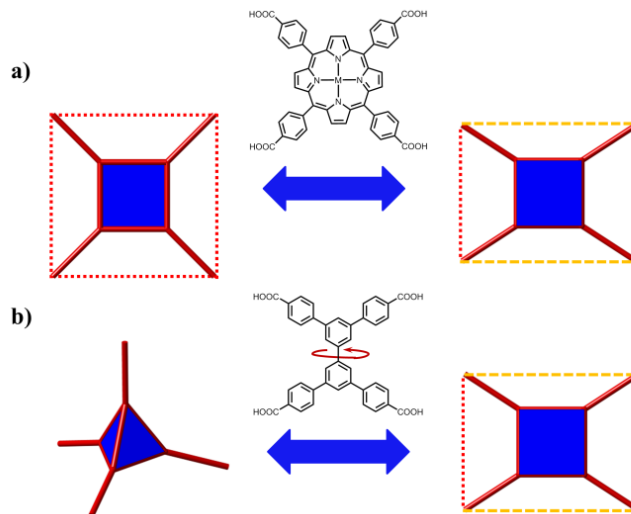


Figure 3.4 Mechanisms by which a flexible linker can access multiple geometries. a) A planar linker deforms to adopt both square and rectangular shapes. b) Adoption of both tetrahedral and planar shapes through bond rotation.

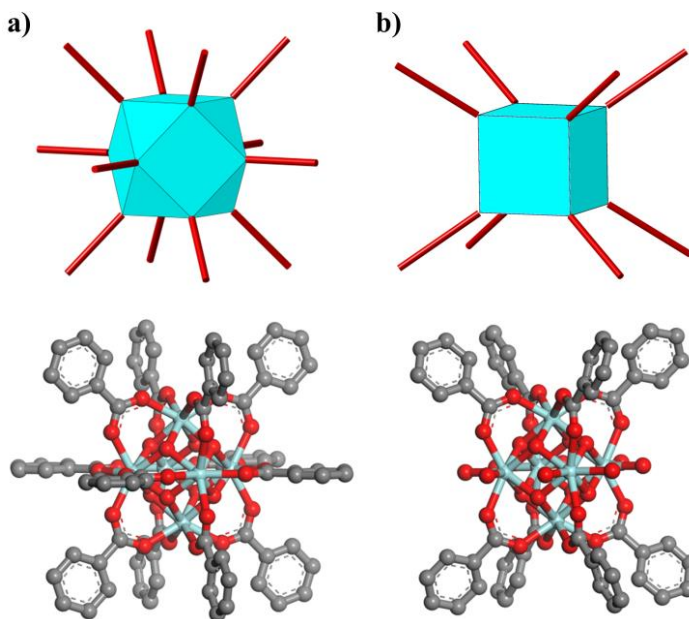


Figure 3.5. Common Zr₆ clusters and their topology representations of a) 12-connected $[\text{Zr}_6(\mu_3\text{-O})_4(\mu_3\text{-OH})_4(\text{COOR})_{12}]$ and b) 8-connected $[\text{Zr}_6(\mu_3\text{-O})_4(\mu_3\text{-OH})_4(\text{OH})_4(\text{H}_2\text{O})_4(\text{COOR})_8]$.

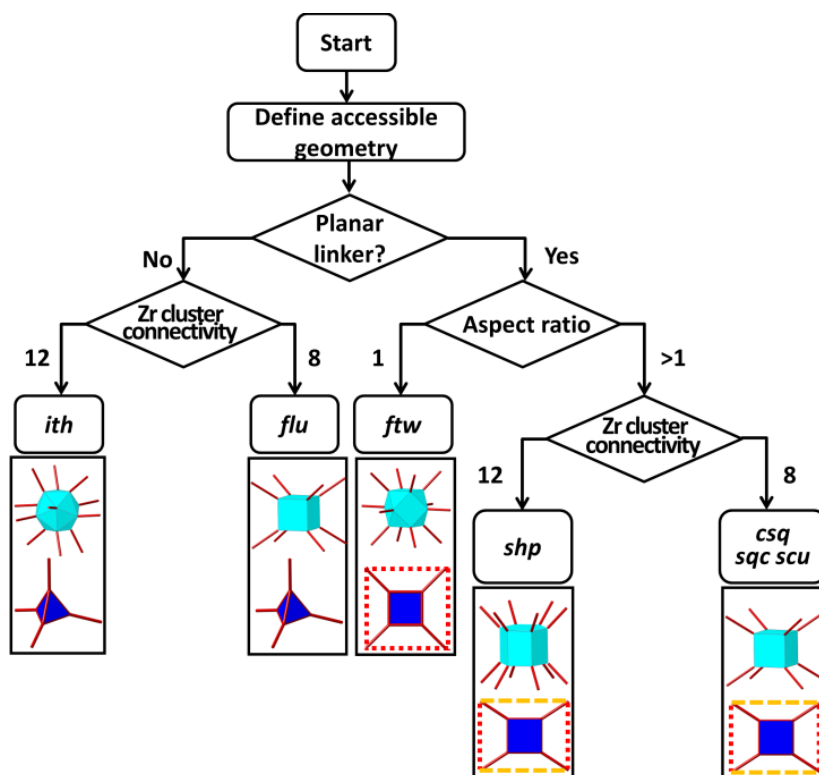


Figure 3.6. Topology prediction framework for designing tetratopic based Zr MCP.

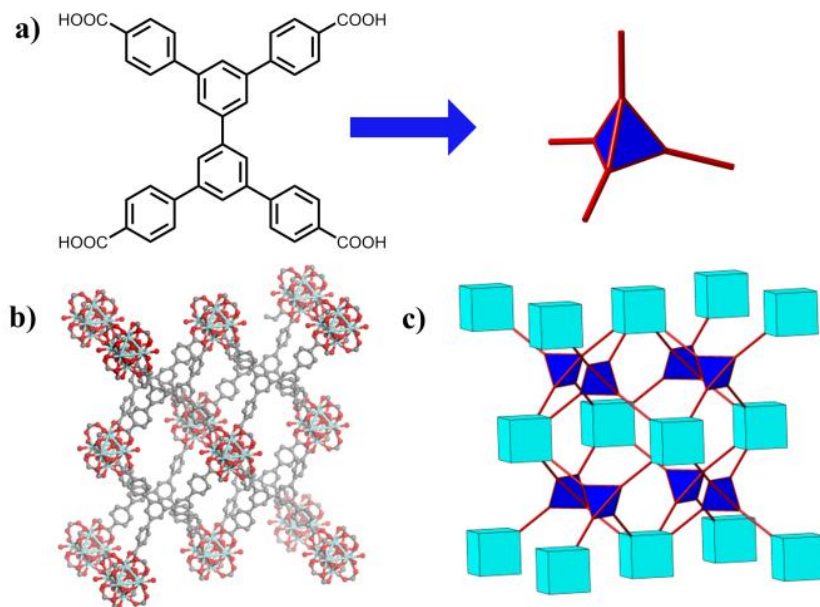


Figure 3.7. Structure of UCMC-312 a) Linker structure and its topology representation. b) Crystal structure of UCMC-312. c) Topology representation of *flu* topology.

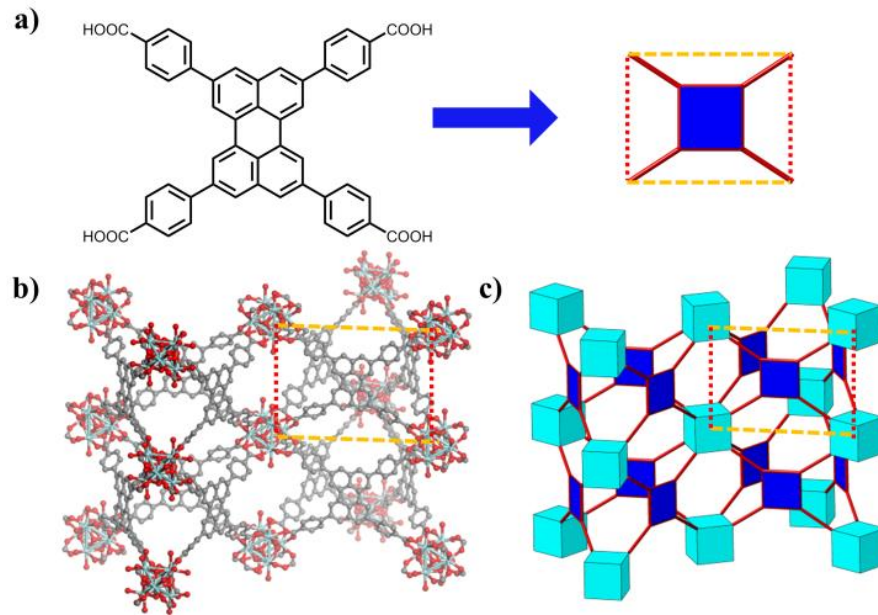


Figure 3.8. Structure of UMCM-313 a) Linker structure and its topology representation. b) Crystal structure of UMCM-313. c) Topology representation of *csq* topology.

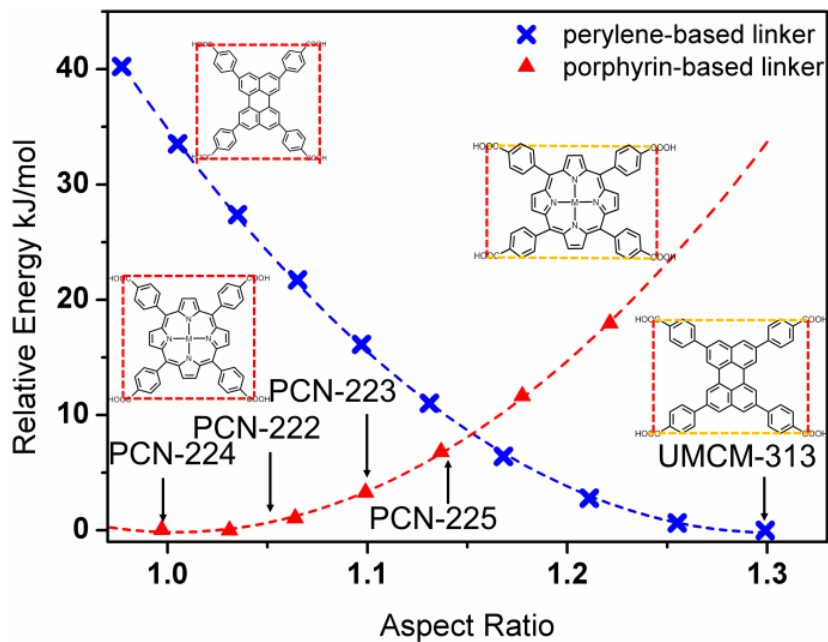
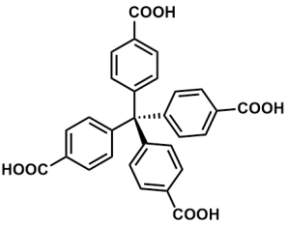
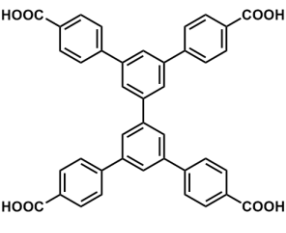
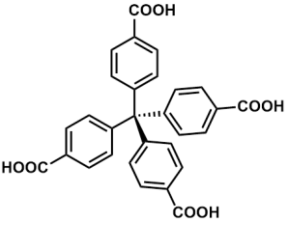
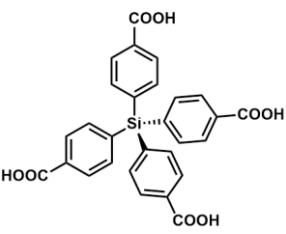
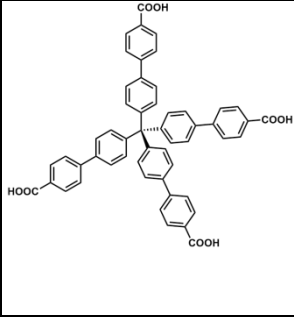
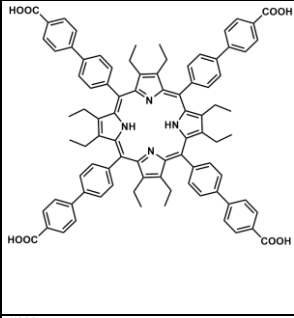
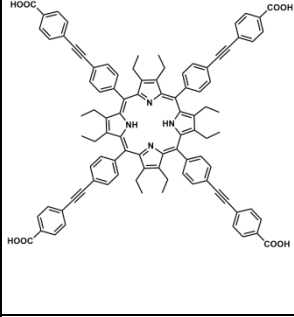
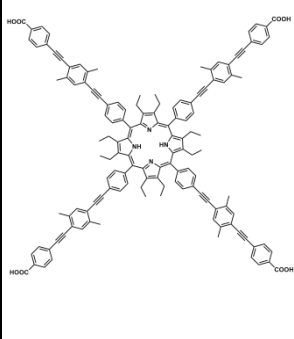
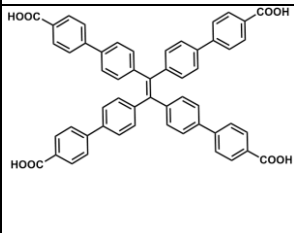
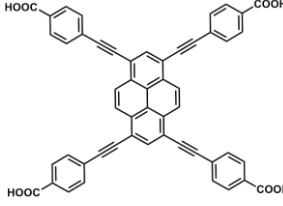
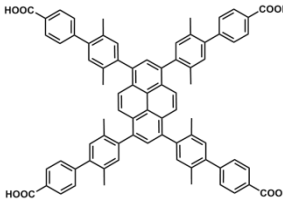
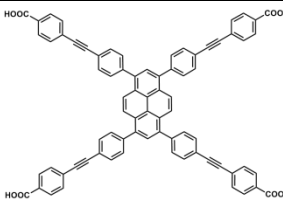
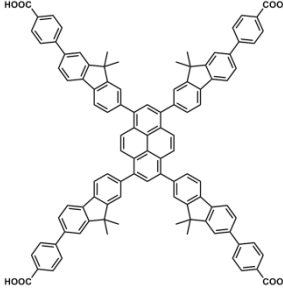
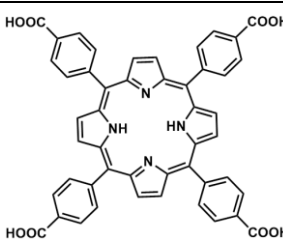


Figure 3.9. Relative energy of perylene-based and porphyrin-based linkers at different aspect ratios (aspect ratios observed in MCP crystal structures are marked with arrows).

3.6 Tables

Linker	Linker shape	Cluster connectivity	Predicted Topology	Experimental determined Topology	MOF
	Tetrahedron	12	<i>ith</i>	<i>ith</i>	MOF-812
	Tetrahedron	8	<i>flu</i>	<i>flu</i>	This work
	Tetrahedron	8	<i>flu</i>	<i>flu</i>	MOF-841
	Tetrahedron	8	<i>flu</i>	<i>flu</i>	Dalton 2015

	Tetrahedron	8	<i>flu</i>	<i>flu</i>	PCN-521
	Square	12	<i>ftw</i>	<i>ftw</i>	PCN-228 NU-1102
	Square	12	<i>ftw</i>	<i>ftw</i>	PCN-229 NU-1104
	Square	12	<i>ftw</i>	<i>ftw</i>	PCN-230
	Square	12	<i>ftw</i>	<i>ftw</i>	PCN-94

	Square	12	<i>ftw</i>	<i>ftw</i>	NU-1100
	Square	12	<i>ftw</i>	<i>ftw</i>	NU-1101
	Square	12	<i>ftw</i>	<i>ftw</i>	NU-1103
	Square	12	<i>ftw</i>	<i>ftw</i>	NU-1105
	Rectangular	12	<i>shp</i>	<i>shp</i>	PCN-223

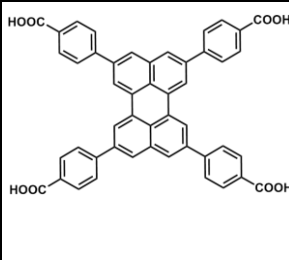
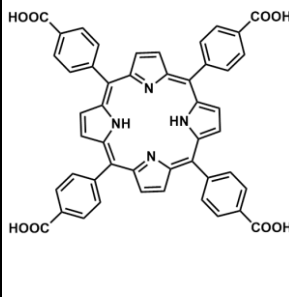
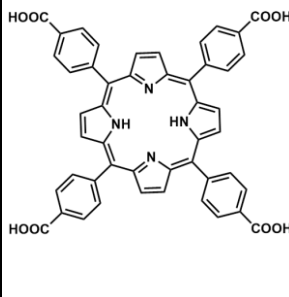
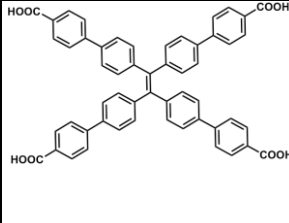
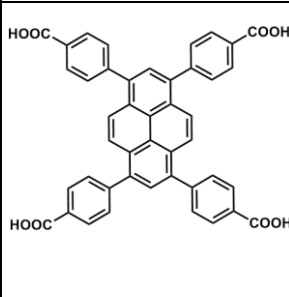
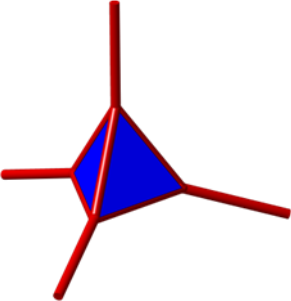
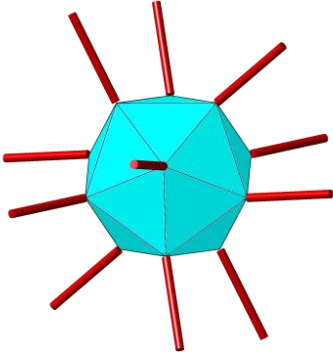
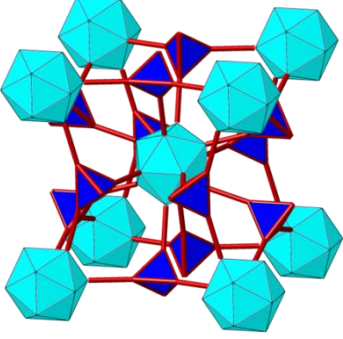
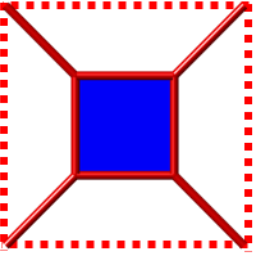
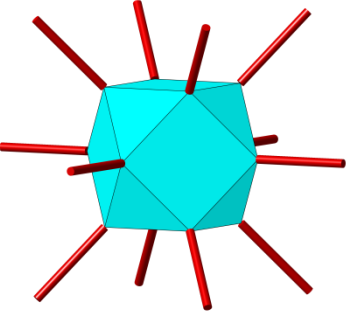
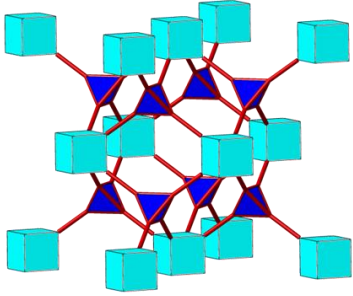
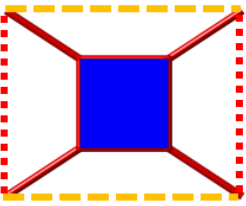
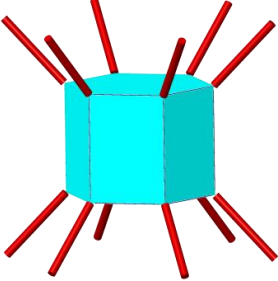
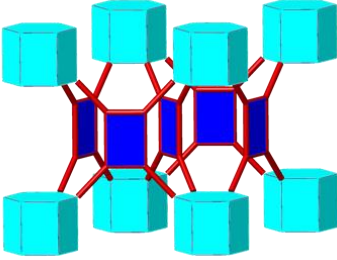
	Rectangular	8	<i>csq, scu or sqc</i>	<i>csq</i>	This work
	Rectangular	8	<i>csq, scu or sqc</i>	<i>csq</i>	PCN-222
	Rectangular	8	<i>csq, scu or sqc</i>	<i>sqc</i>	PCN-225
	Rectangular	8	<i>csq, scu or sqc</i>	<i>csq</i>	PCN-128
	Rectangular	8	<i>csq, scu or sqc</i>	<i>csq</i>	NU-1000

Table 3.1. Summary of linker shape, cluster connectivity, predicted topology based on prediction framework from this work and experimental determined topology from reported Zr MCPs based on tetratopic linker

Linker shape	Cluster connectivity	Predicted topology
<p data-bbox="310 499 461 531">Tetrahedral</p> 		<p data-bbox="1159 281 1203 312"><i>ith</i></p> 
<p data-bbox="298 1157 472 1188">Planar square</p> 		<p data-bbox="1159 1146 1203 1178"><i>flu</i></p> 
<p data-bbox="266 1545 505 1577">Planar rectangular</p> 		<p data-bbox="1159 1545 1203 1577"><i>shp</i></p> 

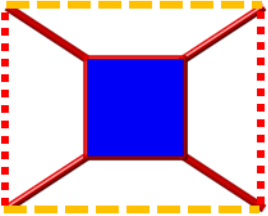
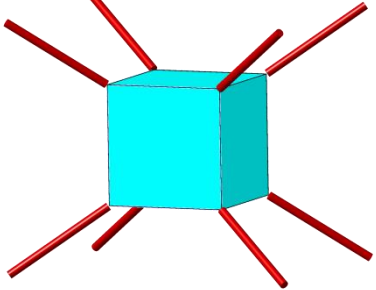
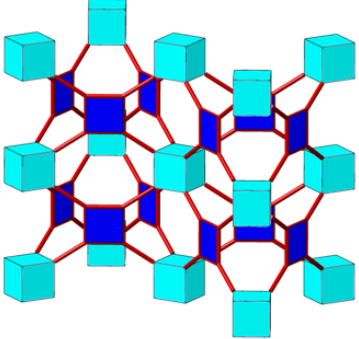
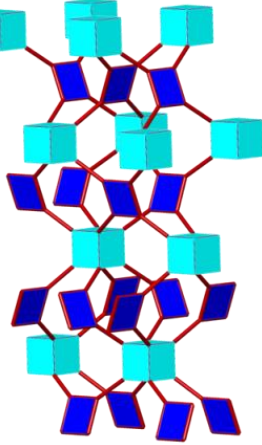
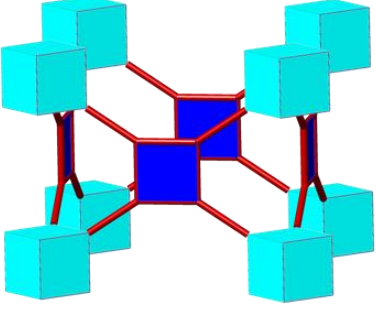
<p>Planar rectangular</p> 		<p><i>csq</i></p> 
		<p><i>sqc</i></p> 
		<p><i>scu</i></p> 

Table 3.2. Summary of linker shape, cluster connectivity and predicted topology mentioned in Figure 3.6 (prediction framework)

	UMCM-312	UMCM-313
Empirical formula	C ₄₀ H ₂₉ O ₁₆ Zr ₃	C ₄₈ H ₃₂ O ₁₆ Zr ₃
Formula weight	1039.29	1138.39
T (K)	85(2)	85(2)
Crystal size (mm)	0.08 x 0.06 x 0.02	0.08 x 0.04 x 0.04
Crystal system	Orthorhombic,	Hexagonal
space group	<i>Fmmm</i>	<i>P6/mmm</i>
a, b, c (Å)	16.2326(5), 33.0024(4), 35.7503(3)	45.4548(6), 45.4548(6), 15.5951(2)
α, β, γ (°)	90	90,90,120
Volume (Å ³)	19151.9(7)	27904.8(8)
Z	8	6
d _{calc} (g/cm ³)	0.721	0.406
μ (mm ⁻¹)	2.898	1.507
F(000)	4136	3408
Theta range for data collection	2.472 to 69.613	2.245 to 67.684
Limiting indices	-19<=h<=19, -39<=k<=38, -43<=l<=43	-54<=h<=56, -56<=k<=56, -18<=l<=19
Reflections collected / unique	74817 / 4827	650790 / 10335
R _{int}	0.0986	0.2424
Completeness	100.0 %	100.0 %
Absorption correction	Semi-empirical from equivalents	Semi-empirical from equivalents
Max. and min. transmission	1.00000 and 0.89469	1.00000 and 0.57005

Refinement method	Full-matrix least-squares on F ²	Full-matrix least-squares on F ²
Data / restraints / parameters	4827 / 151 / 147	10335 / 2 / 170
GOF on F ²	1.167	1.041
R ₁ , wR ₂ [I>2σ(I)]	0.0540, 0.1907	0.0806, 0.2190
R ₁ , wR ₂ (all data)	0.0602, 0.2016	0.1065, 0.2569
Δρ _{max} /Δρ _{min} (e · Å ⁻³)	0.770 and -0.892	2.025 and -1.642

Table 3.3. Crystal Data and Structure Refinements for UMCM-312 and UMCM-313.

3.7 References

- (1) Li, H.; Eddaoudi, M.; O'Keeffe, M.; Yaghi, O. M. *Nature* **1999**, *402*, 276.
- (2) Chui, S. S.-Y.; Lo, S. M.-F.; Charmant, J. P. H.; Orpen, A. G.; Williams, I. D. *Science* **1999**, *283*, 1148.
- (3) Suh, M. P.; Park, H. J.; Prasad, T. K.; Lim, D.-W. *Chem. Rev.* **2012**, *112*, 782.
- (4) He, Y.; Zhou, W.; Qian, G.; Chen, B. *Chem. Soc. Rev.* **2014**, *43*, 5657.
- (5) Van de Voorde, B.; Bueken, B.; Denayer, J.; De Vos, D. *Chem. Soc. Rev.* **2014**, *43*, 5766.
- (6) Chughtai, A. H.; Ahmad, N.; Younus, H. A.; Laypkov, A.; Verpoort, F. *Chem. Soc. Rev.* **2015**, *44*, 6804.
- (7) Horcajada, P.; Gref, R.; Baati, T.; Allan, P. K.; Maurin, G.; Couvreur, P.; Férey, G.; Morris, R. E.; Serre, C. *Chem. Rev.* **2012**, *112*, 1232.
- (8) Kreno, L. E.; Leong, K.; Farha, O. K.; Allendorf, M.; Van Duyne, R. P.; Hupp, J. T. *Chem. Rev.* **2012**, *112*, 1105.
- (9) Yaghi, O. M.; O'Keeffe, M.; Ockwig, N. W.; Chae, H. K.; Eddaoudi, M.; Kim, J. *Nature* **2003**, *423*, 705.
- (10) Luebke, R.; Belmabkhout, Y.; Weselinski, Ł. J.; Cairns, A. J.; Alkordi, M.; Norton, G.; Wojtas, Ł.; Adil, K.; Eddaoudi, M. *Chem. Sci.* **2015**, *6*, 4095.
- (11) Cavka, J. H.; Jakobsen, S.; Olsbye, U.; Guillou, N.; Lamberti, C.; Bordiga, S.; Lillerud, K. P. *J. Am. Chem. Soc.* **2008**, *130*, 13850.
- (12) Schaate, A.; Roy, P.; Godt, A.; Lippke, J.; Waltz, F.; Wiebcke, M.; Behrens, P. *Chem. Eur. J.* **2011**, *17*, 6643.
- (13) Furukawa, H.; Gándara, F.; Zhang, Y.-B.; Jiang, J.; Queen, W. L.; Hudson, M. R.; Yaghi, O. M. *J. Am. Chem. Soc.* **2014**, *136*, 4369.
- (14) Feng, D.; Wang, K.; Su, J.; Liu, T.-F.; Park, J.; Wei, Z.; Bosch, M.; Yakovenko, A.; Zou, X.; Zhou, H.-C. *Angew. Chem. Int. Ed.* **2015**, *54*, 149.
- (15) Ma, J.; Wong-Foy, A. G.; Matzger, A. J. *Inorg. Chem.* **2015**, *54*, 4591.

- (16) Gomez-Gualdrón, D. A.; Gutov, O. V.; Krungleviciute, V.; Borah, B.; Mondloch, J. E.; Hupp, J. T.; Yildirim, T.; Farha, O. K.; Snurr, R. Q. *Chem. Mater.* **2014**, *26*, 5632.
- (17) Feng, D.; Gu, Z.-Y.; Li, J.-R.; Jiang, H.-L.; Wei, Z.; Zhou, H.-C. *Angew. Chem. Int. Ed.* **2012**, *51*, 10307.
- (18) Feng, D.; Gu, Z.-Y.; Chen, Y.-P.; Park, J.; Wei, Z.; Sun, Y.; Bosch, M.; Yuan, S.; Zhou, H.-C. *J. Am. Chem. Soc.* **2014**, *136*, 17714.
- (19) Feng, D.; Chung, W.-C.; Wei, Z.; Gu, Z.-Y.; Jiang, H.-L.; Chen, Y.-P.; Darensbourg, D. J.; Zhou, H.-C. *J. Am. Chem. Soc.* **2013**, *135*, 17105.
- (20) Jiang, H.-L.; Feng, D.; Wang, K.; Gu, Z.-Y.; Wei, Z.; Chen, Y.-P.; Zhou, H.-C. *J. Am. Chem. Soc.* **2013**, *135*, 13934.
- (21) Yang, S.; Lin, X.; Lewis, W.; Suyetin, M.; Bichoutskaia, E.; Parker, J. E.; Tang, C. C.; Allan, D. R.; Rizkallah, P. J.; Hubberstey, P.; Champness, N. R.; Mark Thomas, K.; Blake, A. J.; Schröder, M. *Nat Mater* **2012**, *11*, 710.
- (22) Tran, L. D.; Ma, J.; Wong-Foy, A. G.; Matzger, A. J. *Chem. Eur. J.* **2016**, *22*, 5509.
- (23) Chae, H. K.; Siberio-Pérez, D. Y.; Kim, J.; Go, Y.; Eddaoudi, M.; Matzger, A. J.; O'Keeffe, M.; Yaghi, O. M. *Nature* **2004**, *427*, 523.
- (24) Caskey, S. R.; Wong-Foy, A. G.; Matzger, A. J. *Inorg. Chem.* **2008**, *47*, 7751.
- (25) Chen, B.; Eddaoudi, M.; Hyde, S. T.; O'Keeffe, M.; Yaghi, O. M. *Science* **2001**, *291*, 1021.
- (26) Schnobrich, J. K.; Lebel, O.; Cychosz, K. A.; Dailly, A.; Wong-Foy, A. G.; Matzger, A. J. *J. Am. Chem. Soc.* **2010**, *132*, 13941.
- (27) Zhang, M.; Chen, Y.-P.; Bosch, M.; Gentle, T.; Wang, K.; Feng, D.; Wang, Z. U.; Zhou, H.-C. *Angew. Chem. Int. Ed.* **2014**, *53*, 815.
- (28) Wang, S.; Wang, J.; Cheng, W.; Yang, X.; Zhang, Z.; Xu, Y.; Liu, H.; Wu, Y.; Fang, M. *Dalton Trans.* **2015**, *44*, 8049.
- (29) The shape of the linker is defined by vertices set at centroids of Zr₆ cluster. Distances between vertices were determined to give both sides lengths. The aspect ratio of a linker is defined as the longer side divided by the shorter one.
- (30) Allen, F. *Acta Crystallogr. Sect. B: Struct. Sci.* **2002**, *58*, 380.
- (31) Dutta, A.; Wong-Foy, A. G.; Matzger, A. J. *Chem. Sci.* **2014**, *5*, 3729.
- (32) Wei, Z.; Gu, Z.-Y.; Arvapally, R. K.; Chen, Y.-P.; McDougald, R. N.; Ivy, J. F.; Yakovenko, A. A.; Feng, D.; Omary, M. A.; Zhou, H.-C. *J. Am. Chem. Soc.* **2014**, *136*, 8269.
- (33) Zhang, Q.; Su, J.; Feng, D.; Wei, Z.; Zou, X.; Zhou, H.-C. *J. Am. Chem. Soc.* **2015**, *137*, 10064.
- (34) O'Keeffe, M.; Peskov, M. A.; Ramsden, S. J.; Yaghi, O. M. *Acc. Chem. Res.* **2008**, *41*, 1782.

Chapter 4: Rapid Guest Exchange and Ultra-low Surface Tension Solvents Optimize Metal-Organic Framework Activation[†]

4.1 Introduction

Porous materials, including carbons, zeolites, and certain coordination polymers, often require regimens of chemical, thermal, and/or pressure treatment to achieve their highest levels of surface area.¹⁻³ Such processes are collectively termed ‘activation’ and the details of these processes are particularly important for metal-organic frameworks (MOFs);⁴ nonporous materials are often obtained if, after synthesis, the solvent (guest) is not removed properly.⁵ Synthesis of MOFs is typically carried out solvothermally in high boiling point formamide solvents such as N,N-dimethylformamide (DMF), N,N-diethylformamide (DEF), N-methyl-2-pyrrolidone (NMP) or in dimethylsulfoxide (DMSO) and rarely can the high inherent porosity of the material be accessed by direct evacuation to remove these solvents. Despite progress in developing new strategies for guest removal,⁶⁻¹⁰ it is frequently reported that after activation, MOFs show broadened powder X-ray diffraction (PXRD) patterns (compared to solvent filled ones) and lower surface areas and pore volumes compared to those calculated from single crystal X-ray structures.¹¹⁻¹³ Furthermore, considerable variations in surface area and gas storage properties pervade the literature even for well-established MOFs.¹⁴ When such discrepancies are encountered they are often ascribed to ‘incomplete activation’ and attributed to capillary forces leading to partial or full structural collapse.¹⁵ To address

[†] Published: Ma, J.; Kalenak, A. P.; Wong-Foy, A. G.; Matzger, A. J. *Angew. Chem. Int. Ed.* **2017**, *56*, 14618.

such discrepancies, it is necessary to understand the nature of activation; insights into this process and best practices for MOF activation form the content of this communication.

Current activation strategies are largely empirical in nature and rely on two steps to remove guest molecules: guest exchange and guest evacuation (Figure 4.1).¹⁶⁻¹⁷ The approach, first established to reveal the permanent porosity in MOF-5,⁹ involves submerging MOFs into low boiling point solvents such as CH_2Cl_2 , CHCl_3 and CH_3OH (guest exchange) for days, replacing the solvent multiple times each day before vacuum evacuation (guest evacuation). If this conventional activation method fails to generate theoretical surface areas, another milestone discovery - supercritical CO_2 (scCO_2) processing - has been demonstrated to be extremely useful in unveiling a MOF's true porosity, especially highly porous Zn-based MOFs.^{9,19} Though the protocols have been widely performed and work successfully for many MOFs, how key factors such as solvent exchange time and the number of solvent washes influence outcome are unknown. With regard to the evacuation step, the type of solvent and the rate of guest evacuation also require further exploration to understand their roles in the activation process. Understanding these factors is critical, especially when empirical protocols fail to activate challenging MOFs and further tuning of these factors is necessary to achieve the highest surface area. Moreover, as the desire to transition more MOFs to industrial scale mounts, efficiency in activation protocol will have a pivotal effect on the economics of production.²⁰

4.2 Results and Discussion

Solvent exchange in Zn_4O based MOFs²¹ is generally conducted on timescales ranging from hours to days in various established solvent exchange procedures, a suggestion of a slow kinetic process. However, slow exchange is not consistent with our observations on solvent exchange of, for example, UMCM-9 ($\text{Zn}_4\text{O}(\text{naphthalene-2,6-dicarboxylate})_{1.5}(\text{biphenyl-4,4'-dicarboxylate})_{1.5}$), a highly porous mixed-linker Zn_4O based MOF.²² During our experiments in exchanging solvent from

DMF to CH₂Cl₂ for UMCM-9, as synthesized crystals were found to float upon addition of CH₂Cl₂. Almost immediately, the crystals begin to sink back to the bottom on the timescale of seconds and with a rate that is slower for larger crystals (Figure 4.2a and video upon request). Such behavior indicates a fast guest exchange process wherein DMF (density=0.94 g/cm³) molecules are replaced by CH₂Cl₂ (density=1.43 g/cm³) causing a dramatic density increase for the UMCM-9 crystals. To confirm the hypothesis of fast kinetics observed in solvent exchange, we focused on MOF-5 (Zn₄O(benzene-1,4-dicarboxylate)₃) because its limiting pore aperture (8 Å) is larger than most solvent molecules; in addition MOF-5 has been made in labs around the world using established procedures. To perform real-time monitoring of solvent exchange, ~50 mg of MOF-5 crystals (300-500 μm in diameter) soaked in DMF were collected by filtration and transferred into a 5 mm NMR tube. After introducing 600 μL of CH₂Cl₂ to the NMR tube to mimic the solvent exchange process, the solution was monitored using ¹H-NMR spectroscopy (no sample spinning) where a spectrum was taken every 30 s over a 20 minutes period (Figure 4.2b). The DMF signal (corresponding to DMF exiting the MOF and equilibrating with the exchange solvent) increases steadily in the first 5 min and after 10 minutes a plateau is reached (Figure 4.2c); monitoring for up to 3 hours reveals no further concentration change. A second solvent exchange was also performed where the previously exchanged CH₂Cl₂ was decanted before another 600 μL of fresh CH₂Cl₂ was replenished; this mimics the common practice of multiple washes in MOF solvent exchange protocols. The DMF signal increases steadily and after 20 minutes the change is insignificant (Figure 4.2d).

The fast kinetics of solvent exchange in MOF-5 is clear from the above experiments; however, if there are some more tightly held solvents the completeness of exchange may not be well reflected.²³ Thus MOF-5 was subjected to N₂ isotherm measurement and digestion after each solvent exchange to determine the influence of the exchange protocol on surface area. Approximately 40 mg of MOF-5 was exchanged with 10 mL CH₂Cl₂ for

1, 2 or 3 times (each exchange conducted for 20 minutes) before evacuation and N₂ isotherm measurement. The activated MOF-5 crystals were further digested under acidic conditions to determine the DMF content. The results are shown in the Table 4.1, Figure 4.3 and Figure 4.4. After only one exchange, the DMF concentration is reduced to 0.78 DMF molecules per unit cell in MOF-5 and exhibits a BET surface area of 2650 ± 20 m²/g. The DMF content is further reduced to 0.12 molecules per unit cell after two exchanges with a higher surface area of 3410 ± 30 m²/g. After three solvent exchanges, a surface area of 3640 ± 40 m²/g, matching the theoretical value (3527 m²/g), is obtained with only 0.014 DMF molecules detected per unit cell. Thus the completeness of exchange after multiple short timescale exchanges is confirmed. These observations are echoed by experiments with IRMOF-2, the brominated analog of MOF-5, a compound with slightly smaller pores and additional solvent interaction sites.²⁴ Though both of these factors would be expected to slow exchange kinetics, the effect is minor (Figure 4.5) and rapid exchange occurs.

Armed with an understanding of the timescale for solvent exchange, we turned our attention to guest evacuation in MOFs. If capillary forces caused by surface tension are indeed the major contributor to these failures,²⁵ structural collapse may be avoided by filling the pores with ultralow surface tension solvents via exchange before evacuation, providing a convenient alternative solution to scCO₂ for the activation of extremely fragile MOFs. To test this hypothesis, we attempted to activate UMCM-9 that has previously failed to be activated by the conventional solvent exchange method. UMCM-9 was reported to undergo partial collapse when evacuated from material completely exchanged in CH₂Cl₂ and a low surface area of 1330 m²/g. Only by activation with flowing scCO₂, was a surface area of 4970 m²/g achieved, matching the theoretical value of 4900 m²/g.²² The solvent n-hexane was chosen as the exchange medium due to its low surface tension (17.9 mN/m) compared to CH₂Cl₂ (27.2 mN/m). UMCM-9 was fully exchanged with n-hexane (through a two-step exchange procedure due to the

immiscibility of DMF and n-hexane, see experimental section for details) before evacuation and a high surface area of $4980 \pm 50 \text{ m}^2/\text{g}$ was obtained (Figure 4.6).²⁶ Furthermore, no structural changes after activation of UMCM-9 were found by PXRD analysis (Figure 4.7). It should be noted that exchange of all loosely bound solvent is possible by this procedure, but for MOFs with coordinatively unsaturated metal sites, heating under vacuum may be required for full activation.²⁷⁻²⁸ This is also true for MOFs activated by scCO_2 .⁷

Solvent evacuation rate is known to affect porosity in some classes of materials.²⁹ However, as commonly practiced in MOF activation, the solvent evacuation rate is uncontrolled and the impact of this parameter on MOF activation is unknown. To investigate this activation variable, controlled evacuation of *n*-hexane from UMCM-9 was carried out at three rates: 380 torr/h, 9,990 torr/h and >225,000 torr/h. A two-step procedure was applied to evacuate ~40 mg of UMCM-9 wherein the pressure was reduced from atmospheric pressure (760 torr) to 1 torr at the specified rate and then maintained under dynamic vacuum (~0.05 torr) for another 2 hours before N_2 isotherm measurement. The activated materials all demonstrated full surface area indicating evacuation rate does not impact surface area (Figure 4.8).

When expanding the scope of the conventional solvent exchange activation method to more delicate MOFs, further tuning of solvent surface tension is needed to avoid structural collapse as demonstrated below in the activation of the fragile Zn paddle-wheel ($\text{Zn}_2(\text{CO}_2\text{R})_4$) based MOF, FJI-1.³⁰ FJI-1 was reported to amorphatize when evacuated from CH_2Cl_2 exchanged materials. Following the success in activation of UMCM-9, *n*-hexane was applied as the exchange medium in FJI-1 prior to evacuation. However, only negligible surface area ($<100 \text{ m}^2/\text{g}$) was observed (Figure 9). Nevertheless, *n*-hexane is already one of the lowest surface tension solvents commonly found in a lab setting. To achieve even lower surface tension at room temperature and atmospheric pressure, we turn to fluorocarbons. Perfluoropentane possesses a surface tension of 9.42 mN/m. When

FJI-1 is exchanged completely in perfluoropentane (see Experimental Methods for details) and then evacuated, the activated material shows a high BET surface area of 4890 ± 50 m^2/g , which matches well with the theoretical surface area ($4741 \text{ m}^2/\text{g}$) and the state of art scCO_2 flowing processing ($4813 \text{ m}^2/\text{g}$) (Figure 4.9).⁷ Powder X-ray diffraction analysis also confirmed the obtained phase matches with the crystal structure (Figure 4.10).

4.3 Conclusions

In this paper, we have shown that the solvent exchange process is rapid and that minutes rather than days are appropriate for solvent exchange in many MOFs. Lower surface tension solvents such as n-hexane and perfluoropentane are found to create much milder activation conditions during vacuum application and thus lead to better preserved MOF surface area and porosity. Finally we note that scCO_2 activation may not be required for the vast majority of MOFs. Practices such as shorter solvent exchange time and ultralow surface tension solvent should be regarded as the best practices in the field before claiming that conventional activation fails for a given material.

4.4 Experimental Methods

Reagents. Zinc nitrate hexahydrate (Fisher Scientific, ACS grade), 1,4-benzenedicarboxylic acid (H_2BDC , Fisher Scientific, 98%), 2,6-naphthalenedicarboxylic acid (H_2NDC , TCI America, 98%), 4,4'-biphenyldicarboxylic acid (H_2BPDC , Acros Organics, 98%), 2-bromoterephthalic acid ($\text{H}_2\text{BDC-Br}$, Acros Organics, 95%), zinc perchlorate hexahydrate (Alfa Aesar, Reagent grade), 1,3,5-tris(4-carboxyphenyl)benzene (H_3BTB , Alfa Aesar, 98%), 4,4'-bipyridine (Acros Organics, 98%), tetrafluoroboric acid solution (HBF_4 , Sigma-Aldrich, 48 wt% in H_2O), N-Methyl-2-pyrrolidone (NMP, Fisher Scientific, Laboratory grade), dichloromethane (Fisher scientific, HPLC grade), perfluoropentane (Strem Chemicals, >98%), and dimethylformamide (DMF, Fisher Scientific, >99.5%)

were used as received. Diethylformamide (DEF, TCI America, >99.0%) was purified by storing over activated charcoal for ~1 month and subsequently passing through a silica gel column. Anhydrous n-hexane (Fisher Scientific) was stored over activated 4 Å molecular sieves.

Powder X-ray diffraction. Powder X-ray diffraction (PXRD) data were collected on a Rigaku R-axis Spider diffractometer with an image plate detector and Cu-K α radiation (graphite monochromated, 1.5406 Å) operating at 40 kV and 44 mA in transmission mode. Images were collected with χ fixed at 45° while the ϕ was rotating at 10°/min and ω oscillating between 5° and 50° to minimize effects of preferred orientation. The 1-D diffractogram was obtained by integration of the resulting two-dimensional images using the AreaMax (2.0) software package with a step size of 0.1° in 2θ .

Solvent evacuation instrumentation. All MOFs were evacuated under dynamic vacuum for 2 hours using a duoseal vacuum pump (Welch, Model No. 1400B-1). The ultimate vacuum level reached was ~ 0.05 torr. Controlled evacuation experiments were carried out with specified evacuation rates using a needle valve coupled with a Digital Vacuum Regulator (J-KEM, Model No. DVR-200).

Gas sorption measurement. Nitrogen gas sorption experiments were carried out using a NOVA 4200 surface area analyzer from Quantachrome Instruments (Boynton Beach, Florida, USA). Ultra-high purity N₂ (99.999%) was purchased from Cryogenic Gases and used as received. Approximately 30-40 mg of samples in a sample cell soaked in desired exchange solvent were first evacuated under a dynamic vacuum (~0.05 torr) for 2 hours before transferring to the surface area analyzer. N₂ sorption experiments were carried out at 77K. The obtained isotherm was obtained and analyzed using the NOVAwin software. The relative pressure range for calculating the surface area satisfied the criteria for applying BET theory.³¹

¹H-NMR measurement. All ¹H-NMR measurements are carried out on Varian Inova 500 spectrometer operating at 500 MHz at room temperature.

Monitoring of solvent exchange in MOF-5 and IRMOF-2 by $^1\text{H-NMR}$. ~50 mg of MOF-5 or IRMOF-2 soaked in DMF were transferred to a 5 mm NMR tube. A 5 mm NMR tube with 600 μL of CH_2Cl_2 and ~50 mg MOF-5 was first loaded in the Varian Inova 500 spectrometer to pre-shim the magnet. Due to the short interval between each data point, the following acquisition parameters were chosen and applied to give relatively accurate integration and good signal to noise ratio for the kinetics data: steady state scan (ss) = -1, acquisition time (at) = 5 s, relaxation delay (dl) = 5 s, number of transient (nt) = 2. The total relaxation time is 10s which is ~2.5 T_1 of methyl proton in DMF at 2.55 ppm. Once the acquisition parameter is set and the pre-shimming of the magnet is completed, 600 μL of CH_2Cl_2 was introduced into the NMR tube with MOF-5 crystals and the sample was immediately loaded with acquisitions of spectra every 30s for 20 mins. The obtained raw spectra were phase corrected and baseline corrected before integration of the proton peak in the CH_2Cl_2 and DMF methyl peak ($(\text{CH}_3)_2\text{NC}(\text{O})\text{H}$) at 2.55 ppm in MestReNova 5.3.1. The DMF concentration was then calculated based on the amount of CH_2Cl_2 and the ratio between the integration area of DMF methyl peak and CH_2Cl_2 proton peak.

N_2 isotherm measurement and digestion of MOF-5 after multiple solvent exchanges. ~ 40 mg of MOF-5 were exchanged with 10 mL CH_2Cl_2 1, 2 or 3 times. Each time crystals were soaked in CH_2Cl_2 for 20 min before solvent decanted and replenished with fresh CH_2Cl_2 . After the desired number of solvent exchanges, MOF-5 crystals were evacuated under a dynamic vacuum (~ 0.05 torr) for 2 hours before N_2 isotherm measurements. After the N_2 measurement was done, MOF-5 crystals were digested in a mixture of 550 μL DMSO-d_6 (99.96 atm % D, Sigma Aldrich) and 50 μL DCl (35 wt% in D_2O , 99 atm % D, Sigma Aldrich). The samples were then subjected to $^1\text{H-NMR}$ spectroscopy to quantitatively determine DMF content per unit cell. Relaxation delay time was set to 25 s to ensure the complete relaxation of methyl proton in DMF.

Activation procedure for UMCM-9. UMCM-9 (~40 mg) initially washed with

DMF (3×20 mL) was first exchanged with CH_2Cl_2 . The crystals were soaked in 20 mL of CH_2Cl_2 3 times over 1 hour (20 minutes each). The crystals were then immersed in 20 mL of dry n-hexane over 1 hour replacing the solvent every 20 minutes. Once the solvent exchange is complete, the material was isolated by decanting the n-hexane and the crystals were evacuated under dynamic vacuum (0.05 torr) for 2 hours at room temperature before N_2 isotherm measurement.

Activation procedure for FJI-1. Because perfluoropentane is not miscible with most organic solvents, a multiple step exchange procedure is carried out below. FJI-1 (~40 mg) initially washed with DMF (3×20 mL) was first exchanged with CH_2Cl_2 . The crystals were soaked in 20 mL of CH_2Cl_2 3 times over 1 hour (20 minutes each). The crystals were then immersed in 20 mL of dry n-hexane over 1 hour replacing the solvent every 20 minutes. FJI-1 crystals were finally soaked in 20 mL of perfluoropentane 3 times over 1 hour (20 minutes each) before solvent evacuation.

4.5 Figures

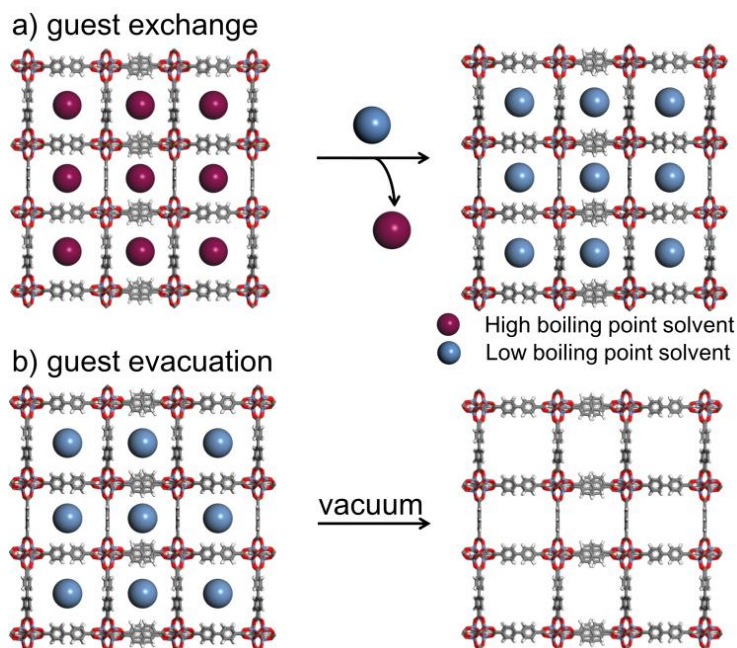


Figure 4.1. a) Guest exchange in MOFs from high boiling point to low boiling point solvent. b) Guest evacuation to remove solvent from MOFs by vacuum.

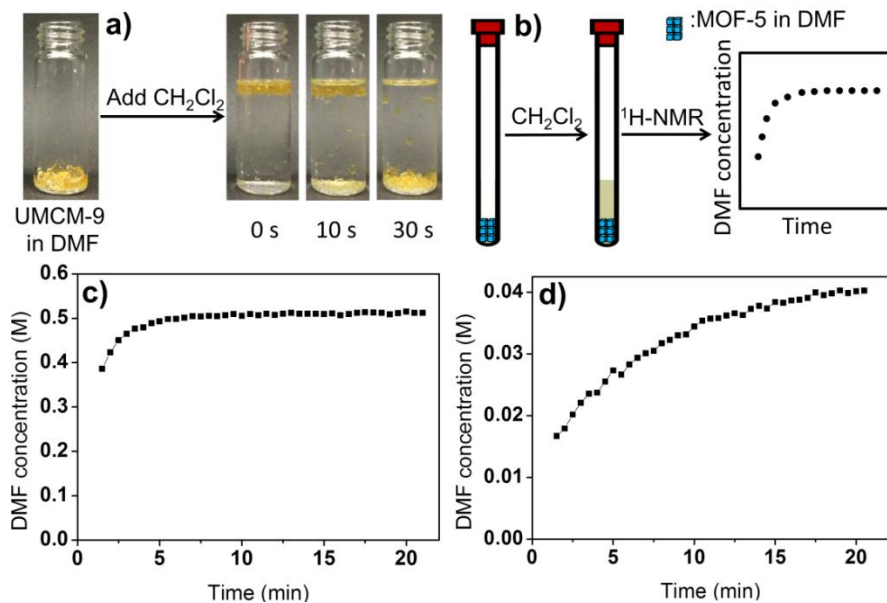


Figure 4.2. a) Images of UMCM-9 in DMF exchanged into CH₂Cl₂. Crystals were found to float (0s) and then sink back to the bottom (10s) completely (30s). b) ¹H-NMR spectroscopy monitoring of the amount of DMF diffusing into CH₂Cl₂ during the c) first and d) second solvent exchange process of MOF-5.

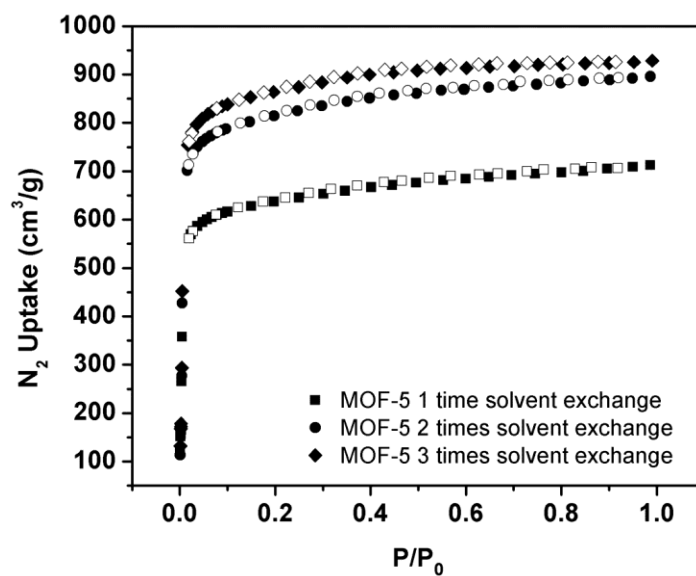


Figure 4.3. N₂ isotherm plot of MOF-5 after 1 (BET SA = 2650 ± 20 m²/g), 2 (BET SA= 3410 ± 30 m²/g) or 3 (BET SA= 3640 ± 40 m²/g) times solvent exchange.

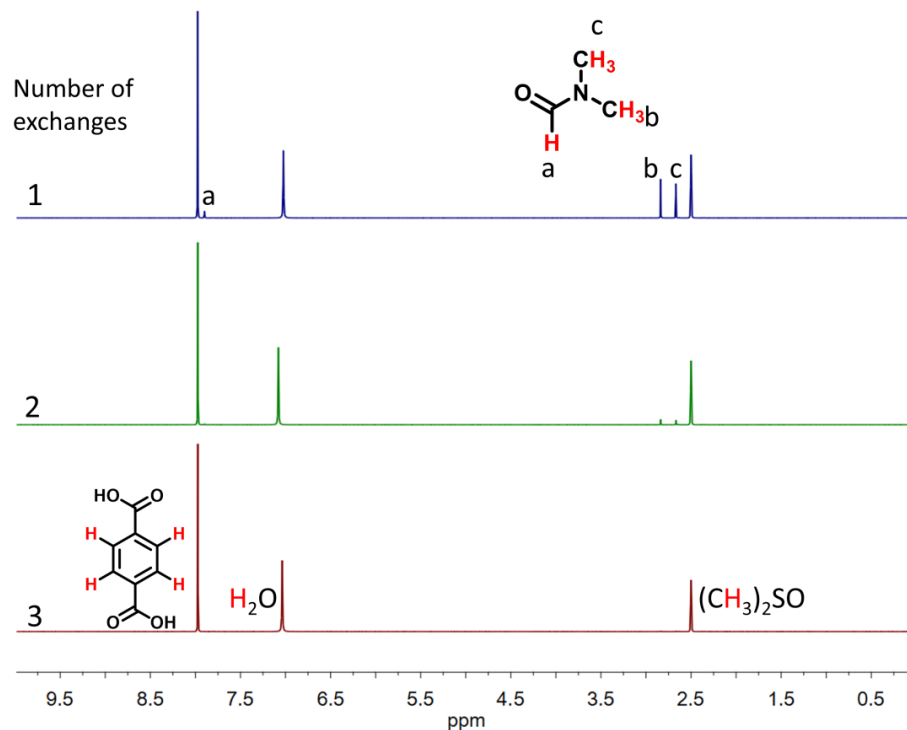


Figure 4.4. DMF content in MOF-5 after multiple solvent exchanges determined by $^1\text{H-NMR}$

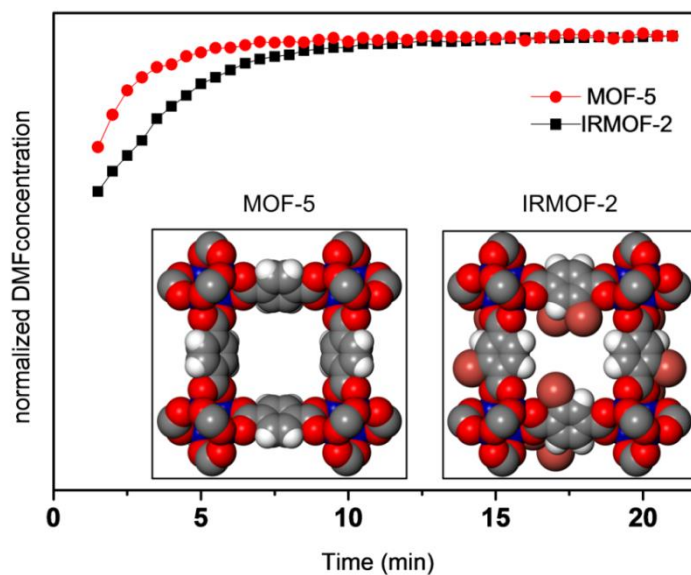


Figure 4.5. $^1\text{H-NMR}$ spectroscopy monitoring of the amount of DMF diffusing into CH_2Cl_2 for MOF-5 and IRMOF-2 during the first solvent exchange process. Concentration of DMF has been normalized for comparison. Inset: structures of MOF-5 and IRMOF-2 (space filling representation, color code: white, H; grey, C; red, O; blue, Zn; maroon, Br)

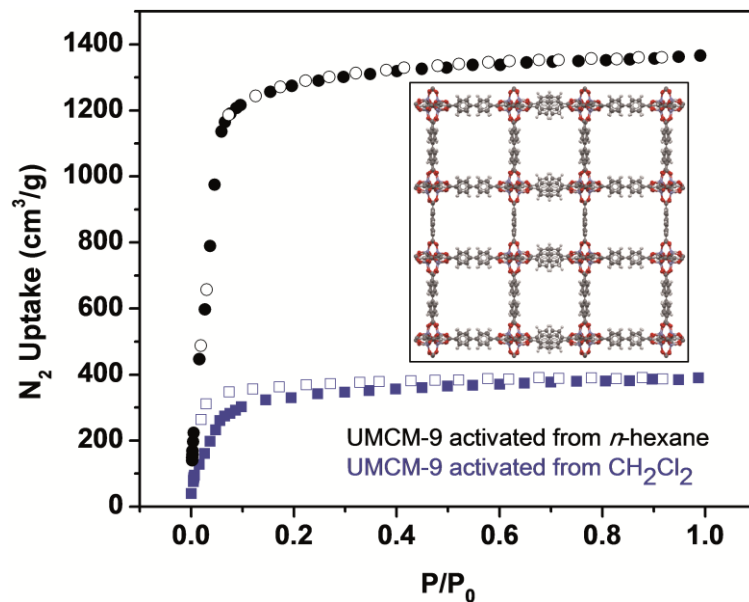


Figure 4.6. N_2 isotherm plots of UMCM-9 activated from *n*-hexane and CH_2Cl_2 exchanged materials. (Adsorption data are shown in full symbols while desorption data are shown in hollow symbols) Inset: Structure of UMCM-9 ($Zn_4O(naphthalene-2,6-dicarboxylate)_{1.5}(biphenyl-4,4'-dicarboxylate)_{1.5}$).

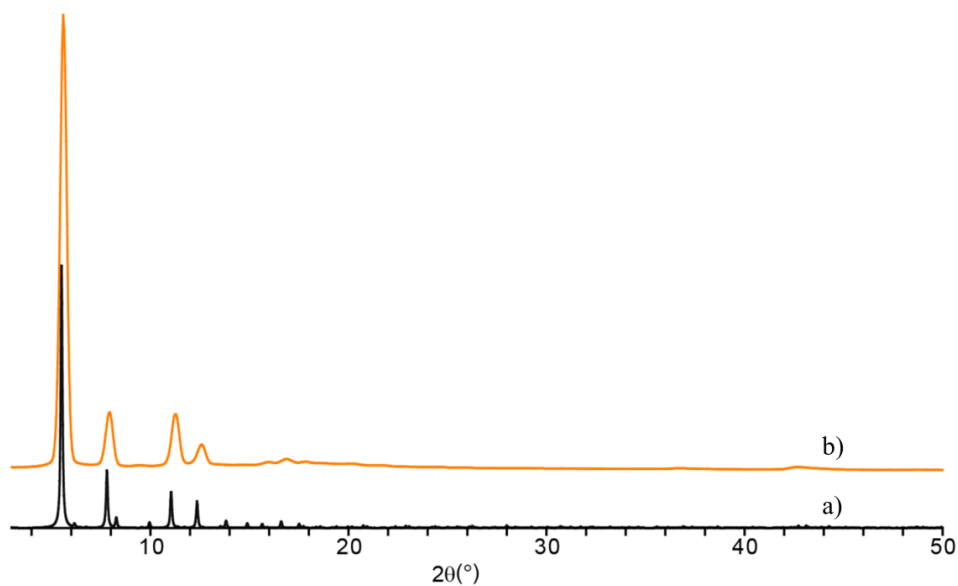


Figure 4.7. PXRD patterns of UMCM-9. a) Simulated, b) conventional solvent exchange activation from *n*-hexane.

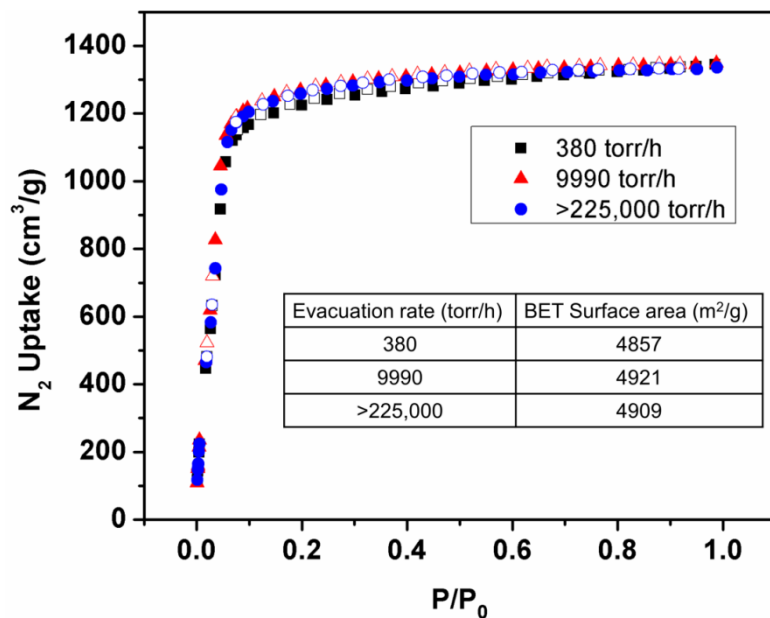


Figure 4.8. N₂ isotherm plot of UMCM-9 activated from n-hexane under different evacuation rates. Inset: BET surface area of activated UMCM-9 with different evacuation rates.

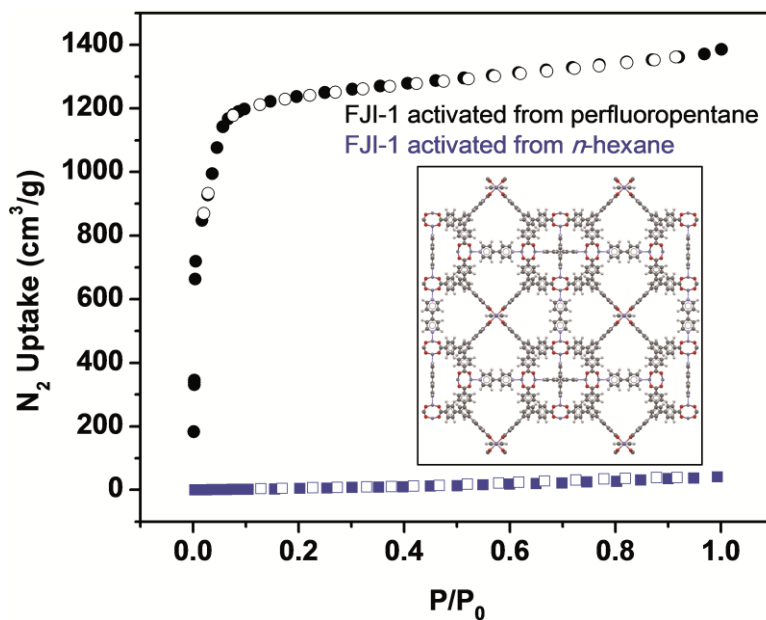


Figure 4.9. N₂ isotherm plots of FJI-1 activated from perfluoropentane and n-hexane exchanged materials. (Adsorption data are shown in full symbols while desorption data are shown in hollow symbols) Inset: Structure of FJI-1 ($Zn_2(\text{benzene-1,3,5-tribenzoate})_{4/3}(4,4'\text{-bipyridine})$).

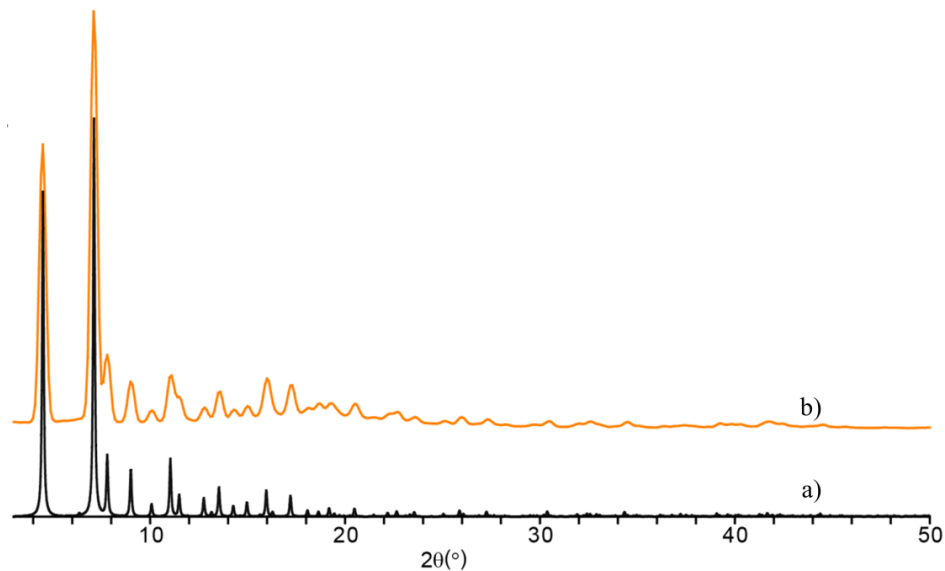


Figure 4.10. PXRD patterns of FJI-1. a) Simulated, b) conventional solvent exchange activation from perfluoropentane.

4.6 Tables

Exchange repeat time	X in $Zn_4O(BDC)_3(DMF)_x$	DMF weight percentage
1	0.78	6.9%
2	0.12	1.1%
3	0.014	0.13%

Table 4.1. DMF content per unit cell after each solvent exchange determined by 1H -NMR spectroscopy.

4.7 References

- (1) Gür, T. M. *Chem. Rev.* **2013**, *113*, 6179.
- (2) Cundy, C. S.; Cox, P. A. *Chem. Rev.* **2003**, *103*, 663.
- (3) Stock, N.; Biswas, S. *Chem. Rev.* **2012**, *112*, 933.
- (4) Farha, O. K.; Hupp, J. T. *Acc. Chem. Res.* **2010**, *43*, 1166.
- (5) He, Y.-P.; Tan, Y.-X.; Zhang, J. *Inorg. Chem.* **2012**, *51*, 11232.
- (6) Nelson, A. P.; Farha, O. K.; Mulfort, K. L.; Hupp, J. T. *J. Am. Chem. Soc.* **2009**, *131*, 458.
- (7) Liu, B.; Wong-Foy, A. G.; Matzger, A. J. *Chem. Commun.* **2013**, *49*, 1419.
- (8) Ma, L.; Jin, A.; Xie, Z.; Lin, W.; *Angew. Chem. Int. Ed.* **2009**, *48*, 9905.
- (9) Li, H.; Eddaoudi, M.; O'Keeffe, M.; Yaghi, O. M. *Nature* **1999**, *402*, 276.
- (10) Feng, D.; Gu, Z.-Y.; Li, J.-R.; Jiang, H.-L.; Wei, Z.; Zhou, H.-C. *Angew. Chem. Int. Ed.* **2012**, *51*, 10307.

- (11) Feldblyum, J. I.; Wong-Foy, A. G.; Matzger, A. J. *Chem. Commun.* **2012**, 48, 9828.
- (12) Kim, J.; Kim, D. O.; Kim, D. W.; Sagong, K. *J. Solid State Chem.* **2013**, 197, 261.
- (13) Liu, J.; Culp, J. T.; Natesakhawat, S.; Bockrath, B. C.; Zande, B.; Sankar, S. G.; Garberoglio, G.; Johnson, J. K.; *J. Phys. Chem. C* **2007**, 111, 9305.
- (14) a) Kaye, S. S.; Dailly, A.; Yaghi, O. M.; Long, J. R. *J. Am. Chem. Soc.* **2007**, 129, 14176.
- (15) Broom, D. P.; Hirscher, M. *Energy Environ. Sci.* **2016**, 9, 3368.
- (16) The term may be accurate for some materials where, for example, additional thermal treatment can reveal the full porosity; however, in cases where collapse occurs the issue is not the completeness of the activation but the integrity of the structure post activation. Nonetheless the term is in common usage.
- (17) a) Howarth, A. J.; Peters, A. W.; Vermeulen, N. A.; Wang, T. C.; Hupp, J. T.; Farha, O. K. *Chem. Mater.* **2017**, 29, 26.
- (18) Sapchenko, S. A.; Samsonenko, D. G.; Dybtsev, D. N.; Fedin, V. P. *Inorg. Chem.* **2013**, 52, 9702.
- (19) Cooper, A. I.; Rosseinsky, M. J. *Nat Chem* **2009**, 1, 26.
- (20) Czaja, A. U.; Trukhan, N.; Muller, U. *Chem. Soc. Rev.* **2009**, 38, 1284.
- (21) Among the major classes of MOFs suitable for exploration, we limit ourselves to the well-established Zn-based structures based on their ubiquity, utility, and relatively long history.
- (22) Koh, K.; Van Oosterhout, J. D.; Roy, S.; Wong-Foy, A. G.; Matzger, A. J. *Chem. Sci.* **2012**, 3, 2429.
- (23) Kim, H. K.; Yun, W. S.; Kim, M.-B.; Kim, J. Y.; Bae, Y.-S.; Lee, J.; Jeong, N. C. *J. Am. Chem. Soc.* **2015**, 137, 10009.
- (24) Eddaoudi, M.; Kim, J.; Rosi, N.; Vodak, D.; Wachter, J.; O'Keeffe, M.; O. M. Yaghi, *Science* **2002**, 295, 469.
- (25) Mondloch, J. E.; Karagiari, O.; Farha, O. K.; Hupp, J. T. *CrystEngComm* **2013**, 15, 9258.
- (26) Hexanes has also been applied in this case achieving similar results.
- (27) Prestipino, C.; Regli, L.; Vitillo, J. G.; Bonino, F.; Damin, A.; Lamberti, C.; Zecchina, A.; Solari, P. L.; Kongshaug, K. O.; Bordiga, S. *Chem. Mater.* **2006**, 18, 1337.
- (28) Haouas, M.; Volkringer, C.; Loiseau, T.; Férey, G.; Taulelle, F. *J. Phys. Chem. C* **2011**, 115, 17934.
- (29) Hench, L. L.; West, J. K. *Chem. Rev.* **1990**, 90, 33.
- (30) The structure is also known as DUT-23(Zn) and SUMOF-1-Zn, see a) Klein, N.; Senkowska, I.; Baburin, I. A.; Gröner, R.; Stoeck, U.; Schlichtenmayer, M.; Streppel, B.; Mueller, U.; Leoni, S.; Hirscher, M.; Kaskel, S. *Chem. Eur. J.* **2011**, 17, 13007. b) Yao, Q.; Sun, J.; Li, K.; Su, J.; Peskov, M. V.; Zou, X. *Dalton Trans.* **2012**, 41, 3953.
- (31) Walton, K. S.; Snurr, R. Q. *J. Am. Chem. Soc.* **2007**, 129, 8552.

Appendix A: A Perylene-based Microporous Coordination Polymer Interacts Selectively with Electron Poor Aromatics[†]

A.1 Introduction

Microporous coordination polymers (MCPs), a class of crystalline solids composed of metal clusters connected by organic linkers, excel in a variety of applications including gas sorption, separations, and catalysis due to their porosity, high surface area, well-defined pore sizes/shapes, as well as tunable chemistries. In particular, using MCPs as separation media for liquid-phase separation has considerable potential for purification of petrochemicals, structural isomers, and stereoisomers, among other classes of adsorbates.¹⁻⁴ Such separations can be strongly influenced by the presence and nature of coordinatively unsaturated metal sites,⁵⁻⁷ sorbent pore size,^{5,8-12} and linker electronic nature. For example, the separation of ethyl benzene and styrene using HKUST-1 as stationary phase is remarkably efficient due to olefin-metal interaction causing selective retention of styrene.^{5,7} An isomeric mixture of *trans*- and *cis*-piperylene is resolved with MIL-96 owing to the cage structure and narrow cage windows which selectively facilitate the efficient packing of the *trans* isomers inside the pore.¹⁰ Yet, examples of MCPs for liquid-phase separation based on electronic interaction between the linkers and guest molecules are rare.¹³ Electronic interaction, particularly the π - π donor-acceptor, is one of the most predictable interactions between aromatics with opposing electronic character and thus could act as an orthogonal recognition element for

[†] Published: Tran, L. D.; Ma, J.; Wong-Foy, A. G.; Matzger, A. J. *Chem, Eur. J.* **2016**, *16*, 5509.

electron poor aromatics (e.g. nitroaromatics). Based on this hypothesis, a new separation material can be designed specifically to allow the selective separation of these compounds. As a secondary consideration, it is important to note that unlike typical silica gel based sorbents used in separations, the vast majority of MCPs employed as separation media contain relatively small pores (less than 12 Å), which limits separations to low molecular weight molecules. In this paper the new MCP UMCM-310 was designed specifically to address these problems and to explore the potential of a ligand with unique electronic character to affect a difficult class of separations.

A.2 Results and Discussion

Perylene, a polycyclic aromatic compound commonly found in dye molecules and used as a donor in donor-acceptor complexes, was chosen to construct UMCM-310.¹⁴ Due to its large conjugated system, perylene frequently serves as a π -donor and thus, can have strong interactions with electron deficient nitroaromatics.¹⁵ With this in mind, the ligand 2,5,8,11-tetrakis(4-carboxyphenyl)perylene H₄L (Figure A.1) was designed and synthesized based on the fact that the appended benzoic acid moieties will significantly increase the size of the linker and thus result in the formation of a MCP with large pores and high surface area. It is important to note that the use of perylene as a building unit for coordination polymers has not yet succeeded, thus emphasizing the challenging of the linker synthesis. Unlike pyrene, 2,5,8,11-tetra substituted perylene cannot be prepared simply by traditional halogenation reactions. Yet these specific C-H bonds can be activated and borylated by a one-step Ir-catalyzed direct C-H borylation reaction to form tetra-borylated perylene (compound **1**, Figure A.1).¹⁶ This tetraborylated compound (**1**) is then subjected to Suzuki coupling with butyl-4-iodobenzoate to generate a tetra-ester intermediate (compound **2**) which is hydrolyzed to form the desired linker H₄L (see experimental methods section).

Solvothermal reaction of H₄L with Cu(NO₃)₂ in the presence of the co-linker 4,4'-bipyridine (bpy) yields the green crystalline UMCM-310. The structure of

UMCM-310 was evaluated by single crystal analysis. The selective interaction of UMCM-310 toward electron poor aromatics was demonstrated through separation experiments with nitroaromatics due to the fact that these are an important class of industrial compounds and have been widely used as explosives, dyes, insecticides, as well as herbicides. Additionally, an example of employing UMCM-310 as stationary phase for the separation of large organic molecules is presented.

Due to the nature of H₄L, a flat conjugated tetracarboxylic acid, its reaction with Cu(II) salts is predicted to form a 2D coordination polymer. As a consequence, a 4,4'-bipyridine (bpy) pillar linker is necessary to organize 2D sheets into a 3D structure. With that in mind, bpy was added as co-linker for the MCP formation reaction. UMCM-310 crystals were formed after approximately 4.5 hours incubation of the solution containing H₄L, bpy, and Cu(NO₃)₂ in NMP/DMF/ethanol/H₂O/CF₃COOH solvent mixture. Conducting the reaction with additional glass surfaces for crystals to grow also induces the formation of small particle size MCPs (10 – 90 μm) which are desirable to increase the column packing efficiency and thus separation performance of the MCPs.¹⁷ The isostructural MCP can be obtained with zinc.

Single-crystal X-ray diffraction of the green cuboctahedron shaped UMCM-310 reveals the framework consists of Cu paddlewheels linked together by perylene-based H₄L linkers and bpy. Each Cu paddlewheel is coordinated to 4 H₄L linkers. The co-linker bpy coordinates to the axial position of two Cu paddlewheels making every Cu paddlewheel a 5-connected node in the framework; such coordination is rarely observed in Cu paddlewheel based MCPs (Figure A.2a). In the ligand, the four carboxylate groups and phenyl rings are twisted; the dihedral angle between the carboxylates and the perylene plane is 38.5°. The structure contains both mesopores and micropores. The mesopores are constructed with 16 paddlewheels and 8 perylene linkers into a cuboctahedron shape (Figure A.2b). The internal diameter is 26 Å and the largest pore window is 16.6 Å (Figure A.2c). A smaller micropore (internal diameter = 13 Å) is

formed with four Cu paddlewheels in a tetrahedral shape (Figure A.2a). Topology analysis of UMCM-310 reveals a new net. Most of the previously reported MCPs, composed of Cu paddlewheels and tetracarboxylate linkers crystallize in the nbo net.¹⁹⁻²⁰ When bpy was used as co-linker, bimetallic paddlewheels and tetracarboxylate linkers coordinate and form 2D sheets. These sheets are connected by bpy and the obtained MCPs are fsc net.²¹ UMCM-310, on the other hand, crystallizes in a 2,4,5-c net which has not been reported before. We designate the net **LYT**.

UMCM-310 was activated by flowing supercritical CO₂ from methanol or acetone soaked crystals.²²⁻²³ The BET surface area was measured from the N₂ sorption isotherm and calculated to be in the range of 4511–5110 m²/g depending on the sample (Figure A.3); this value is relatively high compared with other reported MCPs. Pore size distribution was evaluated through Ar sorption experiment and reveals that UMCM-310 has two types of pores corresponding to the dimensions of 17 and 25 Å (Figure A.3). Due to the presence of the mesopores and large pore windows (Figure A.2c), UMCM-310 can potentially be used for the separation of large molecules. Despite the fact that UMCM-310 can be fully activated to have high surface area, the framework gradually collapses after guest removal as the BET surface area drops to ~2700 m²/g after 9 days. However, the UMCM-310 is stable in acetone or methanol solution suggesting application in liquid phase separations is feasible.

The separation performance of UMCM-310 toward nitroaromatic compounds was initially studied with the nitrobenzene series. A suspension of UMCM-310 (~24 mg) in hexanes/DCM was packed into an HPLC column (50 × 2.1 mm) and hexanes was chosen as the mobile phase. A mixture of nitrobenzene (NB), *o*-dinitrobenzene (*o*-DNB) and 1,3,5-trinitrobenzene (TNB) were fully separated with UMCM-310 as stationary phase (Figure A.4a). Similar baseline separation was obtained with the series of NB, *p*-dinitrobenzene (*p*-DNB) and TNB. The order of retention time is NB (1.2 min) < *o*-DNB (4.5 min) ~ *p*-DNB (5.6 min) < TNB (12 min). Calculation of resolution (R)

between these compounds gave the value of 1.32 – 2.49 (Table A.1). These high R values demonstrate the ability of UMCM-310 to fully resolve the mixture of nitrobenzenes. Overall, UMCM-310 shows strong preference for compounds containing a higher number of nitro groups consistent with a model wherein the more electron-deficient aromatic systems interacts more strongly with the perylene-based framework.

TNT is the most prevalent explosive and is widely used for both military and industrial purposes. In the manufacture of TNT, after several nitration steps, crude TNT is produced contaminated with the meta (unsymmetrical isomers) TNT and dinitrotoluenes (mostly 2,4-dinitrotoluene). Meta TNT can be removed through the conventional sulphitation method.²⁴ However, this method is not capable of eliminating other contaminants. In order to minimize the amount of dinitrotoluenes (DNT), a relatively harsh nitration condition is needed which also facilitates the formation of oxidation products. Recrystallization of crude TNT in alcohol or nitric acid is effective yet this method causes loss of TNT.²⁴⁻²⁵ These obstacles emphasize the need to search for a novel separation method to purify TNT from DNT. Since UMCM-310 has demonstrated its ability to differentiate nitrobenzenes based on the number of nitro groups, it can potentially be used to purify TNT. A mixture of 2,4-dinitrotoluene (2,4-DNT) and TNT was passed through a column packed with UMCM-310 with hexanes as the eluent. A complete baseline separation was obtained (Figure A.5a). As expected, TNT ($t_R = 10.4$ min) is more retained than 2,4-DNT ($t_R = 3.5$ min) due to its higher level of nitration. Moreover, UMCM-310 successfully separates the mixture of 2,4-DNT and 2,6-dinitrotoluene (2,6-DNT) (Figure A.5b). As was shown in the chromatogram, 2,4-DNT elutes first followed by 2,6-DNT ($t_R=9.5$ min). In a higher performance column configuration, TNT would be easily separable from the DNT isomers. Nonetheless the difference in retention times between the isomeric dinitrotoluenes indicates that, in addition to purely electronic nature of the adsorbate, other factors influence the separation such as the substitution pattern of nitration and its influence on charge distribution and

substituent conformation.

As mentioned previously, most of the examples using MCPs as stationary phases explore small molecule separations. For example, for MIL-47 or MIL-53, 1,3,5-triisopropylbenzene is unretained and therefore was used to determine the bed void time.^{6,26} The separation performance of UMCM-310 towards large molecule mixtures was evaluated through analyzing a mixture of 1,3,5-triphenyl benzene and 1,3,5-tris(4-bromophenyl)benzene which have kinetic diameters of 11.8 and 13.6 Å respectively.⁵ 1,3,5-Triphenyl benzene was unretained in the columns packed with HKUST-1 and the 1,3,5-tris(4-bromophenyl)benzene was unretained in MOF-5.⁵ A binary mixture of these compounds was completely separated by UMCM-310 (Figure A.6). 1,3,5-Tris(4-bromophenyl)benzene has the longer retention time most likely because it is somewhat more electron deficient and has stronger van der Waals interaction with the framework. This example demonstrates the ability of UMCM-310 to be used for the separation of mixtures of large organic molecules.

A.3 Conclusions

In conclusion, a new MCP designed to interact selectively with electron deficient aromatic compounds is reported. UMCM-310 composed of 2,5,8,11-tetrakis(4-carboxyphenyl)perylene linker, Cu₂ paddlewheels cluster, and 4,4'-bipyridine was successfully synthesized and characterized to have high surface area (~5000 m²/g) and large pore sizes. UMCM-310 is very efficient for the purification and separation of large molecules and nitroaromatic compounds.

A.4 Experimental Methods

Reagents. All reagents were obtained from commercial vendors and used as-received unless otherwise noted.

Thermogravimetric Analysis. A Q50 TGA (TA instrument, New Castle, Delaware, USA) was used to obtain thermogravimetric data. Samples (2-3 mg) were heated and

analyzed in a platinum pan under a flow of dry nitrogen.

Gas sorption measurements. N₂ and Ar sorption experiments were carried out using an Autosorb 1C (Quantachrome Instruments, Boynton Beach, Florida, USA). He (99.999%, used to determine void volume), N₂ (99.999% purity), Ar (99.999%) were purchased from Cryogenic Gases and used as received. An activated sample (~20 mg) was charged into a sample cell in a N₂-filled glove box and subsequently transferred to the sorption apparatus for measurement at 77K (N₂ isotherm) and 87K (Ar Isotherm).

Powder X-ray diffraction. Powder X-ray diffraction data were collected on a Rigaku R-Axis Spider diffractometer equipped with an image plate detector and CuK α radiation operating in transmission mode at 40kV and 44 mA. Samples were soaked in mineral oil then mounted on nylon loops for data collection. Samples were fixed in χ at 45 °, rotated in ϕ , and oscillated in ω (80-140 °) to minimize preferred orientation.

2,5,8,11-tetrakis(4,4,5,5-tetramethyl-1,3,2-dioxaboranyl)perylene 1: Compound **1** was synthesized followed the reported procedure with a slight modification.²⁷ Perylene (477.2 mg, 1.885 mmol) and bis pinacolato diboron (2.891 g, 11.38 mol) were added to a 250 mL Schlenk flask equipped with a stirrer. The flask was then evacuated and refilled with N₂ 3 times before transferring to a glovebox. Inside the glovebox, [Ir(OMe)(COD)]₂ (137 mg, 0.207 mmol) and 3,4,7,8-tetramethyl-1,10-phenanthroline (63.4 mg, 0.268 mmol) were added. Dry THF (38 mL) was added outside the glovebox via syringe and the resulting mixture was stirred at 80 °C for 24 h under N₂ atmosphere. The flask was wrapped with aluminum foil during the reaction. After completion, the reaction mixture was cooled to RT and solvent was removed under reduced pressure. The resulting solid was purified by column chromatography in DCM:Ethyl acetate (20:1) to give a yellow solid (1.067 g, 75% yield). ¹H-NMR (400 MHz, CDCl₃, ppm) δ 8.62 (s, 4H) 8.24 (s, 4H) 1.43 (s, 48H).

2,5,8,11-Tetrakis(n-butyl-benzoate-4-yl)perylene(2): 2,5,8,11-tetrakis(4,4,5,5-tetramethyl-1,3,2-dioxaboranyl) perylene **1** (535.7 mg, 0.7084 mmol), Pd₂(dba)₃ (67.7 mg,

0.0739 mmol), triphenyl phosphine (77.7 mg, 0.296 mmol), CsF (430.9 mg, 2.837 mmol), Cs₂CO₃ (1.146 g, 3.517 mmol), *n*-butyl 4-iodobenzoate (7.465 g, 24.54 mmol) were dissolved in a solvent mixture of THF (36 mL) and DMF (36 mL) in a 350 mL glass bomb. This mixture was capped with Teflon screw cap and wrapped in aluminum foil. The reaction was heated with stirring at 110 °C for 2-3 days. After completion, the reaction mixture was cooled to RT followed by evaporation of organic solvents. The remaining solid was washed by hexanes (800 mL) and dry-sorbed onto silica gel. Purification by column chromatography in DCM:ethyl acetate (20:1) gave the solid product as an orange solid (386.6 mg, 57% yield). ¹H NMR (400 MHz, CDCl₃, ppm) δ 8.44 (*s*, 4H) 8.20 (*d*, *J* = 8.2 Hz, 8H) 7.97 (*s*, 4H) 7.83 (*d*, *J* = 8.2 Hz, 8H) 4.39 (*t*, *J* = 6.6 Hz, 8H) 1.87–1.76 (*m*, 8H) 1.60–1.47 (*m*, 8H) 1.03 (*t*, *J* = 7.4 Hz, 12H).

2,5,8,11-Tetrakis(4-carboxyphenyl)perylene (H₄L). Intermediate **2** (317.6 mg, 0.3318 mmol), NaOH (241.5 mg, 6.038 mmol), MeOH (32.0 mL), THF (32.0 mL), and H₂O (3.2 mL) were added to a 150 mL bomb flask equipped with a stir bar. The resulting mixture was heated with stirring at 80 °C overnight and monitored by TLC. After completion, the mixture was cooled down to RT, the organic solvents were removed under reduced pressure. The remaining solid was dissolved in H₂O and stirred at RT for an hour followed by filtration. The filtrate was acidified by HCl 1N and the precipitate was collected by centrifuge. Drying under high vacuum overnight gave the product as a red solid (222.9 mg, 92% yield). ¹H NMR (700 MHz, DMSO-D₆, ppm) δ 13.06 (*brs*, 4H) 8.76 (*s*, 4H) 8.22 (*s*, 4H) 8.10 (*d*, *J* = 8.2 Hz, 8H) 8.06 (*d*, *J* = 8.2 Hz, 8H). ¹³C NMR (175 MHz, DMSO-D₆, ppm) δ 167.2, 143.8, 137.8, 134.8, 130.8, 129.93, 129.90, 127.4, 127.1, 127.0, 120.5. Anal. calcd for C₄₈H₂₈O₈•0.786H₂O: C, 77.19; H, 3.99. Found C, 77.56; H, 4.15.

UMCM-310: A mixture of 2,5,8,11-tetrakis(4-carboxyphenyl)perylene (H₄L) (13.3 mg, 0.0182 mmol), Cu(NO₃)₂•2.5H₂O (32.2 mg, 0.141 mmol), and 4,4'-bipyridine (12.1 mg, 0.0773 mmol) were dissolved in the solvent mixture of NMP (15.0 mL) and DMF

(3.0 mL) by sonication (5 mins) followed by the addition of CF₃COOH (4.0 mL, 0.068M solution in ethanol:H₂O (3.5:1)). The resulting mixture was filtered and distributed equally into six 20 mL-scintillation vials. Two microscope slides were placed in each vial to create additional sites for crystal growth. The vials were incubated in the oven at 95 °C for 4.5 hours, after which time green crystals were formed. The reaction mixtures were allowed to cool to room temperature followed by rinsing with fresh DMF (3 times over 1 day) and subsequently with acetone (4 times over 3 days) and stored in acetone. UCMCM-310 was activated by flowing supercritical CO₂ and the obtained materials were stored in a N₂ glove box until analysis. For reaction yield determination, the solvent was removed under high vacuum. The yield of the dry material is 30.4%, based on H₄L. Anal. calcd for Cu₂(C₄₈H₂₄O₈)0.5(C₁₀H₈N₂): C, 68.16; H, 3.02; N, 1.50 Found C, 67.69; H, 3.06; N, 1.58.

UMCM-310(Zn): A mixture of 2,5,8,11-tetrakis(4-carboxyphenyl)perylene (H₄L) (4.46 mg, 0.00609 mmol), Zn(NO₃)₂•6H₂O (11.2 mg, 0.0376 mmol), and 4,4'-bipyridine (4.04 mg, 0.0259 mmol) were dissolved in NMP (12.0 mL) by sonication (~5 mins). H₂O (1.5 pipette drops) were added to the solution and the resulting mixture was filtered and distributed equally into two 20 mL-scintillation vials. The vials were incubated in the oven at 85 °C for 12 days, after which time orange crystals were formed. The reaction mixtures were allowed to cool to room temperature followed by rinsing with fresh DMF (3 times over 1 day) and subsequently with DCM (4 times over 3 days) and stored in DCM. However, due to the difficulty in preparing a phase pure UCMCM-310(Zn), this material was not explored further

Supercritical CO₂ activation. Samples were activated following our previously reported procedure.²² MCPs in acetone or methanol were transferred to a stainless steel HPLC tube. The organic solvent was exchanged with liquid CO₂ (2 mL/min) for 1.5 hour. The column was then heated to 55 °C to convert liquid CO₂ to supercritical CO₂ (2 mL/min). After 2 hours, the flow rate was decreased to 1 mL/min and kept at this flow

rate for another 6.5 hours. Finally, the pressure was reduced to convert supercritical CO₂ to gaseous CO₂ and the backpressure reduced to 1 bar. Activated samples were immediately transferred to a nitrogen-filled glove box and stored until analysis.

A.5 Figures

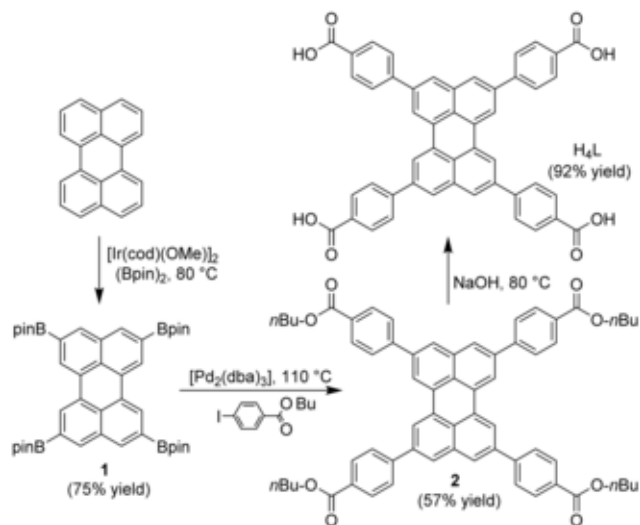


Figure A.1. Synthesis of 2,5,8,11-tetrakis(4-carboxyphenyl)perylene H₄L (cod=1,5-cyclooctadiene; dba=dibenzylideneacetone).

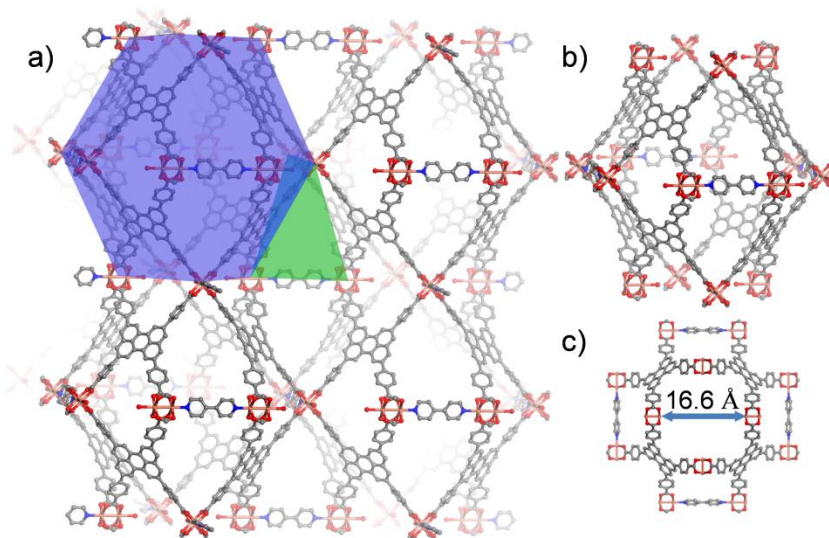


Figure A.2. a) Structure of UMCM-310 with large pore (blue) and small pore (green) indicated. b) Structure of mesoporous cage (large pore). c) Large pore window with Cu-Cu distance measured to be 16.6 Å.

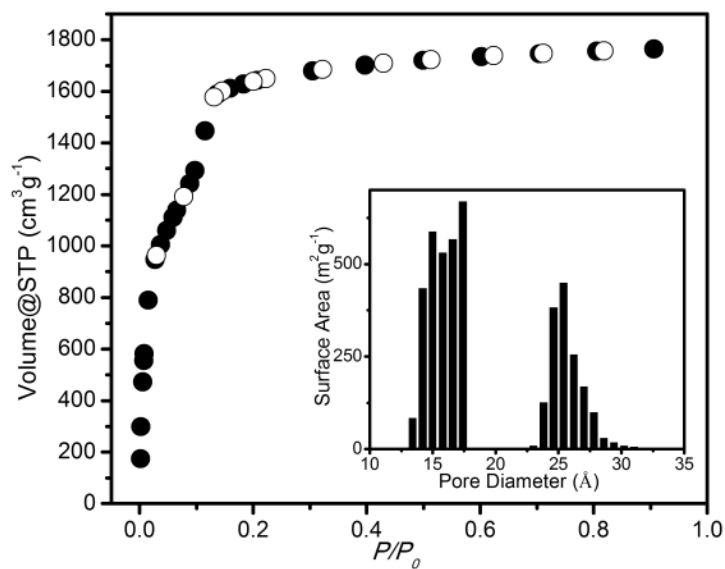


Figure A.3. N_2 -sorption isotherm of UMCM-310 (●adsorption, ○desorption). Insert: Pore-size distribution from NLDFT fitting of the Ar-sorption isotherm.

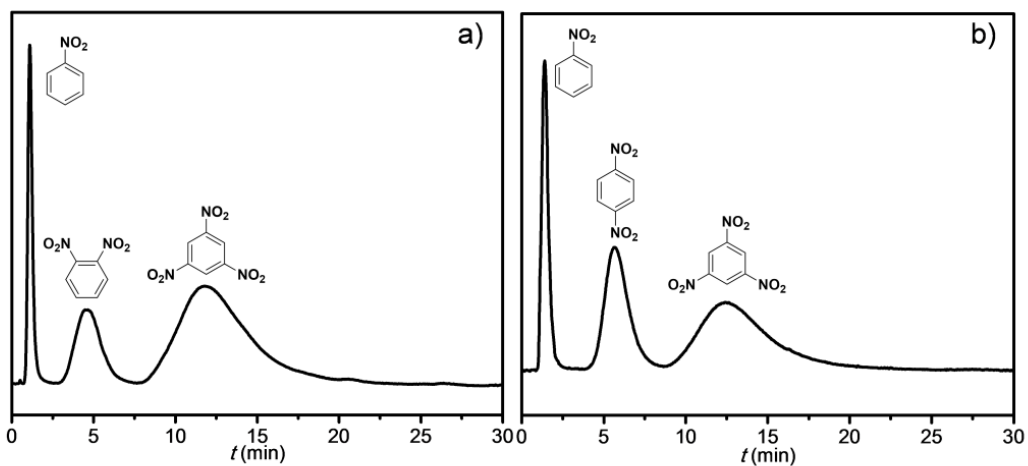


Figure A.4. Liquid-phase separation of nitrobenzenes on a UMCM-310 packed column at a flow rate 1 mL/min: a) mixture of nitrobenzene, o-dinitrobenzene, and 1,3,5-trinitrobenzene ($\lambda=219$ nm); and b) mixture of nitrobenzene, p-dinitrobenzene, and 1,3,5-trinitrobenzene ($\lambda=240$ nm).

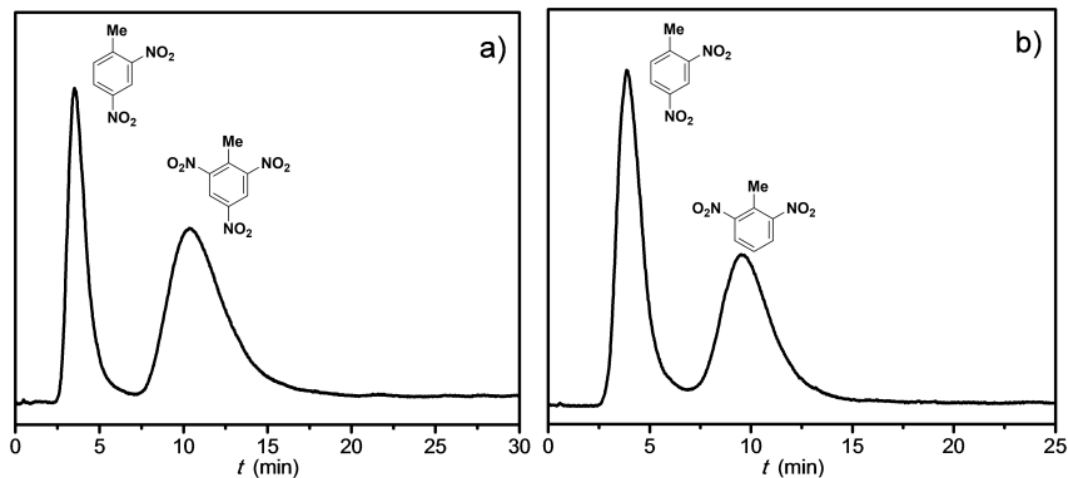


Figure A.5. Liquid-phase separation of nitrotoluenes on a UMCM-310 packed column at a flow rate 1.5 mL/min: a) mixture of 2,4-dinitrotoluene and 2,4,6-trinitrotoluene ($\lambda=224$ nm); and b) mixture of 2,4-dinitrotoluene, 2,6-dinitrotoluene ($\lambda=227$ nm).

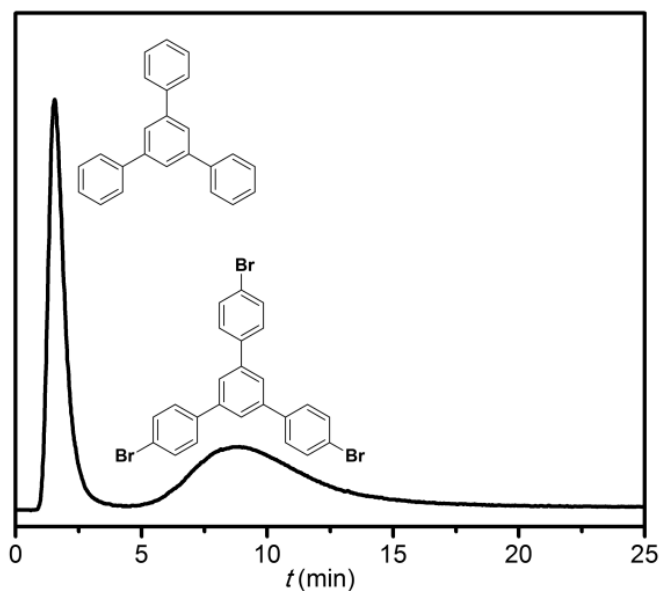


Figure A.6. Liquid-phase separation of a mixture of 1,3,5-triphenyl benzene and 1,3,5-tris(4-bromobenzyl)benzene on a UMCM-310 packed column (flow rate 1.5 mL/min; $\lambda=260$ nm).

A.6 Tables

Peak 1	Peak 2	R
Nitrobenzene (NB)	<i>o</i> -Dinitrobenzene (<i>o</i> -DNB)	1.95
<i>o</i> -DNB	TNB	1.36
NB	<i>p</i> -Dinitrobenzene (<i>p</i> -DNB)	2.49
<i>p</i> -DNB	TNB	1.32
2,4-Dinitrotoluene (2,4-DNT)	Trinitrotoluene (TNT)	1.63
2,4-DNT	2,6-Dinitrotoluene	1.63
1,3,5-Triphenyl benzene	1,3,5-Tris(4-bromophenyl)benzene	1.52

Table A.1. Resolution of compounds separated by liquid chromatography using UCMC-310 as stationary phase

A.7 References

- (1) Cychosz, K. A.; Ahmad, R.; Matzger, A. J. *Chem. Sci.* **2010**, *1*, 293
- (2) Van de Voorde, B.; Bueken, B.; Denayer, J.; De Vos, D. *Chem. Soc. Rev.* **2014**, *43*, 5766;
- (3) Li, J.-R.; Sculley, J.; Zhou, H.-C. *Chem. Rev.* **2012**, *112*, 869;
- (4) Herm, Z. R.; Bloch, E. D.; Long, J. R. *Chem. Mater.* **2014**, *26*, 323.
- (5) Ahmad, R.; Wong-Foy, A. G.; Matzger, A. J. *Langmuir* **2009**, *25*, 11977;
- (6) Alaerts, L.; Maes, M.; van der Veen, M. A.; Jacobs, P. A.; De Vos, D. E. *Phys. Chem. Chem. Phys.* **2009**, *11*, 2903;
- (7) Maes, M.; Vermoortele, F.; Alaerts, L.; Denayer, J. F. M.; De Vos, D. E. *J. Phys. Chem. C* **2011**, *115*, 1051;
- (8) Fu, Y.-Y.; Yang, C.-X.; Yan, X.-P. *Langmuir* **2012**, *28*, 6794.
- (9) Huang, G.; Yang, C.; Xu, Z.; Wu, H.; Li, J.; Zeller, M.; Hunter, A. D.; Chui, S. S.-Y.; Che, C.-M. *Chem. Mater.* **2009**, *21*, 541;
- (10) Jiang, H.-L.; Tatsu, Y.; Lu, Z.-H.; Xu, Q. *J. Am. Chem. Soc.* **2010**, *132*, 5586;
- (11) Maes, M.; Alaerts, L.; Vermoortele, F.; Ameloot, R.; Couck, S.; Finsy, V.; Denayer, J. F. M.; De Vos, D. E. *J. Am. Chem. Soc.* **2010**, *132*, 2284;
- (12) Van der Perre, S.; Duerinck, T.; Valvekens, P.; De Vos, D. E.; Baron, G. V.; Denayer, J. F. M.; *Microporous Mesoporous Mater.* **2014**, *189*, 216;
- (13) Kuang, X.; Ma, Y.; Su, H.; Zhang, J.; Dong, Y.-B.; Tang, B. *Anal. Chem.* **2014**, *86*, 1277.
- (14) Park, T.-H.; Cychosz, K. A.; Wong-Foy, A. G.; Dailly, A.; Matzger, A. J. *Chem. Commun.* **2011**, *47*, 1452.
- (15) Torrance, J. B.; *Mol. Cryst. Liq. Cryst.* **1985**, *126*, 55.
- (16) Landenberger, K. B.; Matzger, A. J.; *Cryst. Growth Des.* **2010**, *10*, 5341.
- (17) Coventry, D. N.; Batsanov, A. S.; Goeta, A. E.; Howard, J. A. K.; Marder, T. B.; Perutz, R. N. *Chem. Commun.* **2005**, 2172.

- (18) Holcroft, J. M.; Hartlieb, K. J.; Moghadam, P. Z.; Bell, J. G.; Barin, G.; Ferris, D. P.; Bloch, E. D.; Algaradah, M. M.; Nassar, M. S.; Botros, Y. Y.; Thomas, K. M.; Long, J. R.; Snurr, R. Q.; Stoddart, J. F. *J. Am. Chem. Soc.* **2015**, *137*, 5706.
- (19) Chen, B.; Ockwig, N. W.; Millward, A. R.; Contreras, D. S.; Yaghi, O. M. *Angew. Chem. Int. Ed.* **2005**, *44*, 4745.
- (20) Ma, S.; Sun, D.; Simmons, J. M.; Collier, C. D.; Yuan, D.; Zhou, H.-C.; *J. Am. Chem. Soc.* **2008**, *130*, 1012.
- (21) Farha, O. K.; Malliakas, C. D.; Kanatzidis, M. G.; Hupp, J. T. *J. Am. Chem. Soc.* **2010**, *132*, 950.
- (22) Liu, B.; Wong-Foy, A. G.; Matzger, A. J. *Chem. Commun.* **2013**, *49*, 1419;
- (23) Nelson, A. P.; Farha, O. K.; Mulfort, K. L.; Hupp, J. T.; *J. Am. Chem. Soc.* **2009**, *131*, 458.
- (24) Kaye, S. M. in *Encyclopedia of Explosives and Related Items, PATR 2700, Vol. 9*, US Army Armament Research and Development Command, **1980**, 235.
- (25) Urbanski, T. in *Chemistry and Technology by Explosives. Vol. I*, Macmillan, **1964**, 345.
- (26) El Osta, R.; Carlin-Sinclair, A.; Guillou, N.; Walton, R. I.; Vermoortele, F.; Maes, M.; de Vos, D.; Millange, F. *Chem. Mater.* **2012**, *24*, 2781.
- (27) Coventry, D. N.; Batsanov, A. S.; Goeta, A. E.; Howard, J. A. K.; Marder, T. B.; Perutz, R. N. *Chem. Commun.* **2005**, *0*, 2172.